universiteit hasselt
KNOWLEDGE IN ACTION

2015 | Faculty of Sciences

DOCTORAL DISSERTATION

Diffusion of interacting particles in confined geometries: a random walk approach

Doctoral dissertation submitted to obtain the degree of
Doctor of Science: Physics, to be defended by

Thijs Becker

Promoter: Prof. Dr Bart Cleuren

D/2015/2451/19

Samenvatting

In deze thesis bestuderen we de diffusie van interagerende deeltjes in sterk begrenzende structuren. Een voorbeeld van materialen met een begrenzende structuur zijn nanoporeuze materialen, zoals zeolieten. Veel zeolieten bestaan uit een aaneenschakeling van holtes. In iedere holte kunnen slechts enkele moleculen zitten. We beschouwen een roostermodel, waarbij iedere holte een punt op het rooster is. De deeltjes voeren een willekeurige wandeling uit op het rooster, beschreven door een Markov dynamica. Er is interactie tussen deeltjes die dezelfde positie bezetten op het rooster. Deze interactie wordt beschreven door een vrije energie $F(n)$ die afhangt van het aantal deeltjes n op die positie. Hiernaast wordt ook nog het maximale aantal deeltjes $n_{\max}$ per roosterplaats ingevoerd. De begrenzende structuur van het materiaal en de interactie van de deeltjes beïnvloeden dan de vorm van $F(n)$ en de waarde van $n_{\max}$.

Diffusie wordt beschreven door verschillende coëfficiënten. In thermodynamisch evenwicht is de zelfdiffusie D_s de relevante grootheid. D_s geeft aan hoe snel de gemiddelde kwadratische verplaatsing van een deeltje groeit in de tijd. Indien er een concentratiegradiënt aanwezig is gebruikt men de transport diffusie D_t. Deze geeft de verhouding tussen de deeltjesflux en de concentratiegradiënt in het systeem. Tot voor kort vond men in experimenten dat de transport diffusie altijd groter is dan de zelfdiffusie. In een experiment in een nanoporeus materiaal vond men recent het omgekeerde gedrag: de zelfdiffusie was groter dan de transport diffusie. Later werd er gesuggereerd dat dit het gevolg is van het clusteren van de deeltjes. Met ons model kan het verband tussen het clusteren van deeltjes enerzijds en $D_s > D_t$ anderzijds op een duidelijke manier begrepen worden. We stellen vast dat het clusteren van de deeltjes een noodzakelijke maar niet voldoende voorwaarde is voor $D_s > D_t$. Verder kan ook de experimenteel geobserveerde concentratie-afhankelijkheid van D_s en D_t begrepen worden met ons model.

We berekenen analytische uitdrukkingen voor D_s en D_t voor willekeurige interactiesterktes en deeltjesconcentraties. Deze uitdrukkingen worden bekomen door gebruik te maken van een gemiddelde-veld benadering. Dit houdt in dat de correlaties tussen opeenvolgende sprongen van de deeltjes genegeerd worden. De uitdrukkingen zijn exact indien de parameterwaarden zo zijn dat ons model een zero-range process is.

De exacte Markov dynamica van het systeem, met inbegrip van correlaties, wordt numeriek gesimuleerd met kinetische Monte Carlo. We vinden dat ons model in staat is om het diffusief gedrag van zowel aantrekkende als afstotende deeltjes in nanoporeuze materialen te beschrijven. De diffusie vertraagt altijd door de correlaties. Voor de experimenteel relevante gevallen kan de verhouding van D_s en D_t goed voorspeld worden via de niet-gecorreleerde uitdrukkingen, ook als D_s en D_t afzonderlijk sterk beïnvloed worden door correlaties.

In veel toepassingen wordt een leeg nanoporeus materiaal in contact gebracht met een deeltjesreservoir. De snelheid waarmee de deeltjes in het materiaal stromen is van cruciaal belang. Het omgekeerde proces, namelijk het leegstromen van het materiaal in contact met een leeg reservoir, is evenzeer van belang. We bestuderen daarom beide processen voor verschillende deeltjesinteracties. We vinden dat de snelheid van absorptie en desorptie sterk afhankelijk is van de startconcentratie en interactie. Deze resultaten worden besproken aan de hand van de tijdsafhankelijke concentratieprofielen.

We bestuderen het gemiddelde en de fluctuaties van de deeltjesstroom in de stationaire niet-evenwichtstoestand, in de macroscopische limiet. We vinden dat de fluctuaties van de stroom voorspeld kunnen worden door het zogenaamde additiviteitsprincipe.

Abstract

In this thesis we study the diffusion of interacting particles in confined geometries. An example of materials with a confining geometry are nanoporous materials, such as zeolites. Many zeolites consist of a series of connected cavities. Each cavity can contain only a few molecules. We consider a lattice model, where each cavity is a site on the lattice. The particles perform a random walk on the lattice, described by a Markovian dynamics. Particles occupying the same lattice site interact. This interaction is described by a free energy $F(n)$ that depends on the number of particles n on that site. Also the maximal number of allowed particles at a lattice site $n_{\max}$ is introduced. The confinement of the material and the particle interactions then influence the shape of $F(n)$ and the value of $n_{\max}$.

Diffusion is described by different coefficients. In thermodynamic equilibrium the self-diffusion D_s is the relevant quantity. D_s quantifies how fast the mean squared displacement of a single particle increases in time. If a concentration gradient is present, one uses the transport diffusion D_t. This quantity gives the ratio of the particle flux and concentration gradient in the system. Until recently, one found in experiments that the transport diffusion is always larger than the self-diffusion. In an experiment in a nanoporous material one recently found the reverse behavior: the self-diffusion was larger than the transport diffusion. Later, it was suggested that this was the result of particle clustering. With our model, the connection between particle clustering on the one hand and $D_s > D_t$ on the other hand can be clearly understood. We find that particle clustering is a necessary but not sufficient condition for $D_s > D_t$. Furthermore, our model allows for an understanding of the experimentally observed concentration dependence of D_s and D_t.

We calculate analytical expressions for D_s and D_t which are valid for all interactions and concentrations. These expressions are found by using a mean field approximation. This means that correlations between subsequent particle jumps are neglected. These expressions are exact if the parameters are such that our model becomes a zero-range process.

The exact Markov dynamics, including correlations, is simulated numerically using kinetic Monte Carlo. We find that our model can correctly describe the diffusive behavior of both attractive and repulsive particles in nanoporous materials. The diffusion always slows down because of correlations. For the experimentally relevant cases the ratio of D_s and D_t can be accurately predicted from the uncorrelated expressions, even if D_s and D_t separately are strongly influenced by correlations.

In many applications an empty nanoporous material is brought into contact with a particle reservoir. The rate at which particles are absorbed in the material is of crucial importance. The reverse process, i.e., the desorption of particles from a material in contact with an empty reservoir, is of equal importance. We study, therefore, both processes for different particle interactions. We find that the rates of absorption and desorption strongly depend on the starting concentration and interaction. These results are understood from a discussion of the time-dependent concentration profiles.

We study the average and fluctuations of the particle current in the nonequilibrium steady state, in the macroscopic limit. We find that the fluctuations can be predicted by the so-called additivity principle.

Contents

Chapter 1

Introduction

1.1 Diffusion: A short history

We start the introduction with a short historical account of the experiments and theories that led to the understanding of Brownian motion and Fickian diffusion. Both phenomena are the result of the perpetual erratic motion of matter on the atomic scale. Historically, however, their experimental investigation has occurred separately. It took almost 80 years before Albert Einstein made the connection between the two, in one of his four *annus mirabilis* papers of 1905 [1].

The part about Brownian motion is mostly based on the work of Stephen Brush [2]. Refs. [3] and [4] were also consulted. The discussion on Fickian diffusion is based on articles by Mehrer and Stolwijk [5] and Philibert [6]. A dutch translation of Einstein's original paper [1] can be found in [7].

1.1.1 Early experiments: Brown, Graham, and Fick

Robert Brown

Robert Brown (1773-1858) was a Scottish botanist who performed pioneering work in the use of the microscope. He was one of the first to give a detailed description of the cell nucleus. Brown's research on diffusion originated from an attempt to find the mode of action of pollen in the process of impregnation. Small particles that are contained in the pollen, with lengths of around 0.005 mm, were immersed in water and observed under a microscope (see [8] for a recent account of the same experiment). Brown published his results in 1828; he describes his observations as follows [9]:

> While examining the form of these particles immersed in water, I observed many of them very evidently in motion; their motion consisting not only of a change of place in the fluid, manifested by alterations in their relative positions, but also not infrequently by a change of form of the particle itself ... In a few instances the particle was seen to turn on its longer axis. These motions were such as to satisfy me, after frequently repeated observation, that they arose neither from currents in the fluid, nor from its gradual evaporation, but belonged to the particle itself.

This erratic and perpetual movement of small particles suspended in a liquid is nowadays referred to as Brownian motion. It had, in fact, been observed several times before Brown. In his second publication on the subject, Brown himself mentioned ten different previous accounts of the motion he observed. Nevertheless, there are very good reasons to name the phenomenon after Brown. He was the first to study the motion precisely and extensively. By performing measurements for several different substances, ranging from organic matter to pieces of glass to a fragment of the Sphinx of Giza, he showed that dead and living matter exhibited equally well the motion. This proved that the motion was not self-animated, a common view among biologists at the time, who thought their observations were particular to organic particles. Brown's observations moved the subject from biology to physics.

Also physicists and chemists observed the motion. The first (known) written account is from Jan Ingen-Housz (1784). After introducing finely ground charcoal in a drop of alcohol he describes what he sees as follows: "... one will see these corpuscles in a confused continuous and violent motion as if they were animalcules which move violently forward". Ingen-Housz did however not investigate the matter further. He ascribed the motion to evaporation. Brown showed in his experiments that this explanation is incorrect. Other prior observers gave either no or erroneous explanations, did not perform further investigations, and were unsuccessful in popularizing their findings.

Thomas Graham

The Scottish chemist Thomas Graham (1805-1869) was probably the first to study the diffusion in gases systematically. This was done over the years 1828 to 1833 (note that Graham started in the year of Brown's first publication). He found that the rate at which gases diffuse is inversely proportional to the square root of their molar masses:

$$\frac{v_A}{v_B} = \sqrt{\frac{M_B}{M_A}}, \tag{1.1}$$

with M_A and M_B the molar masses and v_A and v_B the average velocities of the A and B molecules. This relation is called Graham's law. Its importance lies in the fact that it could be understood from the molecular-kinetic theory of gases developed by Maxwell and Clausius. More specifically, it could be attributed to the equipartition of the kinetic energies of the molecules

$$M_A v_A^2/2 = M_B v_B^2/2 = 3kT/2, \tag{1.2}$$

with k the Boltzmann constant and T the temperature. This provided a connection between the random motion of molecules in gases on the one hand and diffusion on the other hand. Graham also studied the diffusion of salts in liquids, noticing that it was at least several thousand times slower than in gases.

Adolf Fick

Adolf Fick (1829-1901) was a German physiologist. He made important contributions to medicine, where he applied the concepts of physics to the study of living organisms. He was both a gifted experimentalist and theorist. Fick studied the diffusion of salt

in water, which was published in 1855. He had read the work Graham, but regretted that no fundamental law of diffusion was developed. In analogy to Fourier's law of thermal conduction and Ohm's law of electrical conduction, Fick postulated that the particle flux j is proportional to the gradient of the concentration c:

$$j = -D\frac{\partial c}{\partial x}. \tag{1.3}$$

This is nowadays known as Fick's first law. D is called the diffusion coefficient. Using conservation of matter he also found the equation

$$\frac{\partial c}{\partial t} = D\frac{\partial^2 c}{\partial x^2}, \tag{1.4}$$

now called the diffusion equation or Fick's second law.

Fick measured the concentration profiles of salt in water in a vertical cylinder and a funnel. The stationary concentration profile was created by putting one end of the system in contact with a reservoir at high salt concentration and the other end with pure water. One finds from the diffusion equation that the concentration profile is linear in the cylinder, and inversely proportional to the length for the funnel. This was indeed what Fick observed experimentally. He also determined the diffusion coefficient of salt by measuring the flux in the stationary state.

Fick's theoretical work was later extended to multicomponent diffusion by James Clerk Maxwell (1866) and Josef Stefan (1871).

1.1.2 Theoretical understanding of Brownian motion: Einstein and Smoluchowski

Although Brownian motion was widely known after Brown's original publications, none of the great kinetic theorists such as Boltzmann, Clausius, and Maxwell, investigated it. Other scientists did try to give an explanation of the observed effect. Some suggested that the presence of a temperature gradient due to evaporation caused the motion, apparently unaware that Brown had already dismissed this possibility. The idea that repulsive particle interactions are the driving force was revisited several times. Also here Brown had already performed convincing experiments that excluded this possibility. Others conjectured it was an electrical phenomenon, or the consequence of local hydrodynamic currents or temperature gradients, and so on.

Careful experiments were conducted by Christian Wiener (1863) and Léon Gouy (1889). Both concluded that the motion was not due to external influences, but must come from internal motions in the fluid. Wiener thought that matter consists of material atoms and aether atoms. An important role in his explanation was reserved for the aether atoms. His attempt to understand the physical mechanism underlying Brownian motion was therefore unsuccessful. Gouy dismissed the possibility that the uncoordinated collisions of molecules are responsible for the motion, and suggested that molecular movements in liquids are partly coordinated at small spatial scales.

To summarize, by the end of the 19th century Brownian motion was widely known, and many scientists assumed it had something to do with thermal motions in the fluid itself. Unfortunately, there was still no quantitative theory that made experimental predictions, or a clear picture of the physical mechanism.

Albert Einstein

The first quantitative theory of Brownian motion was published by Albert Einstein in 1905 [1]. He considered particles of small size suspended in a fluid at equilibrium. His aim was to contrast the predictions of thermodynamics and molecular-kinetic theory on the motion of the particles.

Thermodynamics predicts that a solution of particles enclosed by a semipermeable membrane exerts an osmotic pressure. The pressure is predicted by van 't Hoff's law; in today's notation it is seen to be the ideal gas law $pV = NkT$, with V the volume, N the number of particles in the volume, and p the osmotic pressure. Small particles (i.e., much bigger than the molecules in the solvent) suspended in a liquid do not exert a pressure according to thermodynamics. Einstein argued that this is an artificial distinction, and showed that kinetic-molecular theory predicts that small suspended particles also obey van 't Hoff's law. He combined this result with Stokes law for the velocity (v) of a spherical particle experiencing a force (F) in a fluid: $v = F/\zeta$. Here, $\zeta = 6\pi\eta R_p$ is the friction coefficient, with η the viscosity of the fluid and R_p the radius of the particle.

Now consider a constant force that is exerted on the particles. This creates a concentration gradient of particles. In the steady state, this force is counteracted by the osmotic pressure. By balancing the diffusive flux due to the concentration gradient, Eq. (1.3), and the flux resulting from the constant force, one finds

$$D = kT/\zeta. \tag{1.5}$$

This is known today as the Stokes-Einstein or Sutherland-Einstein relation.

Einstein then goes on to derive the diffusion equation (1.4). Since it is assumed that the particles do not influence each other, this equation can be applied to the position of a single particle. If at time $t = 0$ the particle is at position $x = 0$, the probability distribution of its position x at time t is, in one dimension, given by

$$f(x,t) = \frac{1}{\sqrt{4\pi D}} \frac{e^{-x^2/4Dt}}{\sqrt{t}}. \tag{1.6}$$

From this probability distribution one can derive that the average deviation around the starting position is given by

$$\overline{x^2} = 2Dt. \tag{1.7}$$

This equation tells us that a particle suspended in a fluid at equilibrium fluctuates around its average position, i.e., molecular-kinetic theory predicts Brownian motion. The average position squared scales linearly with the observation time.

Einstein's contribution can be summarized as follows. Firstly, he showed that Brownian motion follows from the application of molecular-kinetic theory to fluids. Secondly, the relevant experimental quantity is the mean-squared displacement (MSD) of the particles. The MSD grows linearly in time and is proportional to the diffusion coefficient introduced by Fick. This provides a quantitative connection between Brownian motion and Fickian diffusion. We will later see that using Fick's diffusion coefficient in Eq. (1.7) is correct only if the particles are noninteracting, as was explicitly assumed by Einstein. Finally, the result allowed for an experimental determination of the size of the particles or Avogadro's number.

Marian Smoluchowski

Marian Smoluchowski published his paper on Brownian motion in 1906, shortly after Einstein. His approach was based on the kinetic theory of gases, which was less abstract than Einstein's statistical mechanics approach.

After a discussion of the experimental results on the subject, Smoluchowski proceeds by clearing up a common misconception. The argument was that an individual collision of a fluid particle with the suspended particle is much too weak to have a visible effect on the movement of the particle. Furthermore, if the particle is bombarded from all sides the effect of the different collisions is expected to average out. Why this argument is erroneous can be understood from a simple calculation. Consider a particle in one dimension, surrounded to its left and right by fluid particles. The fluid particles collide from the left and right with equal probability. A collision from the left (right) imparts a velocity $v = +1$ (-1) on the particle. If there are n collisions in total, the probability to have m collisions from the left is

$$p_{n,m} = \frac{1}{2^n}\binom{n}{m}. \tag{1.8}$$

The average positive or negative deviation from zero velocity (i.e., $m = n/2$), equals

$$v = 2\sum_{m=n/2}^{n}(2m-n)p_{n,m} = \frac{n}{2^n}\binom{n}{n/2}. \tag{1.9}$$

For large n one finds

$$v \simeq \sqrt{2n/\pi}. \tag{1.10}$$

In words: the velocity of the suspended particle *increases* with the square root of the number of collisions. The large number of collisions is therefore an argument *in favor* of the interpretation that Brownian motion is caused by atomic collisions.

This model is, however, too simple. It does, for example, not take into account that if the particle has a certain velocity, collisions are less likely to increase its velocity in that direction. Smoluchowski therefore proceeds with the consideration of a more detailed model. The equipartition theorem predicts that the average velocity v of the particle is equal to

$$v = v_f\sqrt{m/M}, \tag{1.11}$$

with v_f and m, respectively, the average velocity and mass of the fluid particles, and M the mass of the suspended particle. Due to collisions the particle changes its direction around 10^{16} times per second. It therefore follows a zigzag path, constantly changing its direction, making it impossible to observe its average velocity. One can only observe the displacement over many steps of this path. Assume therefore a particle that moves around with the average velocity of Eq. (1.11), but with a constantly changing direction. If one furthermore assumes that molecular collisions happen at equal time intervals, one finds the mathematically tractable problem of calculating the average MSD of a chain made up of segments of equal lengths. After performing the calculation and making several estimates on, e.g., the number of collisions per second, Smoluchowski arrives at the same result as Einstein Eq. (1.7). His diffusion coefficient is about 0.65 times smaller than Einstein's. This is because Smoluchowski makes several assumptions from kinetic theory, while Einstein assumes Stokes law to be valid.

1.1.3 Experimental verification: Perrin

There had been quite a few experimental studies on Brownian motion before Einstein's result. Unguided by theory, these efforts were aimed at the determination of the velocity of the suspended particles, as determined from the equipartition theorem. As explained by Smoluchowski and Einstein, the path of a particle is much too erratic to perform such a measurement. Indeed, the velocity is the derivative of the position x with respect to the time t. Such a quantity is only sensible if the function $x(t)$ is sufficiently smooth.

The conclusive experimental verification was performed in the lab of Jean Perrin. Perrin had a strong interest in the atomic hypothesis and a good knowledge of theoretical developments. Before he started his experiments he already gave talks where he referred to Brownian motion as an example of the violation of the second law on small scales. He was aware of the mathematical studies of functions that are continuous but non-differentiable, and mentioned Brownian motion as a physical example. Perrin took on the task of verifying Einstein's predictions after a presentation of Langevin to the Académie des Sciences in Paris in 1908. He later wrote: "ever since I became, through M. Langevin, acquainted with the theory, it has been my aim to apply to it the test of experiment". Svedberg and Henri had already found that the MSD scales linearly with time. Their diffusion constants were, respectively, six and four times larger than Einstein's prediction.

For a quantitative agreement it is of crucial importance that the suspended particles follow Stokes law. Perrin therefore first checked its validity for small particles of gamboge. He found that Stokes law is valid for particles as small as 0.0001 mm, at least for short enough times. Using spherical grains of gamboge whose radius R_p was precisely measured, Perrin and his students found exact agreement with Eq. (1.7) by taking Avogadro's number $N_A = 64 \times 10^{22}$. The distribution of particles was shown to follow Eq. (1.6). These results were published in 1908 and 1909. Perrin spend a significant amount of time popularizing his results. He argued that his work was a decisive demonstration of the atomic hypothesis. He was most successful: almost all skeptics finally admitted to the reality of atoms. For his work, Perrin was awarded the nobel prize in physics in 1926.

Experimental progress since the days of Perrin has been quite spectacular. The measurement of the instantaneous velocity of a brownian particle has been recently performed [10]. The measurement of the transition between ballistic and diffusive motion of a particle suspended in a liquid has been reported in [11].

1.2 Diffusion in confinement

Until now we considered *freely* suspended particles in a liquid. Often the motion of the particles is restricted by obstacles or a confining geometry. This is common in biological systems. Most of the molecules that make up the cell membrane are able to diffuse on the plane of the membrane [12]. On the membrane there are also immobile structures, called fences. Diffusion can be seen as "free" diffusion on the membrane, temporarily slowed down when a fence is encountered, over which the particle must "hop". This can lead to a MSD that scales as $\overline{x^2} \propto Dt^\alpha$ with $\alpha < 1$, in contrast to Eq. (1.7). A scaling with $\alpha \neq 1$ is called anomalous diffusion. The diffusion of

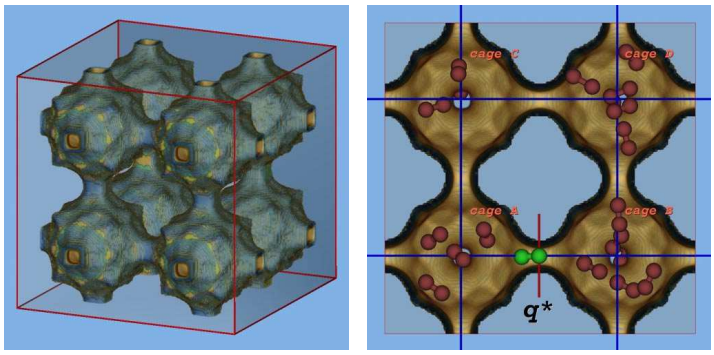

(a) (b)

Figure 1.1: (*a*) A schematic representation of the zeolite Linde type A. (*b*) Molecules diffusing in the material. (Reprinted figure with permission from [E. Beerdsen, B. Smit, and D. Dubbeldam, Phys. Rev. Lett., **93**, 248301, 2004.] Copyright (2004) by the American Physical Society.)

polymers such as DNA through narrow channels is an active field of research [13]. The confinement introduced by the channel wall significantly influences the diffusive behavior. The modeling of particle diffusion in confining geometries is the topic of this thesis. This topic has received considerable attention from theorists in recent years [14]. The main application of the model considered in this thesis is the description of diffusion in nanoporous materials.

1.2.1 Nanoporous materials

An everyday example of a porous material is a sponge: it has a structure that consists of many interconnected voids or pores. These pores are of a macroscopic size and contain a fluid or a gas different from the material. Sponges are therefore ideally suited for water absorption. Materials that are porous on the molecular scale are called nanoporous, although often a distinction is made between macro-, meso-, and microporous, depending on the size of the pores. A well known example of naturally occurring nanoporous materials are zeolites; see Figure 1.1 for an example. Porous structures possess interesting properties. Consider for example the problem of separating a mixture of two different substances. If these two substances are spaghetti and water, life is relatively easy: spaghetti is much larger than a water molecule, and appropriate sieves can be found in the supermarket. However, often one is interested in separating a mixture of molecules of comparable sizes. A nanoporous material can now play the role of the sieve: if its pores allow the passage of one molecule but not the other, one simply needs to introduce a stream of the mixture on one end of the material, and collect the output on the other end. In practice such molecular sieving is more subtle than this simple mechanism, cf. Chapter 20 in [15], but the qualitative idea stays the same.

Nanoporous materials have many more applications. They are currently used, e.g., for catalysis in the petroleum industry [16] and as ion exchangers in water softeners.

Possible future applications include storage of carbon dioxide [17] and hydrogen [18], and use as insulators with a low dielectric constant [19].

Nanoporous materials can be found in nature: over 40 naturally occurring zeolite structures have currently been identified [20]. They can also be synthesized in the laboratory [21]. An important new class of materials is metal-organic frameworks (MOFs) [22]. These are created by combining organic and inorganic molecules, leading to the connection of inorganic subunits by organic linkers. During the last decade hundreds of different MOFs have been synthesized. Since the range of inorganic units, organic linkers, and their interconnection is essentially unlimited, the number of possible structures is practically infinite [23]. This opens up the possibility to synthesize the structure of the material as a function of its application.

1.2.2 Experimental techniques

For almost all applications it is important to understand how atoms and molecules diffuse in such structures. Reliable measurement techniques are therefore of crucial importance. There are macroscopic techniques, where a step change of the pressure is introduced in the environment and the uptake or release of particles is measured. On the other hand there are microscopic methods such as pulsed-field-gradient nuclear magnetic resonance (PFG NMR), which record the diffusion paths of molecules over micrometers [15]. Finding agreement between the different methods [24], and correctly interpreting the experimental data [25], has not always been an easy task.

If the particles do not influence each other, the diffusion coefficients of Fick [Eq. (1.3)] and Einstein [Eq. (1.7)] are equal. Once particle interactions come into play they can differ significantly. In this case the Fick diffusion coefficient is commonly referred to as the transport diffusion D_t:

$$j = -D_t \frac{\partial c}{\partial x}. \tag{1.12}$$

The coefficient of Eq. (1.7) is defined in equilibrium and is referred to as the self-diffusion D_s:

$$\overline{x^2} \propto D_s t. \tag{1.13}$$

Recently, interference microscopy (IFM) and infrared microscopy (IRM) have made it possible to record transient guest profiles in nanoporous materials [26, 27]. With these techniques one can measure the self- and transport diffusion with the same device, under the same operating conditions. A measurement of the self- and transport diffusion of methanol, ethanol, and ethane in a zeolitic imidazolate framework (ZIF), MOF ZIF-8, was performed by Chmelik *et al.* [28]. MOF ZIF-8 is a highly stable and defect free nanoporous material [29], and thus ideal for such an experiment.

The experimental results are shown in Figure 1.2. Both D_s and D_t depend strongly on the concentration. Note that the transport diffusion can become significantly smaller than the self-diffusion for methanol and ethanol. This was the first experimental observation of such behavior. Figure 1.2d shows the adsorption isotherms, i.e., the fractional loading θ (concentration divided by maximal concentration) as a function of the pressure of the environment. $\theta(p)$ displays an "S-shaped" behavior for methanol and ethanol. For ethane the concentration increases much more slowly as a function of the pressure. The strong concentration dependence of the diffusion

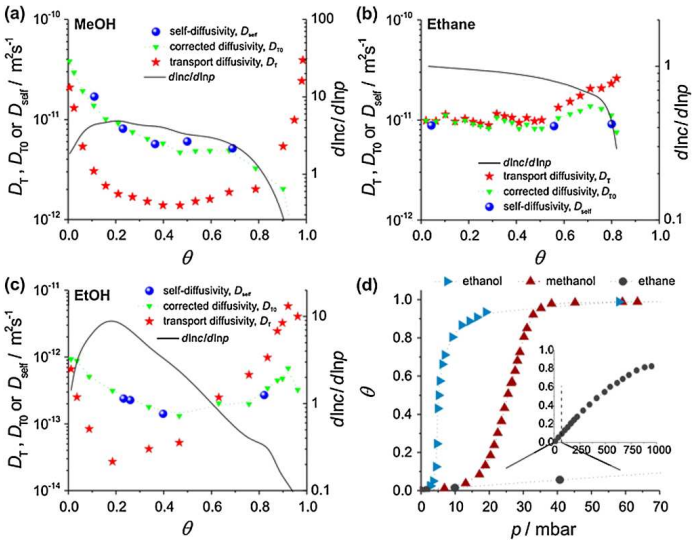

Figure 1.2: Self-diffusion (blue circles) and transport diffusion (red stars) of (a) methanol, (b) ethane, and (c) ethanol, in MOF ZIF-8. The fractional loading as a function of the pressure is given in (d). (Reprinted figure with permission from [C .Chmelik, H. Bux, J. Caro, L. Heinke, F. Hibbe, T. Titze, and J. Kärger, Phys. Rev. Lett., **104**, 085902, 2010.] Copyright (2010) by the American Physical Society.)

coefficients is the result of the interplay between the interparticle interactions and the confinement of the material, as was intuitively argued by Chmelik *et al.* [28]. Later, Krishna and van Baten presented an extensive set of results from molecular dynamics (MD) simulations to show that the molecular mechanism responsible for the self-diffusion exceeding the transport diffusion was the clustering of the particles in the material [30–32].

1.3 Motivation for this work

We can summarize that already today nanoporous materials have a strong technological relevance. The possibility to create new materials in a large variety of structures is likely to increase this relevance in the future. New experimental techniques allow the monitoring of time-dependent guest concentrations, and have created a wealth of new data on particle diffusion coefficients. Nanoporous materials present us with a case of confined diffusion, i.e., particles interact strongly with the material. At nonzero loadings there are also strong interparticle interactions. The interplay between the confinement and interparticle interactions leads to diffusion coefficients that depend on the concentration in a nontrivial way, cf. Figure 1.2. One therefore wants to understand the observed diffusive behavior from the underlying dynamics at the molecular level.

Continuum descriptions of particles diffusing in a confining geometry of varying cross section often rely on a perturbation expansion of some sort [33, 34]. If one

furthermore considers interacting particles and/or high densities, also here a perturbative approach [35–37] or a dynamical density functional theory [38] is necessary. We circumvent these difficulties by putting the particles on a lattice. This type of modeling follows naturally from the structure of many nanoporous materials.

Particle clustering implies that the particles are inhomogeneously distributed at the molecular scale. This has a characteristic effect on the equilibrium properties, such as the adsorption isotherm; cf. Figure 1.2d. A good model should correctly capture the influence of different types of interactions on both the equilibrium properties and the self- and transport diffusion. The description of the interactions should be as general and conceptually simple as possible. A study of the effect of correlations upon the diffusion is also of interest. Also here one would like to have a conceptually simple model that exhibits a variety of behaviors. The construction of such a model is the goal of this thesis.

1.4 Outline of the thesis

This thesis is structured as follows.

In Chapter 2 we introduce the model and discuss the relevant diffusion theory. The methods to numerically determine the self- and transport diffusion are explained. We discuss other lattice approaches to the same problem.

In Chapter 3 we investigate the equilibrium properties, namely the adsorption isotherm and fluctuations in particle number, for different interactions. Recently, there has been interest in systems containing particles that exhibit significant clustering, i.e., the particles are inhomogeneously distributed at the nanoscale. This has a characteristic impact on the equilibrium properties, which we discuss.

In Chapter 4 we calculate analytical results for the diffusion coefficients. These are found by ignoring correlations in the system, which corresponds to the consideration of systems of length 1. The uncorrelated solution is exact for systems of arbitrary length under special conditions, i.e., if our model reduces to a so-called zero-range process. An analytical analysis of the effect of correlations is provided by studying systems of length 2.

In Chapter 5 we present results on the diffusion obtained by numerical simulations. The connection between the self-diffusion exceeding the transport diffusion on the one hand and particle clustering on the other hand, can be understood in simple terms from our model. We find that a qualitative understanding of the behavior of the self- and transport diffusion can be obtained both for repulsive and attractive (clustering) particles, over the whole concentration range. Surprisingly, also a quantitative agreement can be obtained for clustering particles. We analyze the effect of correlations upon the diffusion in detail. The status of our assumptions with respect to experimental systems is discussed at the end.

Chapter 6 contains a discussion of the adsorption and desorption kinetics of the system. We find that for clustering particles the desorption can proceed faster than the adsorption, contrary to what is commonly observed.

In Chapter 7 we study the probability distribution of the current through the system in the nonequilibrium steady state, in different dimensions. The first three cumulants obtained from direct simulations are compared with predictions from the additivity principle [39]. In one and two dimensions the first three cumulants agree

with the predictions from the additivity principle. In three dimensions agreement is found for the first two cumulants. There is insufficient statistics for a reliable estimate of the third cumulant.

Finally, we present our conclusions and some perspectives on interesting further work in Chapter 8.

Chapter 2

The Model

We introduce the model that is studied in this thesis in Section 2.1. Possible forms of the transition rates are calculated using transition-state theory (TST) in Section 2.2. A short introduction to the required diffusion theory is presented in Section 2.3. In Section 2.4 we explain the simulation methods that were used to obtain the diffusion coefficients. Finally, we discuss other work that is related to our model in Section 2.5.

2.1 Construction of the model

The materials we consider consist of a large array of cavities, which are connected to each other by narrow passages, also called windows; see Fig. 2.1. In such a setup, it is natural to assume that the time spent by a particle in a cavity before moving to one of its neighbors is much larger than the equilibration time of particles inside a cavity. This allows us to coarse grain the intracavity degrees of freedom [40]. Interactions are described by the equilibrium free energy $F(n)$, depending only on the number of particles n in the cavity. Contributions to $F(n)$ are the result of particle-particle and particle-wall interactions inside a cavity. When the system is in equilibrium with a particle reservoir at chemical potential μ and temperature T, the probability to have n particles in any cavity is equal to

$$p_n^{\mathrm{eq}}(\mu) = [\mathcal{Z}(\mu)]^{-1}\, e^{-\beta[F(n)-\mu n]}, \tag{2.1}$$

with $\beta = (kT)^{-1}$, k the Boltzmann constant, and $\mathcal{Z}$ the grand-canonical partition function:

$$\mathcal{Z}(\mu) = \sum_{n=0}^{n_{\max}} e^{-\beta[F(n)-\mu n]}. \tag{2.2}$$

Averages over the equilibrium distribution Eq. (2.1) are denoted by $\langle\cdot\rangle$, e.g.,

$$\langle n\rangle(\mu) = \sum_{n=0}^{n_{\max}} n p_n^{\mathrm{eq}}(\mu). \tag{2.3}$$

Since the equilibrium distribution is known for any given $F(n)$ and μ, all equilibrium quantities can be calculated analytically in function of these two variables. For later

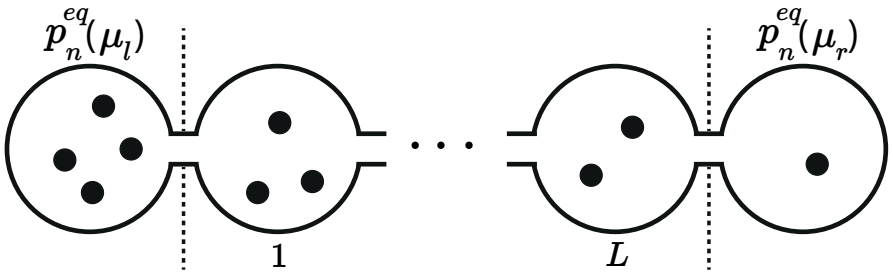

Figure 2.1: The system, shown here between dashed lines, consists of an array of cavities connected by narrow passages. On the boundaries it is connected to uncorrelated cavities with the equilibrium distribution.

reference, we introduce the grand potential $\Omega(n,\mu) = F(n) - \mu n$, which captures the n dependence of the probability. Confinement limits the amount of particles in a cavity and is represented in our model by $n_{\max}$, which is the maximal number of particles a cavity can contain.

A schematic representation of the model in one dimension is given in Fig. 2.1. It consists of pairwise connected cavities numbered from 1 to L. Because we integrate out the intracavity degrees of freedom we can identify the cavities with sites on a lattice. The center-to-center distance between two cavities is equal to λ. A particle jumps from a cavity containing n particles to a cavity containing m particles with probability per unit time k_{nm}. These rates satisfy local detailed balance:

$$\frac{k_{nm}}{k_{m+1,n-1}} = \frac{p_{n-1}^{\mathrm{eq}}(\mu)p_{m+1}^{\mathrm{eq}}(\mu)}{p_n^{\mathrm{eq}}(\mu)p_m^{\mathrm{eq}}(\mu)} \tag{2.4}$$

$$= e^{-\beta[F(n-1)+F(m+1)-F(n)-F(m)]}. \tag{2.5}$$

This ensures that, when the system is in equilibrium, there are no net currents and that the probability distribution equals the equilibrium distribution Eq. (2.1). Particles can enter or leave the system through the boundaries, which are connected to (particle) reservoirs. The left and right reservoirs have, respectively, chemical potential μ_l and μ_r. A reservoir is modeled as a cavity characterized by the equilibrium distribution $p_n^{\mathrm{eq}}(\mu)$ (μ is either μ_l or μ_r), whose state is uncorrelated from the cavity it is connected to (see Appendix C). The rates at which a reservoir cavity at chemical potential μ adds ($k_n^{r,+}$) or removes ($k_n^{r,-}$) one particle from a cavity containing n particles are

$$k_n^{r,+} = \sum_{m=1}^{n_{\max}} k_{mn} p_m^{\mathrm{eq}}(\mu); \quad k_n^{r,-} = \sum_{m=0}^{n_{\max}-1} k_{nm} p_m^{\mathrm{eq}}(\mu). \tag{2.6}$$

With the transition rates determined, one can construct the master equation describing the time evolution of the probability $p_{n_1,n_2,\ldots,n_L}(t)$ for the system to be in state $(n_1, n_2, \ldots, n_L)$ at time t, with n_i the number of particles in the ith cavity. We do not repeat the theory of Markov processes here, see e.g. [41] for an introduction.

Since the focus is here on the influence of the various interactions as compared to

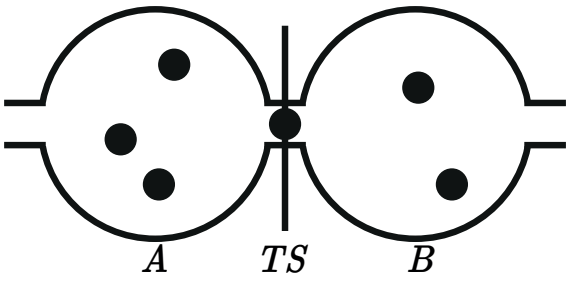

Figure 2.2: Two cavities, A and B, divided by a transition-state surface TS. A particle is in the transition state.

the ideal case, we write the free energy as

$$F(n) = F^{\mathrm{id}}(n) + f(n), \tag{2.7}$$

where $F^{\mathrm{id}}(n)$ is the free energy of an ideal gas:

$$F^{\mathrm{id}}(n) \equiv kT\left[\ln(n!) - n\ln\left(V/\Lambda^3\right)\right], \tag{2.8}$$

with V the volume of a cavity, $\Lambda = h/\sqrt{2\pi MkT}$ the thermal de Broglie wavelength, h the Planck constant, and M the mass of one particle. Note that a linear term in $F(n)$ simply rescales the chemical potential of the system Eq. (2.1). Such a linear term does therefore not influence the equilibrium statistics at a given particle concentration. We call $f(n)$ the interaction free energy, which includes all interactions and confinement. The free energy can be derived from the partition function, defined by

$$Z(n) = \frac{V^n}{n!\Lambda^{3n}} z(n), \tag{2.9}$$

$$z(n) = \frac{1}{V^n}\int_V d\mathbf{r}_1 \ldots \int_V d\mathbf{r}_n e^{-\beta U(\mathbf{r}_1,\ldots,\mathbf{r}_n)}, \tag{2.10}$$

with $\mathbf{r}_i$ the position of the ith particle and $U(\mathbf{r}_1,\ldots,\mathbf{r}_n)$ the interaction energy. The interaction free energy is then determined by the configurational integral $z(n)$ through $f(n) = -kT\ln z(n)$.

2.2 Transition rates

The free energy $F(n)$ does not fully specify the dynamics, contained in the rates k_{nm}, because only local detailed balance Eq. (2.4) has to be obeyed. For example, all rates of the form

$$k_{nm} = \nu n \frac{e^{-\beta c[f(n-1)-f(n)]}}{e^{-\beta(1-c)[f(m)-f(m+1)]}}, \tag{2.11}$$

obey local detailed balance for any $c \in \mathbb{R}$ (ν denotes a positive constant throughout this thesis). As discussed in Appendix A, the physically relevant rates are found for $0 \leq c \leq 1$, where c measures the importance of the interaction of the two cavities

participating in the jump. We use transition-state theory [42] to calculate possible forms of the jump rates. The details of the calculations can be found in Appendix A.

Consider two connected cavities, called A and B, containing respectively n and m particles. In the middle of the window we define a transition-state (TS) surface. If the center of a particle is located on the TS surface, it is said to be in the transition state. The setup is illustrated in Fig. 2.2. The jump rate k_{nm} is equal to the probability that a particle from cavity A is in the transition state, multiplied by its average velocity towards cavity B.

Consider, first, particles which have no long-range interactions. An example is when the particles only feel hard-core repulsion. As a result, the particle in the TS has no influence on the interaction of the particles in cavities A and B. The rates then have the form:

$$k_{nm} = k_{10} e^{-\beta[f(1)-f(0)]} n e^{\beta[f(n)-f(n-1)]}. \tag{2.12}$$

As always we require that $k_{n,n_{\max}} = 0$ for all n. This jump rate only depends on the change in free energy of cavity A. Note that it corresponds to $c = 1$ for the rate given in Eq. (2.11).

Consider now particles with long range interactions. The particle in the TS interacts with the particles of both cavities A and B. k_{nm} therefore depends on the change in interaction free energy of both cavities A and B. We study rates of the form (see Appendix A):

$$k_{nm} = k_{10} n e^{-(\beta/2)[f(n-1)+f(m+1)-f(n)-f(m)]}. \tag{2.13}$$

Note that the change in free energy of cavities A and B is of equal importance. This rate corresponds to $c = 1/2$ in Eq. (2.11).

2.3 Diffusion theory

We present the necessary diffusion theory that will be used in this thesis. We assume that the diffusion is isotropic. Anisotropic diffusion is not considered in this thesis. The average particle concentration at position $\mathbf{r}$ is denoted by $c = c(\mathbf{r})$.

The self-diffusion coefficient D_s describes the average mean-squared displacement (MSD) of a single particle in a system at equilibrium, in the long-time limit:

$$D_s = \lim_{t\to\infty} \frac{1}{2dt} \overline{[\mathbf{r}(t) - \mathbf{r}(0)]^2} = \lim_{t\to\infty} \frac{1}{2dt} \overline{\Delta \mathbf{r}^2(t)}, \tag{2.14}$$

where d is the dimension of the system, $\mathbf{r}$ the position of the particle, and the overline denotes the average over all equilibrium trajectories. A common way of measuring this coefficient is by labeling a subset of the particles in the system (denoted by $*$); see Fig. 2.3. Particles in the reservoir cavities are labeled with different percentages, resulting in a concentration gradient ∇c^* of labeled particles under overall equilibrium conditions. The resulting flux $\mathbf{j}^*$ of the labeled particles reads [15]:

$$\mathbf{j}^* = -D_s \nabla c^*. \tag{2.15}$$

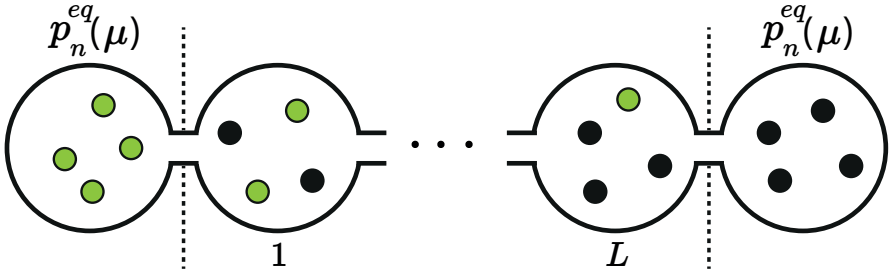

Figure 2.3: Measuring the self-diffusion: A concentration gradient of labeled particles (open green circles) is introduced under overall equilibrium conditions.

The transport diffusion coefficient D_t, also called Fick or chemical diffusion, quantifies the particle flux $\mathbf{j}$ appearing in response to a concentration gradient:

$$\mathbf{j} = -D_t \nabla c. \tag{2.16}$$

It is assumed that the concentration gradient is sufficiently small so linear response is valid. Note the similarity between the definitions of the self-diffusion Eq. (2.15) and the transport diffusion Eq. (2.16). The difference lies in the physical situation to which they apply: out of equilibrium for D_t (Figure 2.1) and in equilibrium for D_s (Figure 2.3).

One can rewrite Eq. (2.16) in terms of the gradient of the chemical potential. The two gradients are related by $\nabla c = (\partial c/\partial \mu)\nabla \mu$. Since $c = \langle n \rangle / V$ with V the volume of one cavity, and $d\langle n \rangle / d\mu = \beta(\langle n^2 \rangle - \langle n \rangle^2)$, as follows from Eq. (2.3), this yields:

$$\mathbf{j} = -D_t \beta \frac{\langle n \rangle}{V} \frac{\langle n^2 \rangle - \langle n \rangle^2}{\langle n \rangle} \nabla \mu. \tag{2.17}$$

The Maxwell-Stefan (MS) diffusion coefficient D_{ms} is defined as [43]

$$\mathbf{j} = -D_{\mathrm{ms}} \beta c \nabla \mu. \tag{2.18}$$

From Eqs. (2.17) and (2.18) it follows that

$$D_t = \Gamma D_{\mathrm{ms}}, \tag{2.19}$$

where we have defined the thermodynamic factor:

$$\Gamma(\mu) = \frac{\langle n \rangle}{\langle n^2 \rangle - \langle n \rangle^2}. \tag{2.20}$$

From Eq. (2.19) one can see that the transport diffusion is the product of a thermodynamic term Γ and a kinetic term D_{ms}. Because thermodynamic effects are "factored out", or corrected for, in D_{ms}, it is sometimes called the corrected diffusion. The Maxwell-Stefan diffusion coefficient can be written as

$$D_{\mathrm{ms}} = \lim_{t \to \infty} \frac{1}{2dNt} \overline{\left(\sum_{i=1}^{N} \Delta \mathbf{r}_i(t) \right)^2}, \tag{2.21}$$

where the sum runs over all N particles in the system. The equivalence of Eq. (2.18) and Eq. (2.21) follows from the Kubo-Green expression for D_{ms} [44]

$$D_{\mathrm{ms}} = \frac{1}{Nd}\int_0^\infty \mathrm{d}t \overline{\left(\sum_{i=1}^{N}\mathbf{v}_i(t)\right).\left(\sum_{i=1}^{N}\mathbf{v}_i(0)\right)}, \tag{2.22}$$

with $\mathbf{v}_i(t)$ the velocity of the ith particle at time t. Because we study particles on a lattice it is better to rewrite Eq. (2.22) as a function of the particle positions $\mathbf{r}_i(t)$. This leads to Eq. (2.21).

The definition Eq. (2.21) is similar to the one for the self-diffusion Eq. (2.14), with the MSD of N times the center of mass of all particles instead of the MSD of one particle. D_{ms} is therefore also called the center-of-mass diffusion coefficient. From Eqs. (2.19) and (2.21) one finds the following relation between the self- and transport diffusion:

$$D_t = \lim_{t\to\infty}\frac{\Gamma}{2dNt}\left(\sum_i \overline{\Delta\mathbf{r}_i^2} + \sum_{i,j\neq i}\overline{\Delta\mathbf{r}_i.\Delta\mathbf{r}_j}\right) \tag{2.23}$$

$$= \Gamma D_s + \lim_{t\to\infty}\frac{\Gamma}{2dNt}\sum_{i,j\neq i}\overline{\Delta\mathbf{r}_i(t).\Delta\mathbf{r}_j(t)}. \tag{2.24}$$

For conciseness we do not write the time dependence in Eq. (2.23).

Two types of correlation effects influence the diffusion. The first type considers only a *single* particle. If the direction and average rate of subsequent jumps of a single particle are uncorrelated, the self-diffusion is equal to $D_s = \lambda^2 k_{\mathrm{av}}/2d$, with k_{av} the average jump rate. In general, however, subsequent jumps are correlated. Consider, for example, the case where only one particle can occupy each lattice site. If a particle jumps, it is more likely to return to the site from where it came, because this site is more likely to be empty. These single-particle correlations influence the self-diffusion D_s. The second type considers the correlation between jumps of *different* particles. It is described by the second term on the right-hand side of Eq. (2.24). If the particles have a tendency to drag along other particles, then this term is positive. This happens, for example, when there is interparticle friction. The Maxwell-Stefan theory of diffusion is often used to study diffusion in porous materials [43]. In this context one can derive the relation:

$$\frac{1}{D_s} = \frac{1}{D_{\mathrm{ms}}} + \frac{1}{D_{\mathrm{cor}}}. \tag{2.25}$$

Interparticle correlations are captured by the term $1/D_{\mathrm{cor}}$, while single-particle correlations influence D_s. $1/D_{\mathrm{cor}}$ is interpreted as resulting from interparticle friction (in continuum models) or correlations between jumps of different particles (in lattice models [45]). It is positive if the interparticle correlation term in Eq. (2.24) is positive and vice versa.

2.4 Numerical simulations: methods

We discuss how the diffusion coefficients are obtained from numerical simulations. The Markov dynamics of the system is simulated using the kinetic Monte Carlo method, as

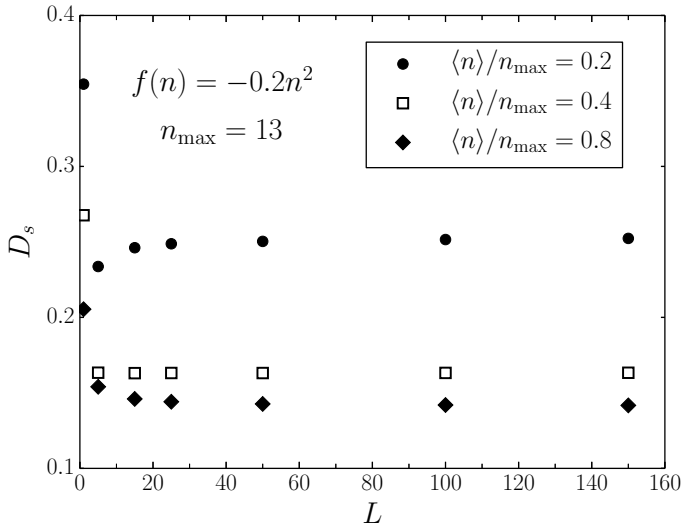

(a)

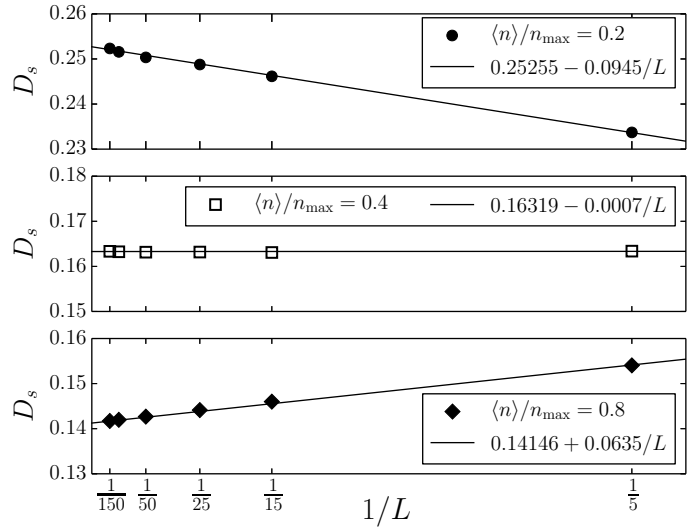

(b)

Figure 2.4: Self-diffusion in a one-dimensional system with $f(n) = -0.2n^2$, $n_{\max} = 13$, the rates of Eq. (2.13), and loadings $\langle n \rangle / n_{\max} = 0.2, 0.4$, and 0.8. (*a*) D_s as a function of the length L of the system. (*b*) The same data, plotted as a function of $1/L$. The analytical fit is obtained using Mathematica, and was done for all lengths except $L = 1$.

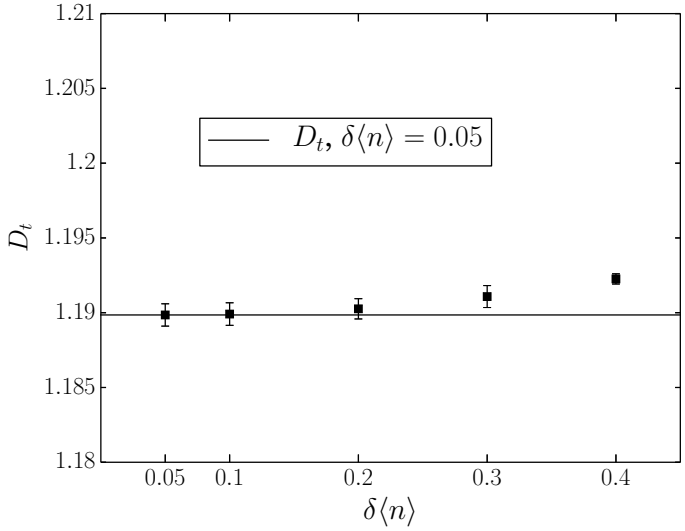

Figure 2.5: Transport diffusion in one dimension as a function of $\delta\langle n\rangle$, for $L = 20$, $n_{\max} = 2$, $\langle n\rangle = 1$, $f(n) = 0$, and the rates of Eq. (2.13).

discussed in Appendix B. The chemical potential corresponding to a certain loading $\langle n\rangle$ can be found numerically via Eq. (2.3). This chemical potential determines the rates at which particles are injected or removed at the boundaries; see Eq. (2.6). Note that we only consider isothermal systems.

2.4.1 Self-diffusion

To measure the self-diffusion at loading $\langle n\rangle(\mu)$ both reservoirs are put at the chemical potential μ. A concentration gradient of labeled particles is introduced by labeling particles that enter from the left or right reservoir with different percentages. D_s can then be found using Eq. (2.15). In the simulations, all particles coming from the left reservoir are labeled (100%), and none of the particles coming from the right reservoir are labeled (0%). Taking different percentages gives the same D_s. We are interested in the situation where the boundary cavities have negligible influence. The length dependence of D_s in a one-dimensional system, for the parameters $f(n) = -0.2n^2$, $n_{\max} = 13$, the rates of Eq. (2.13), at loadings $\langle n\rangle/n_{\max} = 0.2, 0.4$, and 0.8, is shown in Fig. 2.4a. Once $L > 1$ the diffusion is influenced by correlations, as discussed in Chapters 4 and 5, and one observes a sharp decrease of D_s. The influence of the boundary cavities decreases with increasing length. For large L the length dependence scales as $\propto 1/L$. This $1/L$ dependence can be increasing, decreasing, or (approximately) constant, depending on the loading of the system, cf. Fig. 2.4b.

2.4.2 Transport diffusion

The transport diffusion at loading $\langle n\rangle$ is measured by putting the left and right reservoirs at different chemical potentials corresponding to, respectively, $\langle n\rangle + \delta\langle n\rangle/2$

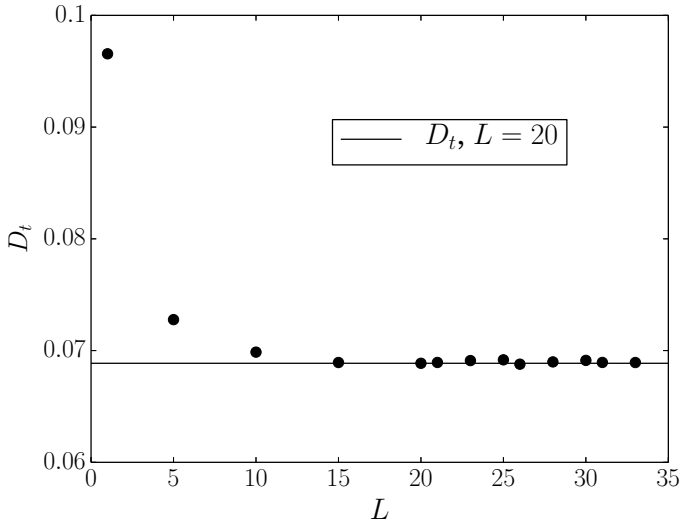

(a)

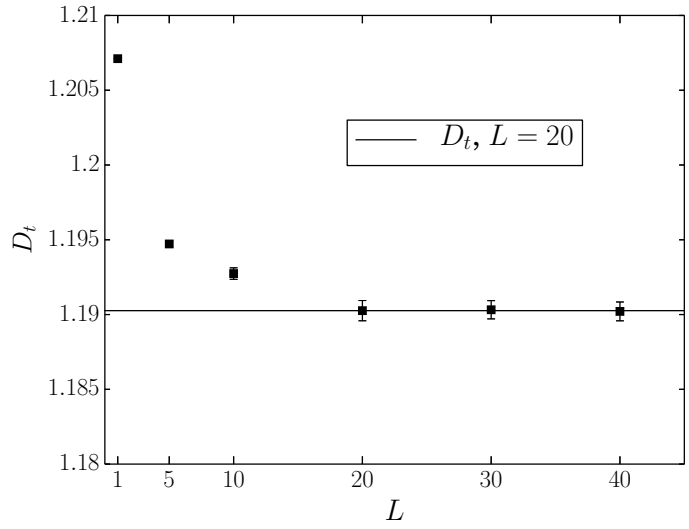

(b)

Figure 2.6: Transport diffusion in a one-dimensional system with the rates of Eq. (2.13). (*a*) $f(n) = -0.2n^2$, $n_{\max} = 13$, and $\langle n \rangle / n_{\max} = 0.8$. (*b*) $f(n) = 0$, $n_{\max} = 2$, and $\langle n \rangle = 1$.

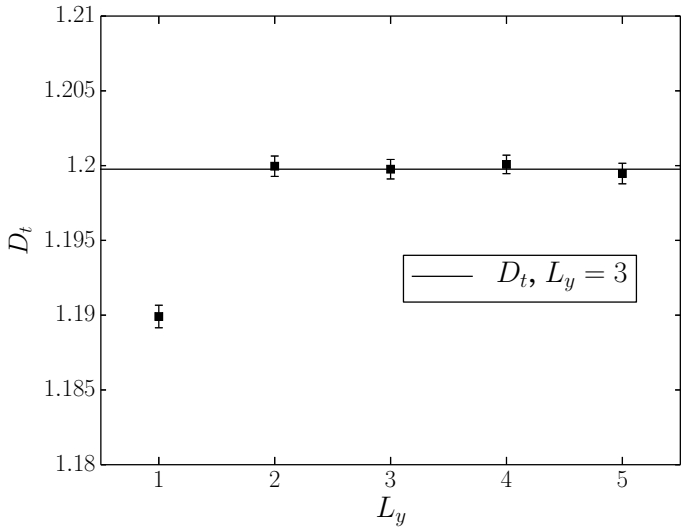

Figure 2.7: Transport diffusion in two dimensions as a function of L_y, for $L_x = 20$, $n_{\max} = 2$, $\langle n \rangle = 1$, $f(n) = 0$, and the rates of Eq. (2.13). Periodic boundary conditions are imposed in the y direction.

and $\langle n \rangle - \delta\langle n \rangle/2$, where $\delta\langle n \rangle$ should be small enough to ensure that one is in the regime of linear response. An example of the convergence to linear response is shown in Figure 2.5. By measuring the particle flux through the system one can calculate D_t using Eq. (2.16). We note that the Maxwell-Stefan diffusion can be found from Eq. (2.19), where the thermodynamic factor Eq. (2.20) is known analytically. The length dependence of the transport diffusion for two different parameter sets is plotted in Fig. 2.6. Also here one observes a sharp decrease of D_t for small L. A convergence to the $L \to \infty$ limit is found around $L = 20$. The time needed to achieve good statistics is much larger for the transport diffusion than for the self-diffusion. This is because the transport diffusion is measured for a small concentration gradient. For large L the particle flux becomes very small, and the error bars on the transport diffusion are very large. This is in contrast to D_s, where a concentration gradient of labeled particles is applied, which can be made arbitrarily high (100% in the left reservoir and 0% in the right reservoir). The problem of a very small labeled particle flux occurs much later compared to the transport diffusion. We have therefore not studied the length dependence of D_t for large lengths. For practical purposes one can assume that D_t has converged at $L \approx 20$, as can be seen from Figure 2.6.

We have also performed simulations in two- and three-dimensional systems. If periodic boundary conditions are imposed in the y and z directions, convergence to the limit of large system size is remarkably fast. An example of this convergence is shown in Figure 2.7.

2.4.3 Determination of the error bars

The error bars are determined as follows. We measure the value of the self- and transport diffusion each 10^8 Monte Carlo steps and store these values in a list A. Error bars are found by calculating $\overline{\sigma} = \sqrt{\langle \delta A^2 \rangle / n}$, where n is the number of elements in the list and

$$\langle \delta A^2 \rangle = \frac{1}{n-1} \sum_{i=1}^{n} (A_i - \langle A \rangle)^2, \tag{2.26}$$

with $\langle A \rangle$ the average of the list. The error bars have value $\langle A \rangle \pm \overline{\sigma}$. The error bars are generally encompassed by the symbol sizes. If this is not the case they have been included in the Figures. The error bars for Figures 5.1, 5.3, and 5.4 were measured differently. Four different diffusion coefficients were simulated, and the maximum and minimum values were taken as the error bars.

2.5 Related work

Crystalline nanoporous materials exist in a variety of forms. One commonly distinguishes between channel-type and cage-type structures [46]. We refer to the supplementary material of [47] for an overview of a representative subset of these materials. Channel-type structures consist of straight channels, which are either interconnected in a network or disconnected one-dimensional lines. A notable example is MFI [48], which is used in many commercial petrochemical and separation processes. Cage-type materials consist of cages separated by windows. A distinction can be made between materials with window sizes comparable to the cage size and those with window sizes that are significantly smaller. In the latter case, the size of the window is often comparable to the size of the guest molecules diffusing in the material. Our model is inspired by cage-type nanoporous materials connected by narrow windows. An example is Linde Type A (LTA), whose applications include paraffin cracking and use in water softeners. Another prominent example is MOF ZIF-8. It has shown potential for the separation of carbon dioxide and methane [49, 50], a necessary step in the refinement of natural gas.

Given their great technological and fundamental importance, it is no surprise that these materials are widely studied. Furthermore, the structure of the cage-type materials naturally suggests a coarse-graining procedure like the one we perform. In this Section, we give a short overview of the most relevant literature regarding the diffusion. Relevant work on equilibrium properties is discussed in Section 3.2. For a more general introduction on the modeling of diffusion in nanoporous materials we refer to [15].

2.5.1 Transition-state theory models

Analytical TST calculations

An early application of TST to diffusion in cage-type materials can be found in [51, 52]. One calculates the average jump rate of a particle from TST. It is assumed that subsequent particle jumps are uncorrelated. The self- and Maxwell-Stefan diffusion are

then equal to each other by construction. The self-diffusion is predicted by [Eq. (4.42) in [15])]

$$D_s = \frac{\lambda^2}{h} \frac{p}{\langle n \rangle} \frac{f^+}{f_g} \exp\left(-\frac{E_0 - U_0}{kT}\right). \tag{2.27}$$

f^+ and f_g are the molecular partition functions (i.e., without translational degrees of freedom) of a molecule in, respectively, the window and the free gas phase. p is the pressure of the reservoir, E_0 is the energy difference between the state in the cavity and in the window, and U_0 is the difference in the zero energy levels between the free gas phase and the absorbed state.

From Eq. (2.27) one can rationalize several experimental results, cf. Chapter 16 in [15]. Particle diffusion constitutes a case of activated diffusion over a barrier. One therefore expects, as predicted by the exponential factor in Eq. (2.27), that the diffusion coefficients show Arrhenius ($\propto 1/T$) behavior. This is indeed observed experimentally. Furthermore, larger molecules or smaller windows make it less likely a particle occupies the transition state, i.e., f^+ decreases. A slower diffusion for larger particles or smaller windows is indeed observed. By a calculation of the partition functions one was able to predict the correct order of magnitude of the diffusion at infinite temperature of several light molecules [53].

From molecular dynamics to random walks

A very popular approach to the understanding of diffusion in nanoporous materials are molecular dynamics (MD) simulations [16, 54]. Diffusion in cavity-type materials with narrow windows is a process of activated diffusion: particles spend a long time in a cavity before they jump to a neighboring cavity. A standard MD simulation therefore spends a lot of computational time on the "uninteresting" situation of the particles sitting in the cavities. This issue can be resolved by performing short MD simulations which, based on transition-state theory techniques, allow to compute the jump rates between the cavities. Standard TST techniques can be straightforwardly applied to diffusion at low loadings, when different particles have negligible influence on each other [55, 56]. The extension to high loading is non-trivial.

A first attempt to produce a TST scheme that quantitatively reproduces MD results for the self-diffusion at arbitrary loadings was undertaken by Tunca and Ford [57–59]. They assumed that interactions can be described by a free energy function that depends on the number of particles in a cavity and in its neighboring cavities. The jump rates k_{nm} were determined from TST simulations. This was achieved by closing off all cavities except A and B (as in Figure 2.2). These jump rates were employed in a kMC simulation to determine the self-diffusion. Their attempt to quantitatively reproduce the self-diffusion was not completely successful: some discrepancy between MD and TST calculations persisted. The similarities with our model are the consideration of free energies which depend solely on the particle numbers in the cavities and the use of kMC simulations with rates k_{nm}. Because the question was about the quantitative reproduction of MD results, they only considered one parameter set (one type of interaction). They also only studied the self-diffusion.

A quantitative agreement with MD simulations was obtained by Beerdsen, Dubbeldam, Smit, and Vlugt [60, 61]. They computed the effective hopping rate of a single particle. Quantitative agreement with MD simulations was achieved by taking into

account interactions with all neighboring cavities (not only A and B), and allowing for simultaneous jumps of other particles during the TST simulation. Since one assumed that subsequent particle jumps are uncorrelated, the self-diffusion could be calculated directly from the effective hopping rate. By considering all other particles as the environment and integrating over these interactions, the free energy of a single particle as a function of its position in the cavity can be calculated, see, e.g., Figure 2 from [60]. This position-dependent free energy allows for an understanding of the concentration-dependence of the self-diffusion.

2.5.2 Lattice gas models

Cellular automata

A lattice gas approach that most resembles our model is found in the work of Pazzona, Demontis, and Suffritti [62–65]. A lattice of connected cavities is considered, where each cavity can contain between zero and $n_{\max}$ particles. The difference in setup is that different cavities are connected via another lattice site, which can maximally contain one particle. Introducing such sites has the advantage of incorporating the decreased probability of moving to a cavity that is already highly occupied. It however also introduces extra parameters in the model. The updating is performed according to a cellular automaton approach [62, 63]. Therefore, despite the similarity in setup, the dynamical rules are very different compared to our model. Furthermore, as with all the works discussed up to now, the transport diffusion is not studied.

Other lattice gas approaches

A very popular approach is to consider a lattice where each site can contain maximally one particle, see e.g. [66–70]. Reed and Ehrlich studied such a lattice gas with nearest neighbor interactions in the context of surface diffusion [71, 72]. The application to zeolites was given by Krishna, Paschek, and Baur [73].

A lattice that can contain at most one particle per site and does not interact with other particles is called a simple exclusion process (SEP) in the physics literature. This model has been studied extensively, for example in the context of nonequilibrium statistical mechanics [74]. If one allows multiple particles per site and defines a set of jump rates that depend only on the particle numbers of the two participating sites, one has a generalized exclusion process (GEP) [75]. Such systems are studied in the mathematical physics literature [76]. Our model constitutes a GEP with a thermodynamic interpretation for the rates.

2.6 Conclusion

Inspired by diffusion in cage-type nanoporous materials, we have introduced a lattice model of interacting particles. The dynamics is Markovian and is simulated using kinetic Monte Carlo. The rates, which are used as input in the simulations, are calculated from transition-state theory. Both the self- and transport diffusion can be numerically determined from a straightforward procedure. Finally, we have briefly discussed other similar models.

Chapter 3

Equilibrium properties

Before turning to the diffusive properties, we study the equilibrium behavior of the model. The effect of $f(n)$ on fluctuations in particle number, and the equivalence of a concave $f(n)$ and clustering, is discussed. An investigation of particle clustering in porous materials using MD simulations can be found in Refs. [30–32]. If particles cluster the inverse thermodynamic factor Γ^{-1} is larger than 1, and there are steep adsorption isotherms. Porous materials are classified by the characteristic dimensions of their structure. If the pore dimensions are smaller than 2 nm, then the material is called microporous; if the dimensions are between 2 and 50 nm, then it is called mesoporous; and even larger pores are called macroporous. Steep isotherms and $\Gamma^{-1} > 1$ are more common in macro- and mesoporous materials than in microporous materials, i.e., the more confining the geometry the less likely particle clustering occurs. All these features are present in our model and can be understood from the shape of the interaction free energy, as discussed in this Chapter.

3.1 Fluctuations in particle number

Fluctuations in particle number are encoded in the thermodynamic factor, Eq. (2.20). We discuss the behavior of Γ^{-1} instead of Γ because the latter goes to infinity at maximum loading, making it more difficult to interpret graphically. Let us first consider noninteracting particles with zero volume, i.e., $f(n) = 0$ and $n_{\max} = \infty$. The distribution $p_n^{\text{eq}}(\mu)$ is then a Poisson distribution,

$$p_n^{\text{eq}}(\mu) = \frac{\langle n \rangle^n}{n!} e^{-\langle n \rangle}, \tag{3.1}$$

for which $\langle n^2 \rangle - \langle n \rangle^2 = \langle n \rangle$ and $\Gamma = 1$ at all loadings. The change in variance $\langle n^2 \rangle - \langle n \rangle^2$ is caused by the convexity versus concavity of $f(n)$. For better insight into the dependence of the equilibrium distributions on this convexity or concavity of $f(n)$ we consider the grand potential $\Omega(n, \mu)$, which we write as

$$\Omega(n, \mu) = F^{\text{id}}(n) + f(n) - \mu n, \tag{3.2}$$

or, by defining the constant $\mu_0 \equiv kT \ln \left(V/\Lambda^3 \right)$,

$$\Omega(n, \mu) = kT \ln (n!) + f(n) - (\mu + \mu_0)\, n. \tag{3.3}$$

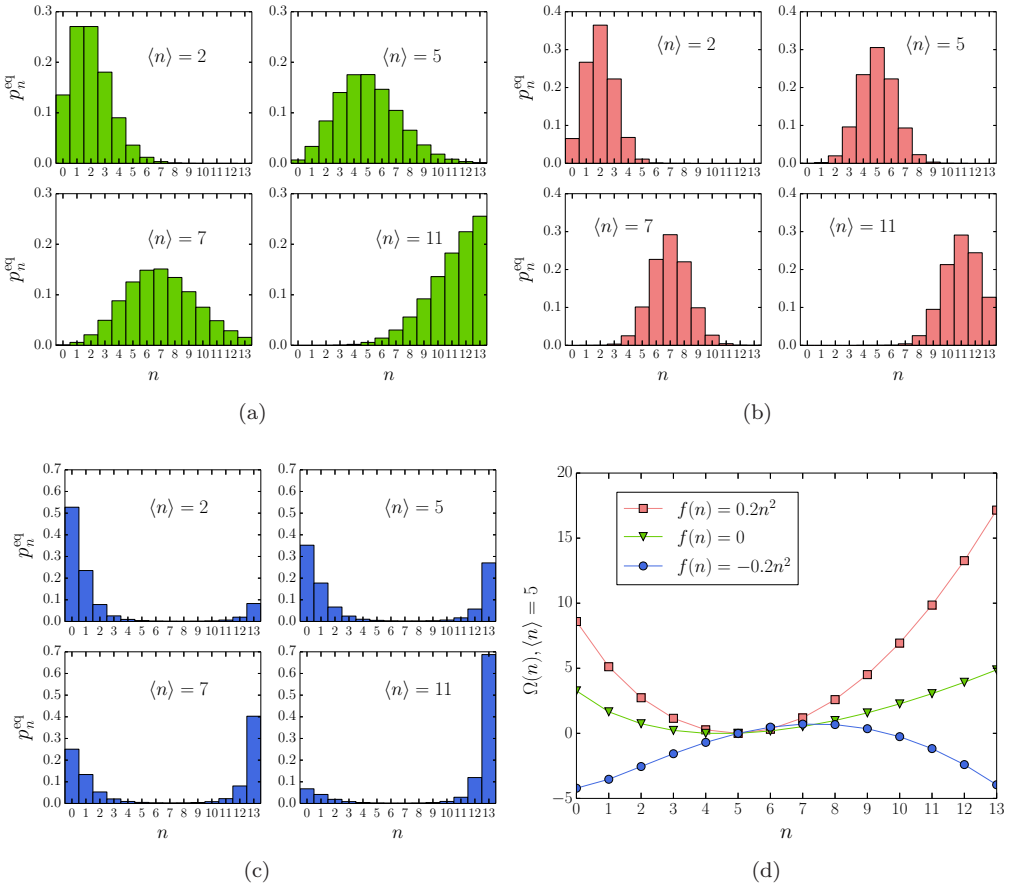

Figure 3.1: The probability distribution of cavity occupation $p_n^{\rm eq}$, Eq. (2.1), at different loadings and with $n_{\max} = 13$, for (a) $f(n) = 0$ (b) $f(n) = 0.2n^2$ (c) $f(n) = -0.2n^2$. (d) $\Omega(n)$ for the different interactions, at $\langle n\rangle = 5$. The lines are a guide to the eye.

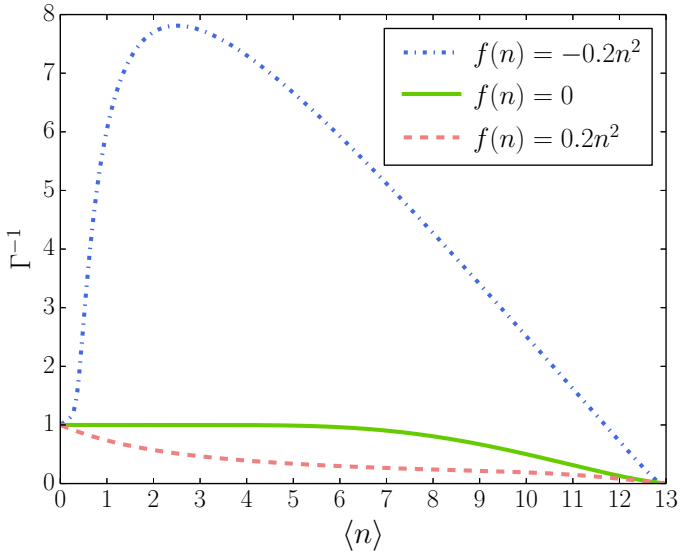

Figure 3.2: The inverse thermodynamic factor $\Gamma^{-1} = \left(\langle n^2 \rangle - \langle n \rangle^2\right) / \langle n \rangle$, for $n_{\max} = 13$ and different interactions.

μ_0 changes the chemical potential for which a certain loading is achieved; it does not change the behavior of $\Omega(n, \mu)$ at a given loading. Because we only consider isothermal systems kT is a constant, which we take to be equal to 1. We discuss three situations: no interactions $f(n) = 0$; convex interactions, with as an example $f(n) = 0.2n^2$; and concave interactions, with as an example $f(n) = -0.2n^2$. For all interactions we take $n_{\max} = 13$, corresponding to $f(n) = \infty$ for $n > n_{\max}$.

To understand the effect of introducing an $n_{\max}$, we consider the situation $f(n) = 0$ and $n_{\max} = 13$. The probability distributions of cavity occupation p_n^{eq} at different loadings are plotted in Fig. 3.1a. As long as $p_{n_{\max}}^{\text{eq}} \approx 0$, p_n^{eq} is equal to the Poisson distribution Eq. (3.1) and $\Gamma = 1$. Once the probability to be full becomes nonzero the variance decreases compared to the Poisson distribution, resulting in $\Gamma^{-1} < 1$; see Fig. 3.2.

To understand the change in variance for different interactions we plot $\Omega(n, \mu)$ as a function of n, at the chemical potentials for which $\langle n \rangle = 5$; see Fig. 3.1d. For graphical clarity the three curves are shifted vertically so $\Omega(5) = 0$. For $f(n) = 0$ the minimum of $\Omega(n)$ lies at $n = \langle n \rangle$. All other values of $\Omega(n)$ are higher, because $\Omega(n) = kT \ln(n!) - (\mu + \mu_0)n$ is a convex function of n. By adding a convex $f(n)$, $\Omega(n)$ increases faster around its minimum, and therefore all states that differ from $n = \langle n \rangle$ become less likely compared to $f(n) = 0$. This is clear from the probability distributions of cavity occupation for $f(n) = 0.2n^2$; see Fig. 3.1b. As a result, $\Gamma^{-1} < 1$ at all loadings, cf. Fig. 3.2. An example of a convex $f(n)$, and hence a concave $z(n)$, is discussed in Ref. [59], where it was attributed to excluded volume interactions between the methane molecules.

Adding a concave $f(n)$ gives the opposite behavior. $\Omega(n)$ increases more slowly around the average, and occupations that differ from the average become more likely

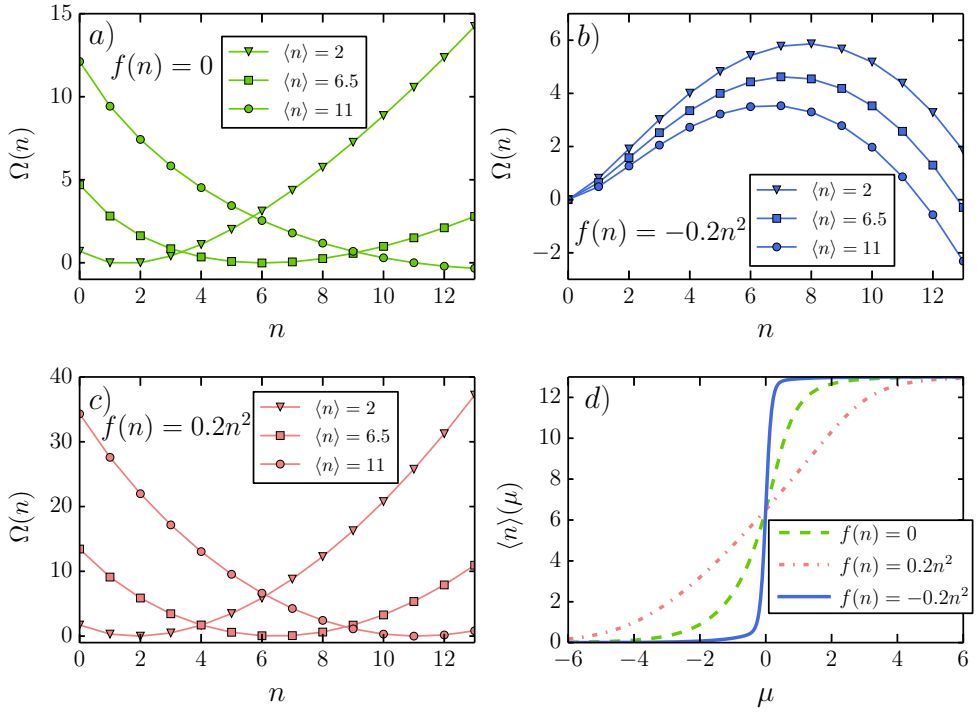

Figure 3.3: $a), b), c)$ $\Omega(n)$ for different interactions and loadings, with $n_{\max} = 13$. For $f(n) = 0$ and $f(n) = 0.2n^2$ the curves are shifted vertically so that $\Omega(\langle n\rangle) = 0$. For $f(n) = -0.2n^2$ the curves are shifted vertically so that $\Omega(0) = 0$. The lines are a guide to the eye. $d)$ Adsorption isotherms $\langle n\rangle(\mu)$. The curves are shifted horizontally so that $\langle n\rangle(0) = 0.5n_{\max}$.

compared to $f(n) = 0$. For a very concave $f(n)$, $\Omega(n)$ no longer has a single minimum around $n = \langle n\rangle$; there are two minima, at $n = 0$ and $n = n_{\max}$; see Fig. 3.1d. The probability distributions of cavity occupation for $f(n) = -0.2n^2$ are shown in Fig. 3.1c. The particles cluster: The cavities are mostly empty or full. As a result, $\Gamma^{-1} > 1$ for low and medium loadings, after which the effect of $n_{\max}$ becomes dominant; cf. Fig 3.2. An example of a concave contribution to $f(n)$ is the energy of a cluster of particles feeling short-range attractive interactions, which scales as $\propto n^{2/3}$ for large n [77]. An example of clustering is found for particles undergoing hydrogen bonding [30].

3.2 Adsorption isotherm

Adsorption isotherms give the equilibrium concentration of particles in the system as function of, e.g., the pressure or chemical potential of the reservoir. Studies of adsorption in porous materials which use the same model assumptions as presented in this paper have been performed by several authors. In these studies one tries to predict

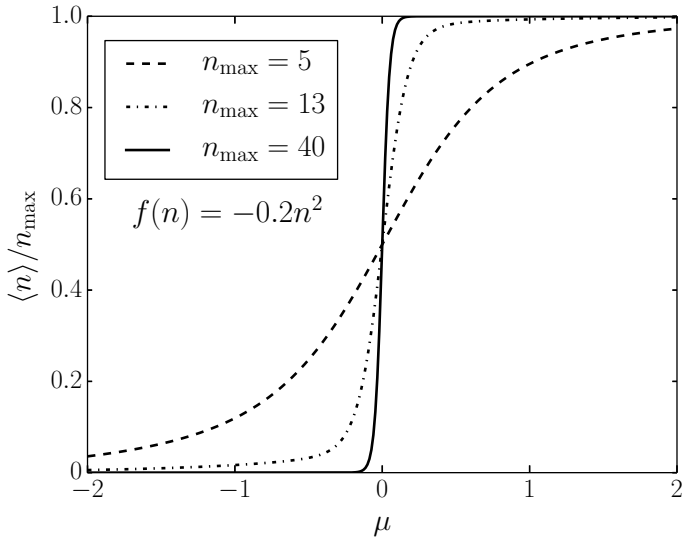

Figure 3.4: Adsorption isotherms $\langle n\rangle(\mu)/n_{\max}$ for different values of $n_{\max}$, for the interaction $f(n) = -0.2n^2$. The curves are shifted horizontally to have $\langle n\rangle(0) = 0.5n_{\max}$.

and explain the behavior of the adsorption isotherm, using only a few microscopic parameters that describe the particle-particle and particle-cavity interaction. One of the first such analyses was performed by Ruthven [78]. Similar studies have been performed both analytically [65, 79–83] and numerically [59, 84, 85]. We refer to Ref. [86] for an introduction. We discuss here the qualitative influence of $f(n)$ and $n_{\max}$ on the adsorption isotherm. The particle concentration is equal to $\langle n\rangle/\lambda^d$ (with d the dimension). Since the term λ^d only rescales the adsorption isotherm by a constant, we study $\langle n\rangle(\mu)$.

The adsorption isotherms $\langle n\rangle(\mu)$ for the three considered interactions are plotted in Fig. 3.3d. The grand potentials at different loadings are shown in Figs. 3.3a,b,c. The adsorption isotherm for the concave $f(n)$ is steeper than the one for $f(n) = 0$, which is steeper still than the one for the convex $f(n)$. Such behavior can be understood from $\langle n\rangle(\mu)$:

$$\frac{d\langle n\rangle}{d\mu} = \beta\left(\langle n^2\rangle - \langle n\rangle^2\right) = \beta\langle n\rangle\Gamma^{-1}. \tag{3.4}$$

A concave $f(n)$ leads to a larger value of Γ^{-1}, which means a steeper adsorption isotherm. Steep isotherms occur if there is a first-order phase transition, for example, when there is capillary condensation [87]. They have also been found for systems where the particles cluster; see Ref. [31] and references therein. The connection among clustering, first-order phase transitions, and steep isotherms can be understood from Fig. 3.3. For noninteracting and repulsive particles (Figs. 3.3a,c) only the average concentration $\langle n\rangle$ is stable (i.e., a local minimum). Increasing the chemical potential gradually shifts this local minimum to higher concentrations. For the concave $f(n)$, Fig. 3.3b, there are in contrast two stable concentrations, at $n = 0$ and $n = n_{\max}$.

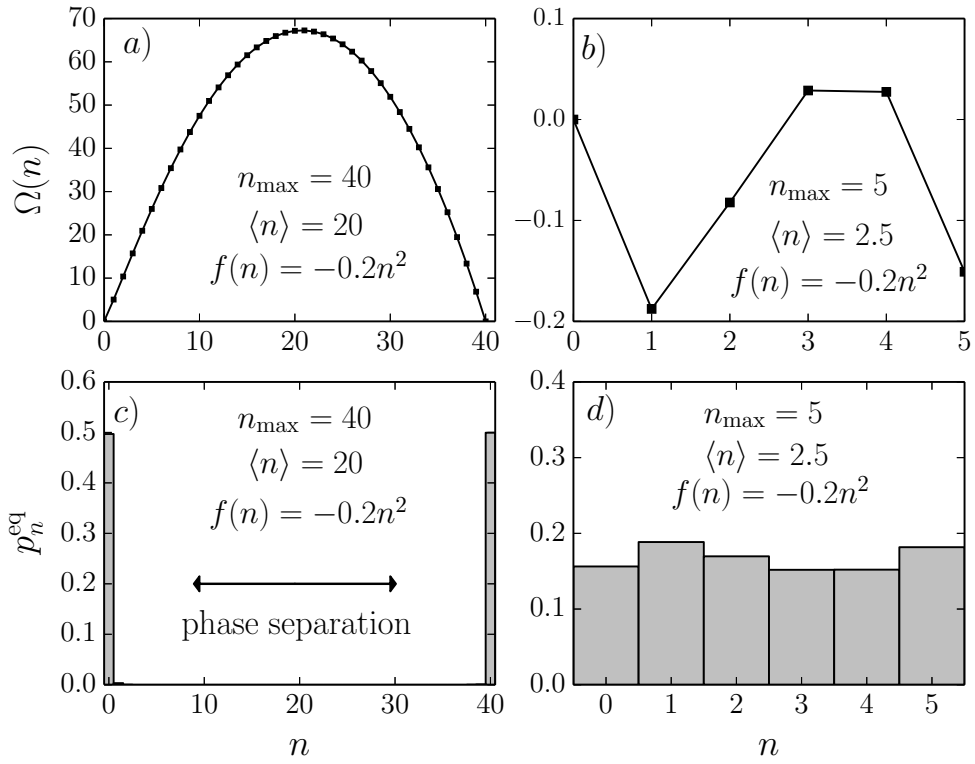

Figure 3.5: *a*) $\Omega(n)$ and *c*) $p_n^{\rm eq}$, for $n_{\rm max} = 40$, $\langle n \rangle = 20$, and $f(n) = -0.2n^2$. *b*) $\Omega(n)$ and *d*) $p_n^{\rm eq}$ for $n_{\rm max} = 5$, $\langle n \rangle = 2.5$, and $f(n) = -0.2n^2$.

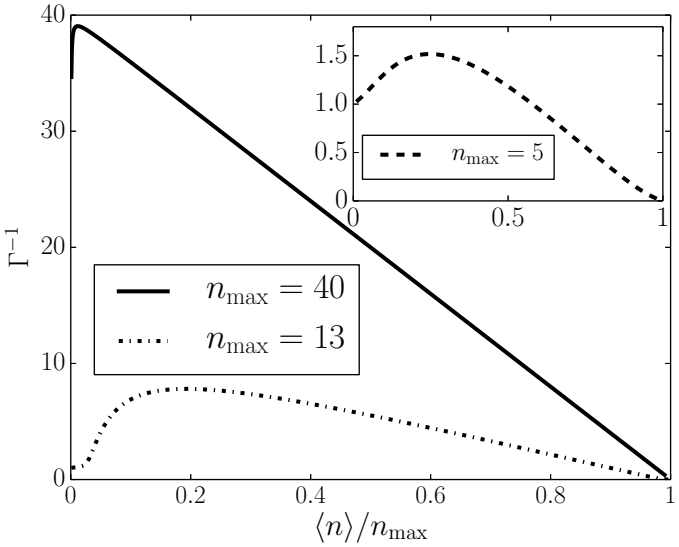

Figure 3.6: The inverse thermodynamic factor $\Gamma^{-1} = \left(\langle n^2 \rangle - \langle n \rangle^2\right) / \langle n \rangle$, for different $n_{\max}$ and $f(n) = -0.2n^2$.

Increasing the chemical potential causes a sudden shift of the global minimum from $n = 0$ to $n = n_{\max}$, resulting in a steep isotherm.

While stepped isotherms are commonly encountered in mesoporous materials, they are quite rare in microporous materials [31]. This can be seen as the result of the confinement, which prevents the formation of stable macroscopic phases [87–89]. We discuss how such behavior is reproduced in our model.

We take the diameter of the cavities as the characteristic dimension of the system (i.e., $n_{\max}$). Consider the same type of particles in materials with cavities of different size. The smaller the volume of the cavities the lower $n_{\max}$. To study the transition from micro- to macroporous for clustering particles, we consider the interaction $f(n) = -0.2n^2$, for $n_{\max} = 5, 13$, and 40. The adsorption isotherms are presented in Fig. 3.4. Their steepness decreases with decreasing cavity size. For an interpretation of this behavior we plot p_n^{eq} and $\Omega(n)$ at loading $\langle n \rangle / n_{\max} = 0.5$, for $n_{\max} = 40$ and $n_{\max} = 5$ in Fig. 3.5. For $n_{\max} = 40$ a stable cluster consists of 40 particles, and the thermodynamic barrier between the stable phases $n = 0$ and $n = 40$ is very large, cf. Fig. 3.5a. Fluctuations between the two phases are highly unlikely, as can be seen from p_n^{eq} in Fig. 3.5c. This resembles the situation where there is a macroscopic phase separation (i.e., in the thermodynamic limit), where moving on the infinitely steep part of the adsorption isotherm corresponds to changing the relative portion of the two phases of the system. For $n_{\max} = 5$ the maximum size of a cluster is 5 particles. Such a cluster is easily broken by fluctuations. In fact, the grand potential does not show the typical structure of two stable minima [see Fig. 3.5b], and the adsorption isotherm shows no real steepness. $n_{\max} = 13$ is an intermediate case of these two situations; see Figs. 3.1c and 3.3b. The inverse thermodynamic factors are plotted in Fig. 3.6. For $n_{\max} = 40$, $\Gamma^{-1}(\langle n \rangle)$ is approximately a straight line between $\Gamma^{-1}(0) \approx n_{\max}$ and

$\Gamma^{-1}(n_{\max}) = 0$. This can be understood by making the approximation that cavities are either empty or full. In this case, $p_{n_{\max}} = \langle n \rangle / n_{\max}$, $p_0 = 1 - \langle n \rangle / n_{\max}$, and

$$\Gamma^{-1}(\langle n \rangle) = n_{\max} \left(1 - \frac{\langle n \rangle}{n_{\max}} \right). \tag{3.5}$$

If particle clustering occurs the inverse thermodynamic factor goes from showing almost no increase above 1 for microporous materials, to a straight line between $n_{\max}$ at $\langle n \rangle = 0$ and 0 at $\langle n \rangle = n_{\max}$ for macroporous materials, cf. Fig. 3.6.

3.3 Conclusion

We conclude that the effect of interactions can be best understood by considering whether the interaction free energy is convex or concave. Repulsive particle interactions lead to a convex $f(n)$ and a homogeneous particle distribution in the system. Attractive particle interactions give a concave $f(n)$ which leads to particle clustering in the cavities. The equilibrium behavior observed experimentally and in MD simulations for clustering particles can then easily be understood within the context of our model. The above discussion applies to all lattice models where the same assumption of a time-scale separation between inter- and intra-cavity dynamics is made [86]. Having discussed the equilibrium properties we now turn to the main subject of this thesis, namely the different diffusion coefficients and how they are influenced by interactions.

Chapter 4

Diffusion: analytical results

We calculate and discuss the analytical results that were obtained for the self- and transport diffusion. The uncorrelated result is found for systems of length $L = 1$. The final expressions for D_s and D_t are remarkably simple. The uncorrelated result is also found for zero-range processes (ZRPs). In a ZRP the transition rates only depend on the number of particles in the departing cavity, i.e. the rates must be of the form $k_{nm} = k_n$. The steady state distribution of a ZRP can be interpreted as the generalization of the $L = 1$ case to arbitrary lengths. Finally, we discuss exact solutions for $L = 2$ and $n_{\max} = 2$, which includes correlations.

4.1 Length $L = 1$

We derive an exact expression for D_t and D_s, in a limiting situation where correlations between particle numbers in different cavities are absent. Consider a system consisting of three cavities, with n_l, n and n_r specifying the number of particles inside the left, middle and right cavity, respectively, as depicted in Figure 4.1. The left (right) cavity is connected to an equilibrium reservoir at a fixed chemical potential μ_l (μ_r) and temperature T. These reservoirs try to impose their equilibrium distribution, Eq. (2.1), to the cavity that is connected to them. This is the model of Section 2.1, with more general equilibrium reservoirs at the boundaries. In the limit in which the exchange rates with the middle cavity are small compared to the exchange rates with the reservoirs, the left and right cavity are effectively uncorrelated from the middle cavity, and are characterized by the equilibrium probability distribution $p^{\mathrm{eq}}_{n_l}(\mu_l)$ and $p^{\mathrm{eq}}_{n_r}(\mu_r)$, respectively. An explicit calculation for this separation of time-scales is given in Appendix C. This setup allows us to obtain exact analytical results at arbitrary particle density. The probability distribution p_n for the middle cavity obeys the following master equation:

$$\dot{p}_n = k^+_{n-1} p_{n-1} + k^-_{n+1} p_{n+1} - \left(k^+_n + k^-_n\right) p_n, \tag{4.1}$$

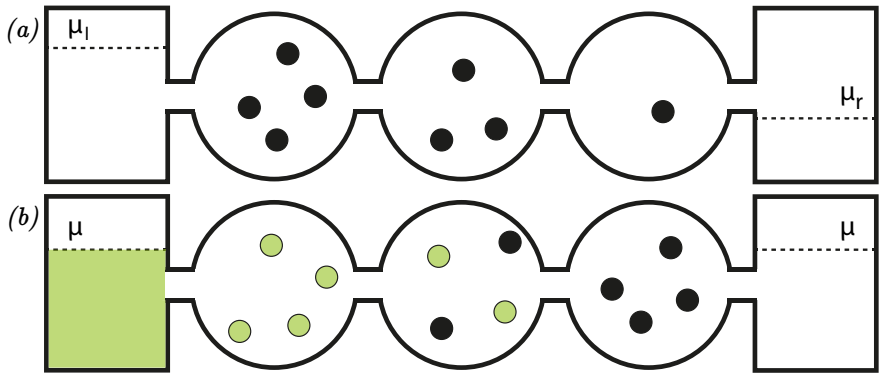

Figure 4.1: The model with general particle reservoirs. (a) Transport diffusion: a concentration gradient shows a current. (b) Self-diffusion: a concentration gradient of labeled particles is introduced under overall equilibrium conditions.

with k_n^+ and k_n^- the rates to add or remove a particle from the middle cavity containing n particles:

$$k_n^+ = \sum_{n_l} p_{n_l}^{\rm eq}(\mu_l) k_{n_l n} + \sum_{n_r} p_{n_r}^{\rm eq}(\mu_r) k_{n_r n} \tag{4.2}$$

$$k_n^- = \sum_{n_l} p_{n_l}^{\rm eq}(\mu_l) k_{n n_l} + \sum_{n_r} p_{n_r}^{\rm eq}(\mu_r) k_{n n_r}. \tag{4.3}$$

The particle flux and concentration difference between the left and middle cavity read:

$$j(\mu_l, \mu_r) = \sum_{n, n_l} \left(k_{n_l n} - k_{n n_l}\right) p_{n_l}^{\rm eq}(\mu_l) p_n, \tag{4.4}$$

$$dc(\mu_l, \mu_r) = (1/\lambda) \sum_{n, n_l} (n - n_l) p_{n_l}^{\rm eq}(\mu_l) p_n, \tag{4.5}$$

where λ is the center-to-center distance between cavities. The transport diffusion D_t, quantifying the linear response of j with respect to dc, is found from the ratio $-j/(dc/\lambda)$ in the limit $\delta = (\mu_l - \mu_r)/2 \to 0$. Introducing the average chemical potential $\mu = (\mu_l + \mu_r)/2$, one finds for Eqs. (4.2) and (4.3) up to linear order in δ:

$$k_n^+ = 2 \sum_m p_m^{\rm eq}(\mu) k_{mn}, \quad k_n^- = 2 \sum_m p_m^{\rm eq}(\mu) k_{nm}. \tag{4.6}$$

One concludes from Eq. (4.1) that at this order in δ, the steady state solution of the master equation is given by $p_n = p_n^{\rm eq}(\mu)$. The corresponding current and concentration difference are obtained from the expansion of Eqs. (4.4) and (4.5) to first order in δ, see Appendix D, resulting in

$$D_t(\mu) = \frac{\lambda^2 \sum_{n,m} p_n^{\rm eq}(\mu) p_m^{\rm eq}(\mu) k_{nm}}{\langle n^2 \rangle - \langle n \rangle^2} \equiv \frac{\lambda^2 \langle k \rangle}{\langle n^2 \rangle - \langle n \rangle^2}, \tag{4.7}$$

where $\langle \cdot \rangle$ denotes the average over $p^{\rm eq}(\mu)$.

We next turn to the self-diffusion, using the labeling procedure discussed in Section 2.3. Since the final expression for D_s does not depend on the labeling percentages, we consider a simple case: all particles in the left reservoir are labeled, those in the right reservoir remain unlabeled. As a result, all particles in the left and none in the right cavity are labeled. The state of the middle cavity is now described by two numbers, n (total number of particles) and n^*, the number of labeled particles. The corresponding steady state probability distribution p_{n,n^*} is:

$$p_{n,n^*} = p_n^{\mathrm{eq}}(\mu)\frac{n!}{n^*!(n-n^*)!}\frac{1}{2^n}. \tag{4.8}$$

The flux of labeled particles and concentration difference between the left and middle reservoir read:

$$\begin{aligned} j^* &= \sum_{n_l,n,n^*}\left(k_{n_l n} - k_{n n_l}\frac{n^*}{n}\right)p_{n,n^*}p_{n_l}^{\mathrm{eq}}(\mu) = \frac{\langle k\rangle}{2} \\ dc^* &= (1/\lambda)\sum_{n_l,n,n^*}(n^*-n_l)p_{n,n^*}p_{n_l}^{\mathrm{eq}}(\mu) = -\frac{\langle n\rangle}{2\lambda}. \end{aligned} \tag{4.9}$$

Hence, the self-diffusion $D_s = -j^*/(dc^*/\lambda)$ reads

$$D_s(\mu) = \lambda^2\frac{\langle k\rangle}{\langle n\rangle}. \tag{4.10}$$

A derivation of self-diffusion for a general concentration difference of labeled particles is given in Appendix E. Equations (4.7) and (4.10) are valid at all values of the concentration and can be calculated for any interaction. From Eqs. (4.7) and (4.10), one finds for the ratio of D_t and D_s:

$$\frac{D_t(\mu)}{D_s(\mu)} = \frac{\langle n\rangle}{\langle n^2\rangle - \langle n\rangle^2} = \frac{\langle n\rangle}{\mathrm{Var}(n)} = \Gamma(\mu), \tag{4.11}$$

where $\Gamma(\mu)$ is the thermodynamic factor Eq. (2.20), an equilibrium property. Equation (4.11) can be derived by a general argument, when correlations are ignored [44, 90].

4.2 Zero-range processes

Exact expressions for transport and self-diffusion are possible when the model satisfies the criteria of a zero-range process [91]. Because the rates are of the form $k_{nm} = k_n$, the particle is not aware of the state of the cavity it moves to. Clearly this can only be true if the number of particles at each site is unlimited, i.e. $n_{\max} = \infty$. Local detailed balance then gives the following condition:

$$k_n\frac{p_n^{\mathrm{eq}}(\mu)}{p_{n-1}^{\mathrm{eq}}(\mu)} = k_{m+1}\frac{p_{m+1}^{\mathrm{eq}}(\mu)}{p_m^{\mathrm{eq}}(\mu)}. \tag{4.12}$$

Since this condition must hold for all values of m and n, both sides of the equation must be equal to a function $g(\mu)$. Using Eq. (2.1) one finds:

$$k_n = g(\mu)e^{-\beta\mu}ne^{\beta[f(n)-f(n-1)]}. \tag{4.13}$$

Since k_n only depends on particle interactions in the cavity it must be independent of the chemical potential of the reservoir. As a result $g(\mu) = \nu e^{\beta\mu}$. The model is therefore a ZRP for the rates:

$$k_n = \nu n e^{\beta[f(n)-f(n-1)]}. \tag{4.14}$$

As discussed in Section 2.1, a linear term in the free energy is not relevant, and can be absorbed in ν. The transition rates describing the exchange of particles with the reservoirs follow directly by substituting Eq. (4.14) in Eq. (2.6):

$$k_n^{r,+}(\mu) = \nu e^{\beta\mu}; \quad k_n^{r,-}(\mu) = k_n. \tag{4.15}$$

Consider $p_{n_1,n_2,\ldots,n_L}(\mu_l, \mu_r, t)$, the probability for the system to be in state $(n_1, n_2, \ldots, n_L)$ at time t, with n_i the number of particles in the ith cavity. For a ZRP the stationary distribution $p_{n_1,n_2,\ldots,n_L}(\mu_l, \mu_r)$ can be calculated exactly:

$$p_{n_1,n_2,\ldots,n_L}(\mu_l, \mu_r) = \prod_{i=1}^{L} p_{n_i}^{\mathrm{eq}}(\mu_i), \tag{4.16}$$

with

$$\mu_i = \beta^{-1} \ln \left[e^{\beta\mu_l} - \frac{i}{L+1} \left(e^{\beta\mu_l} - e^{\beta\mu_r} \right) \right]. \tag{4.17}$$

The stationary state is found by postulating Eq. (4.16) as the solution, and using this solution in the master equation. This results in a set of equations for μ_i that depend on μ_l and μ_r, which can be solved recursively [92]. It is important to note here that it is not always possible for the system to reach a stationary state. For example attractive particles can condensate in the system, which continues to absorb particles from the reservoirs since $n_{\max} = \infty$. We refer to [92] for a derivation of Eq. (4.16) and a discussion on its range of validity. This type of interactions are excluded in the following discussion. The solution is a product measure: particle numbers in different cavities are uncorrelated, for all possible interactions. Performing a first order expansion in δ around $\delta = 0$, as explained in Section 4.1, one finds that μ_i decreases linearly between the cavities:

$$\mu_i = \mu + \delta \left(1 - \frac{2i}{L+1} \right). \tag{4.18}$$

From this result one can derive that D_t is equal to the uncorrelated result Eq. (4.7).

The self-diffusion coefficient of a ZRP can be calculated directly from the definition Eq. (2.14), see for example [93]. We succeeded to calculate D_s via the alternative method by introducing labeled particles in the system. The stationary solution is again a product measure:

$$p_{n_1,n_1^*,\ldots,n_L,n_L^*}(\mu, \alpha_l, \alpha_r) = \prod_{i=1}^{L} p_{n_i}^{\mathrm{eq}}(\mu) \binom{n_i}{n_i^*} \alpha_i^{n_i^*} (1-\alpha_i)^{n_i - n_i^*}, \tag{4.19}$$

with α_l and α_r the fraction of labeled particles in the left and right reservoir respectively and

$$\alpha_i = \alpha_l - (\alpha_l - \alpha_r) \frac{i}{L+1}. \tag{4.20}$$

The fraction of labeled particles decreases linearly between the cavities. The method of solution is analogous to the case without labeled particles [92]. One postulates Eq. (4.19) as the solution. Using Eq. (4.19) in the master equation gives a set of equations for α_i, of which the solution is Eq. (4.20). From Eq. (4.19) one can derive that D_s is equal to the uncorrelated result Eq. (4.10).

The obtained stationary states Eqs. (4.16) and (4.19) can be interpreted as generalizations of the $L = 1$ case of Section 4.1. Indeed, to calculate D_t and D_s from the stationary states one can take three neighboring cavities, consider the left and right cavity as reservoir cavities, and perform the same calculation as for the $L = 1$ case. This is however only possible for ZRPs. In general, correlations influence the stationary state.

4.3 Length $L = 2$ and $n_{\max} = 2$

The influence of correlations appear only for system sizes $L = 2$ and larger. However, for increasing system size L and $n_{\max}$ the resulting calculations quickly become unfeasible, even when making use of a symbolic calculator. We were able to calculate analytically the self- and transport diffusion for systems of length $L = 2$ and $n_{\max} = 2$, for the rates of Eq. (2.13). As follows from Eq. (2.13), adding a linear term to $f(n)$ does not influence the dynamics. As discussed in Section 2.1, the equilibrium statistics in function of particle concentration is also not influenced by a linear term in $f(n)$. Without loss of generality, we rescale the interaction free energy by $f(n) \to f(n) - n[f(1) - f(0)] - f(0)$, which makes $f(0) = f(1) = 0$. Both the equilibrium and dynamical quantities then only depend on $f(2)$. Putting $\beta \equiv 1$, $x \equiv e^{\mu}$, and $y \equiv e^{f(2)/2}$, the exact analytical results for D_t and D_s are

$$
\begin{aligned}
D_t = 2\Big(& x^5 + x^4(7+x)y + x^3(21+8x)y^2 + x^2(15+x(23+2x))y^3 + 2x(19+33x \\
& + 6x^2)y^4 + 2(10+x(17+5x))y^5 + 8(1+x)y^6\Big) \Big/ \Big(x^4(4+x) + x^3(4+x)(5+x)y \\
& + 2x^2(20+3x(6+x))y^2 + 2x(40+x(29+x(10+x)))y^3 + 4x(7+x)(1+2x)y^4 \\
& + 4(10+x(9+x))y^5 + 16(1+x)y^6\Big) \qquad (4.21)
\end{aligned}
$$

$$
\begin{aligned}
D_s = & \Big(2y^2(2x^7(1+y) + 64y^6(1+y)^2(5+2y) + x^6(2+30y+32y^2+9y^3) \\
& + 8xy^5(71+283y+274y^2+88y^3+8y^4) + x^5y(24+198y+227y^2+100y^3+8y^4) \\
& + x^4y^2(118+726y+958y^2+435y^3+64y^4) + 2x^2y^4(237+1309y+1604y^2+652y^3 \\
& + 72y^4) + x^3y^3(304+1686y+2371y^2+1030y^3+152y^4))\Big) \Big/ \Big(2x^8(1+y) + 128y^8 \\
& (1+y)^2(5+2y) + x^7(2+30y+38y^2+15y^3) + x^6y(26+212y+301y^2+178y^3 \\
& + 39y^4) + 16xy^6(40+127y+179y^2+186y^3+152y^4+40y^5) + x^5y^2(146+856y \\
& + 1314y^2+931y^3+354y^4+42y^5) + 2x^4y^3(214+991y+1692y^2+1434y^3+654y^4 \\
& + 154y^5+8y^6) + 4x^2y^5(108+681y+1081y^2+1448y^3+916y^4+248y^5+32y^6) \\
& + 2x^3y^4(298+1354y+2508y^2+2725y^3+1410y^4+384y^5+48y^6)\Big). \qquad (4.22)
\end{aligned}
$$

The exact and uncorrelated results for $f(2) = -2, 0, 2$, and 5 are plotted in Fig. 4.2. D_s has a minimum at $\langle n \rangle = 1$ for $f(2) = 5$ because the state $(n_1, n_2) = (1, 1)$ is very stable, and particles will not diffuse easily. The transport diffusion shows a maximum in this situation, because a particle that enters the system when it is in state $(n_1, n_2) = (1, 1)$ is "pushed out" again rapidly. The transport diffusion has a minimum for low and medium concentrations for $f(2) = -2$ because particles are attracted against the concentration gradient, see also Section 5.1.

Correlations always lower the self-diffusion compared to the uncorrelated result. This was checked analytically for all interactions. Correlations lower the transport diffusion almost always compared to the uncorrelated result, except for $\ln(2) < f(2) < \ln(9/4)$. For these interactions the transport diffusion is slightly higher than the uncorrelated result. The particle concentrations at which this occurs depends on the interaction. Because the effect is very small we do not plot this situation. It is an open question whether positive correlations for the transport diffusion also exist for systems with $L \uparrow \infty$, when the influence of the reservoir cavities is negligible.

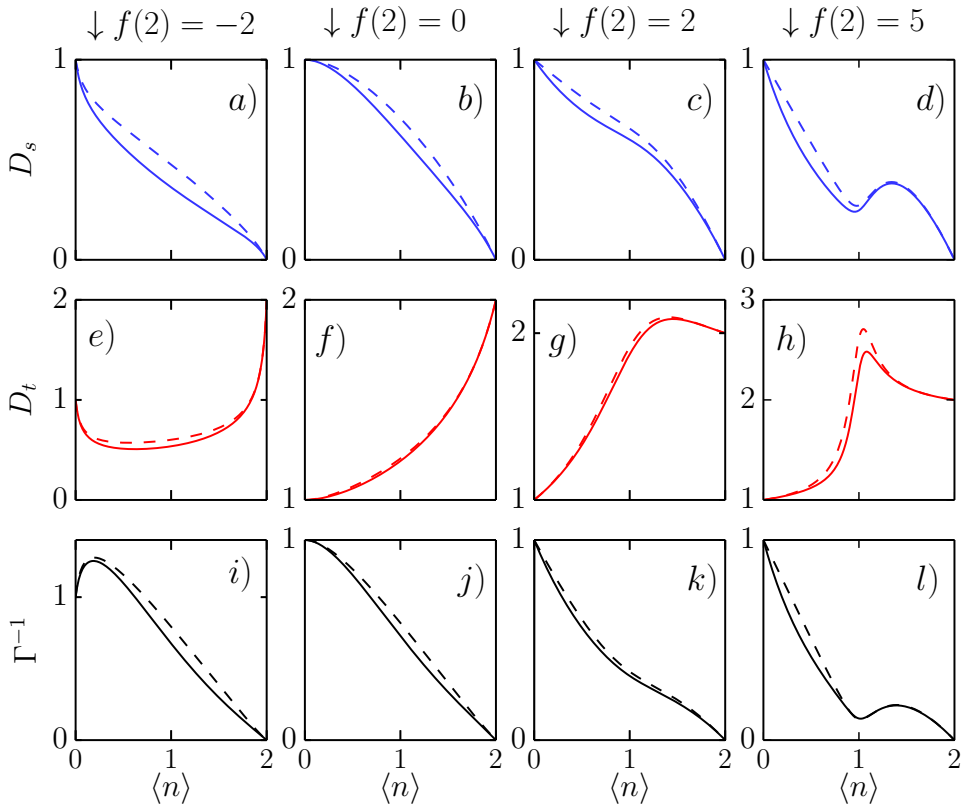

Figure 4.2: System of length $L = 2$, $n_{\max} = 2$, and the rates of Eq. (2.13). *a*), *b*), *c*), and *d*): self-diffusion D_s, exact (solid line) and uncorrelated (dashed line); *e*), *f*), *g*), and *h*): transport diffusion D_t, exact (solid line) and uncorrelated (dashed line); *i*), *j*), *k*), and *l*): Γ^{-1} (dashed line) and D_s/D_t (solid line), for respectively $f(2) = -2$, $f(2) = 0$, $f(2) = 2$, and $f(2) = 5$.

Chapter 5

Diffusion: numerical results

In an experiment of particle diffusion in a nanoporous material one found, for the first time, that the self-diffusion can exceed the transport diffusion; see the discussion in Section 1.2.2. In Section 5.1 we use our model to give a simple interpretation of this result. In Section 5.2 we show that, furthermore, one is able to reproduce the experimental data of the diffusion coefficients and the thermodynamic factor. An alternative derivation of the uncorrelated results for D_s and D_t is presented in Section 5.3. It allows for a better understanding of what it means to neglect correlations in the diffusion. In Section 5.4 we discuss the diffusion for the two rates of Eqs. (2.12) and (2.13), for different interactions. The effect of correlations is studied in detail. In Section 5.5 we examine the assumptions underlying our model and discuss when agreement with experiments and molecular dynamics simulations can be expected.

5.1 Relation of the self- and transport diffusion

Chmelik *et al.* measured the self- and transport diffusion of methanol and ethanol in a nanoporous material, MOF ZIF-8 [28]. At variance with previous experiments [94–99], it was found that the self-diffusion could exceed the transport diffusion. This was attributed to the strong influence of interparticle interaction. The experimental finding of D_s exceeding D_t was explained on the basis of MD simulations [30–32] as due to clustering of the particles.

Starting from our model, the connection between $D_s > D_t$ and clustering can be understood from a simple analytical argument. Since a concave $f(n)$ gives $\langle n^2\rangle - \langle n\rangle^2 > \langle n\rangle$ one finds from Eq. (4.11) that $D_s > D_t$ is possible only for clustering particles. A cavity can typically contain a limited number of particles $n \leq n_{\max}$. This corresponds to $f(n) = \infty$ for all $n > n_{\max}$, i.e., $f(n)$ is "infinitely convex" at $n_{\max}$. We conclude from the above argument that a concave section is a necessary, but not sufficient, condition for having $\langle n^2\rangle - \langle n\rangle^2 > \langle n\rangle$, i.e., for D_s to exceed D_t. One can give an intuitive explanation as to why a concave $f(n)$ promotes $D_s > D_t$. D_t is measured by a flux j. If $f(n)$ is concave, particles tend to cluster, which will mostly happen in cavities that are already high in particle number. This causes the particles to be "pulled back" towards the region of higher concentration. The net effect is a force in the direction of higher concentration, lowering the particle flux.

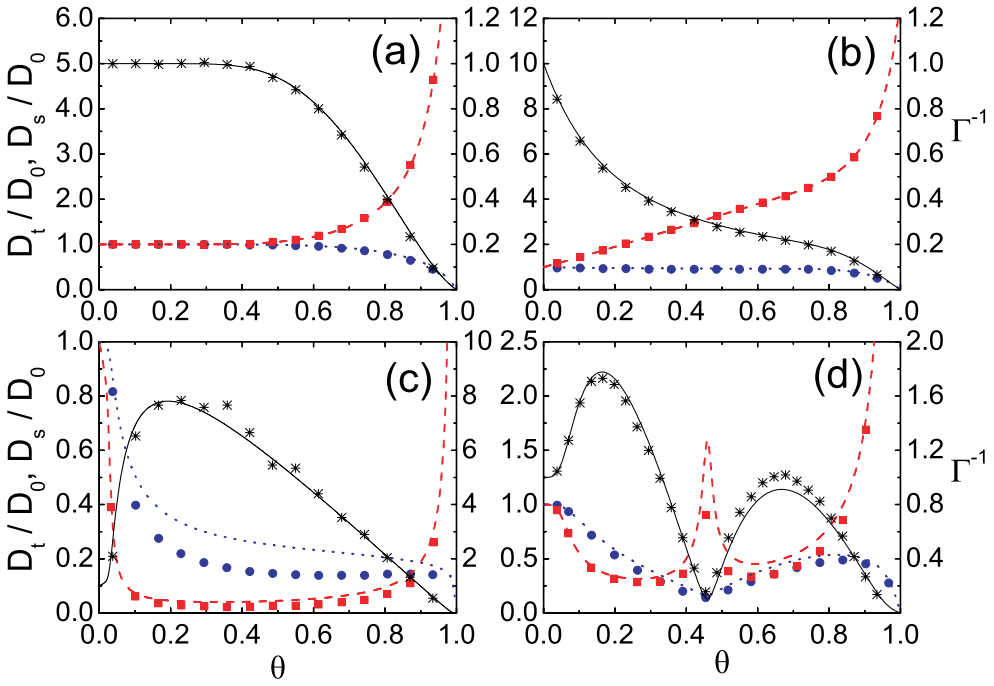

Figure 5.1: D_s/D_0, D_t/D_0 and Γ^{-1} as a function of loading $\theta = \langle n \rangle / n_{\max}$, $n_{\max} = 13$; for (a) $\beta f(n) = 0$, (b) $\beta f(n) = 0.2n^2$, (c) $\beta f(n) = -0.2n^2$ and (d) $\beta f(n)$ that is subsequently concave, convex and again concave, see Table 5.1 and Figure 5.2. The red dashed lines (analytical solution, Eq. (4.7)) and squares (simulations) show the transport diffusion and the blue dotted lines (analytical solution, Eq. (4.10)) and full circles (simulations) the self-diffusion (values on lhs axis). The analytical Γ^{-1} (black full lines, Eq. (2.20)) are compared with the ratio of D_s and D_t (black stars) from the simulations (values on rhs axis).

D_s is measured by a flux of labeled particles j^*. Since the system is in equilibrium there is no concentration gradient. As a result, there is no preferential direction for clustering, and there will be no force counteracting the current of labeled particles.

The ratio of D_s and D_t Eq. (4.11) however ignores correlations. We have therefore performed kinetic Monte Carlo simulations, cf. Section 2.4. Our choice of rates is:

$$k_{nm} = \nu n e^{-\frac{\beta}{2}[f(n-1)+f(m+1)-f(n)-f(m)]}. \tag{5.1}$$

The factor ν determines the time scale. We refer to Section 2.2 for a rationalization of the use of these rates for clustering particles. In the limit of infinite dilution, both D_t and D_s are equal to $\nu\lambda^2 \equiv D_0$. For an ideal gas $f(n) = 0$, $k_{nm} = \nu n$, i.e., the rates satisfy the law of mass action [41]. The simulations presented here are for 15 pairwise connected cavities, with $n_{\max} = 13$. D_s/D_0, D_t/D_0 and Γ^{-1} are plotted in Fig. 5.1 for different types of free energies, as a function of the loading $\theta = \langle n \rangle / n_{\max}$. Both the simulation data and the analytical curves Eqs. (4.7) and (4.10) are shown. The stars in the figures correspond to the ratio between the self-

and transport diffusion obtained from simulations. Since correlations are included in the simulations but absent in the analytical result, the difference of the two curves is a measure of the effect of correlations on the diffusion. Figure 5.1(a) shows the diffusion for noninteracting particles $\beta f(n) = 0$, with confinement (presence of $n_{\max}$). At low and medium loadings the particles are not influenced by the confinement; $\Gamma = 1$ and $D_s = D_t$. At high loading, the confinement comes into play: Γ^{-1} decreases, D_t rises and D_s lowers. The effect of correlations is negligible: the simulation data and analytical results coincide almost perfectly. Figure 5.1(b) shows the diffusion in the case of a convex free energy $\beta f(n) = 0.2n^2$. Γ^{-1} is lower than one, and D_t is always larger than D_s. Correlations have a negligible influence. Fig. 5.1(c) shows the diffusion for a concave free energy $\beta f(n) = -0.2n^2$. As expected, $D_s > D_t$ for low to moderate loading. At moderate and high loading the "convexity effect" of confinement takes over: Γ^{-1} decreases and eventually becomes smaller than one with $D_t > D_s$. This curve should be compared with Figs. $3(a), (c)$ in [28]. Noteworthy is the fact that the transport diffusion shows a minimum when the thermodynamic factor is around its maximum. This feature is in agreement with experimental observations [28, 100, 101] and with MD simulations [102]. It is now easily understood: when Γ^{-1} is at its highest, the tendency to cluster is maximal, therefore the force opposing the current is also at its strongest. Turning to the effect of correlations, we note that they are quite strong: both D_t and D_s are significantly lower than the analytical results. The effect is the largest for self-diffusion. Nevertheless, the ratio of D_t and D_s is still very close to Γ, again in agreement with what is observed in experiments [28] and MD simulations in similar systems [103]. Fig. 5.1(d) shows the diffusion for a free energy that is first concave, then convex and then concave, as given in table 5.1. A plot of this free energy is given in Figure 5.2. From 0 to 6 $f(n)$ is concave, between 5 and 7 it is convex, and between 6 and 13 it is concave ($n_{max} = 13$).

n	0	1	2	3	4	5	6	7	8	9	10	11	12	13
$\beta f(n)$	0	0	0	0	-0.2	-0.6	-4.0	-0.6	-0.2	0	0	0	0	0

Table 5.1: $\beta f(n)$ used in Fig. 5.1(d).

For the first concave part the self-diffusion exceeds the transport diffusion. For the second concave part this is no longer the case, due to the confinement and the influence of the convex part in the middle. This is an illustration of how concavity is necessary but not sufficient for $D_s > D_t$. D_t shows a (local) maximum in the convex part, whereas D_s shows a (local) minimum. Correlations have noticeable effect, and are now more important for D_t than for D_s. Notice that in all cases correlations lower the diffusion coefficients.

5.2 Fit with experimental data

Motivated by the qualitative agreement with experiments, we have tried to reproduce the experimental results from [28] quantitatively. Inspired by the form of the energy function for Lennard-Jones crystals [104], we take $\beta f(n) = an^2 + bn^3$ for $n \leq n_{\max}$, with $n_{\max} = 13$ taken from the experimental data [28]. The parameters a and b are determined by fitting the thermodynamic factor (Eq. (2.20)) with the experimental data, resulting in $\beta f(n) = 0.000642n^2 - 0.0083n^3$. The parameters ν and λ only

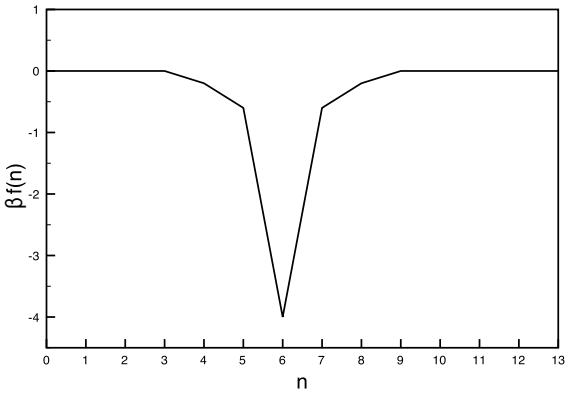

Figure 5.2: $\beta f(n)$ of Table 5.1 and Fig. 5.1(d).

appear in the combination $\nu\lambda^2$, which follows directly from the experimental value of D_t at very low loading. In Fig. 5.3 we compare the obtained simulation results for D_s and D_t with experimental data of methanol in ZIF-8 [28]. Quantitative agreement is found for both D_s and D_t at all values of the loading. This is remarkable since a and b are determined from the equilibrium quantity Γ, and only the experimental value of D_t at very low loading is used in the fit of $\nu\lambda^2$.

A similar quantitative agreement is also found for ethanol in ZIF-8. To find a good free energy function for ethanol, we used a different fitting procedure. Using the analytical results for the thermodynamic factor and the diffusion coefficients as a guide, several free energies where tried until a good resemblance with experiment was found. Since calculation of the analytical results for different free energies requires no computation time, this resemblance can easily be checked "by hand". D_0 is taken slightly higher than the experimental value of D_t for the lowest measured loading ($D_0 = 9.6\ 10^{-13}\ m^2/s$). n_{max} is taken equal to 9. The values of $\beta f(n)$ are given in Table 5.2. The first part of $f(n)$ is constant, after which it becomes (very) concave. The last part is convex. The simulation results and experimental data are given in Figure 5.4. Good agreement is found with experiment, except for the outlier for Γ^{-1} around $\langle n \rangle \approx 1.6$.

n	0	1	2	3	4	5	6	7	8	9
$\beta f(n)$	0	0	0	0	-0.2	-6.8	-13.6	-19.0	-21.0	-21.0

Table 5.2: $\beta f(n)$ used in simulations for ethanol in ZIF-8, Fig. 5.4.

5.3 Dynamical mean-field approximation

In Section 4.1 we obtained analytical expressions for D_s and D_t for a system of length $L = 1$. We now show that the same expressions are obtained in an infinitely long system if one ignores all dynamical correlations. This derivation provides a basis

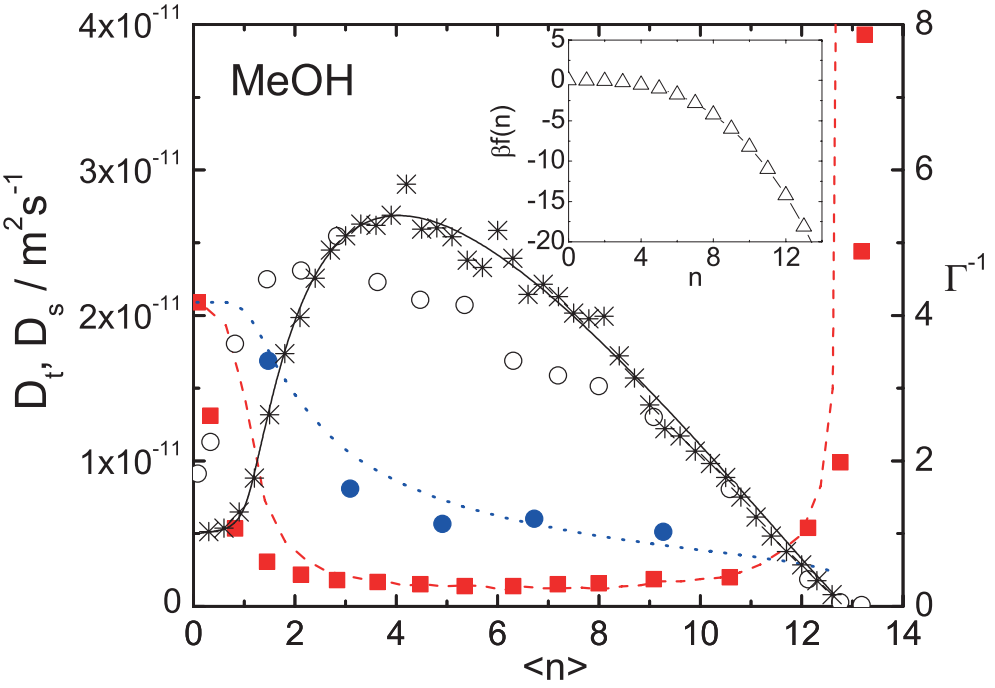

Figure 5.3: Comparison of experimental data of methanol in ZIF-8 [28] with simulations from our model. The experimental self-diffusion and transport diffusion are represented by the blue full circles and red squares, respectively, with the corresponding results from simulations given by the blue dotted line and the red dashed line (values on lhs axis). The experimental (black open circles) and analytical (full black line) Γ^{-1} are compared with the ratio of self- and transport diffusion (black stars) taken from the simulations (values on rhs axis). The inset shows $\beta f(n)$.

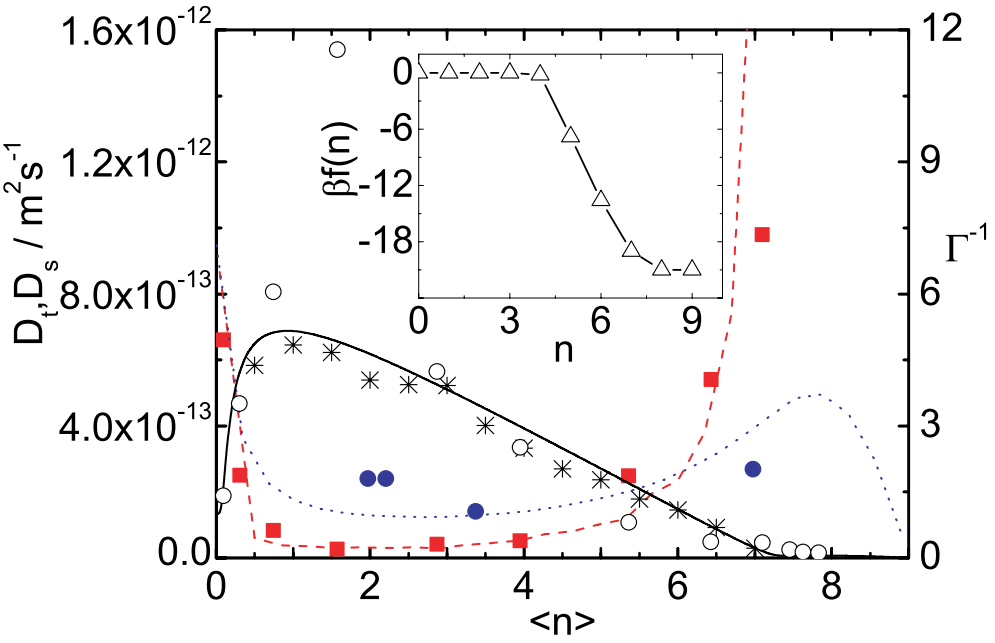

Figure 5.4: Diffusion of ethanol in ZIF-8. The experimental self-diffusion is given by the blue full circles and the results from simulations by the blue dotted line. The experimental transport diffusion is given by the red squares and the results from simulations by the red dashed line (values on lhs axis). The free energy function is shown in the inset. $\beta f(n)$ is represented by the black open triangles, the black line serves as a guide to the eye. The ratio between the self-diffusion and transport diffusion taken from the simulations is given by the black stars. The experimental Γ^{-1} is given by black open circles, the analytical result is given by a full black line (values on rhs axis). Experimental data from [28]

for the understanding of the effect of correlations upon the diffusion, as discussed in Section 5.4.

Consider an infinitely large equilibrium system at chemical potential μ. The lattice is cubic and has dimension d, i.e., each cavity has $2d$ neighbors. We tag one particle at time $t = 0$, and calculate its average MSD in the limit $t \uparrow \infty$. Subsequent jumps of the tagged particle are correlated because of memory effects in the environment (i.e., the other particles), as already explained in Section 2.3. For example, for $n_{\max} = 1$, the tagged particle is more likely to jump back to its previous position, because this cavity is more likely to be empty. The influence of such memory effects is discussed in detail in Section 5.4. In the dynamical mean-field (DMF) approximation all memory effects, or correlations between particle jumps, are neglected [44]. This assumption is equivalent to assuming that, after a jump of the tagged particle, the environment loses its memory instantly. Because the environment is memoryless, the cavities connected to the cavity containing the tagged particle have the equilibrium distribution $p_n^{\rm eq}(\mu)$ at all times. We calculate $\hat{p}_n$, the probability that the cavity containing the tagged particle has n particles in total (including the tagged particle). The tagged particle jumps away from a cavity containing n particles to a cavity containing m particles with rate k_{nm}/n. In the DMF approximation, the master equation for $\hat{p}_n$ reads:

$$\begin{aligned}\dot{\hat{p}}_n = &\sum_{m=1}^{n_{\max}} \hat{p}_m p_{n-1}^{\rm eq} 2d \frac{k_{m,n-1}}{m} - \sum_{m=0}^{n_{\max}-1} \hat{p}_n p_m^{\rm eq} 2d \frac{k_{nm}}{n} \\ &+ \sum_{m=1}^{n_{\max}} \hat{p}_{n-1} p_m^{\rm eq} 2d k_{m,n-1} - \sum_{m=0}^{n_{\max}-1} \hat{p}_n p_m^{\rm eq} 2d k_{nm} \frac{n-1}{n} \\ &+ \sum_{m=0}^{n_{\max}-1} \hat{p}_{n+1} p_m^{\rm eq} 2d k_{n+1,m} \frac{n}{n+1} - \sum_{m=1}^{n_{\max}} \hat{p}_n p_m^{\rm eq} 2d k_{mn}. \end{aligned} \tag{5.2}$$

The positive terms are transitions toward the state $\hat{p}_n$: a jump of the tagged particle to a cavity containing $n-1$ particles (first line), a particle jump to the cavity containing the tagged particle from the state $\hat{p}_{n-1}$ (second line), and a particle jump away from the cavity containing the tagged particle from the state $\hat{p}_{n+1}$ (third line). The negative terms are transitions away from $\hat{p}_n$: a jump of the tagged particle to another cavity (first line), a particle jump away from the cavity containing the tagged particle (second line), and a particle jump to the cavity containing the tagged particle (third line). The stationary solution is

$$\hat{p}_n = \frac{n}{\langle n \rangle} p_n^{\rm eq}(\mu). \tag{5.3}$$

This can be checked by filling in Eq. (5.3) in the master equation and realizing that the two terms on each line cancel each other because of local detailed balance Eq. (2.4). The average jump rate $\hat{k}_{\rm av}$ of the tagged particle is equal to:

$$\hat{k}_{\rm av} = 2d \sum_{n=1}^{n_{\max}} \sum_{m=0}^{n_{\max}-1} \frac{k_{nm}}{n} \hat{p}_n p_m^{\rm eq} \tag{5.4}$$

$$= 2d \sum_{n=1}^{n_{\max}} \sum_{m=0}^{n_{\max}-1} k_{nm} \frac{p_n^{\rm eq}(\mu)}{\langle n \rangle} p_m^{\rm eq} = 2d \frac{\langle k \rangle}{\langle n \rangle}. \tag{5.5}$$

The particle is performing a random walk on a d-dimensional lattice with average jump rate $\hat{k}_{\rm av}$. The self-diffusion is in this case equal to:

$$D_s = \frac{\lambda^2}{2d}\hat{k}_{\rm av} = \frac{\lambda^2\langle k\rangle}{\langle n\rangle}. \tag{5.6}$$

Because all particle jumps are assumed to be uncorrelated, the inter-particle correlation term in Eq. (2.24) is zero and one finds:

$$D_t = \frac{\lambda^2\langle k\rangle}{\langle n^2\rangle - \langle n\rangle^2}. \tag{5.7}$$

As a result, $D_{\rm ms} = D_s$ in the DMF approximation. The self-diffusion Eq. (5.6) and transport diffusion Eq. (5.7) obtained from the DMF approximation are the same as calculated for a system of length $L = 1$, see Section 4.1.

5.4 Diffusion and correlations

We now consider the diffusion for different combinations of rates and interactions. We take $k_{10}e^{-\beta[f(1)-f(0)]} = 1$ for the rates of Eq. (2.12) and $k_{10} = 1$ for the rates of Eq. (2.13). In all cases $kT = \lambda = 1$. We first discuss one-dimensional systems. Diffusion in two- and three-dimensional systems is considered at the end of the section.

Memory effects are studied by measuring directional correlations of subsequent jumps of a single particle, similarly to, e.g., Ref. [105]. We tag one particle and record the direction of its first jump. We measure the probability $\tilde{p}(m)$ that its $m^{\rm th}$ jump has the same direction as its first jump. If the jumps are uncorrelated one has for a one-dimensional system that $\tilde{p}(m) = 1/2$ for all $m \geq 1$. We also measure $p(n|\hat{n})$, the probability that a neighboring cavity has n particles given there are $\hat{n}$ particles in the cavity of the tagged particle. In the DMF approximation one has that $p(n|\hat{n}) = p_n^{\rm eq}$. When we say that correlations increase or decrease the diffusion this is always with reference to the DMF situation. The self-diffusion is influenced by correlations of subsequent jumps of a single particle. By comparing the ratio of the self- and transport diffusion with Γ we have access to interparticle correlations, cf. Eq. (2.24).

For $n_{\rm max} = 1$ our model reduces to the well-known Langmuir gas model [106]. In an infinitely long one-dimensional equilibrium system single-file diffusion occurs [107, 108], resulting in $\langle x(t)\rangle \propto \sqrt{t}$ and $D_s = 0$. In higher-dimensional systems the diffusion is normal. The self-diffusion is lowered because of the *back-correlation mechanism*: If a particle jumps, the cavity it came from is more likely to be empty, making it more likely that the particle jumps back. The transport diffusion is equal to the DMF value for all loadings: $D_t = k_{10} = 1$ [90].

We first discuss the diffusion for $f(n) = 0$. In this case the two rates are the same. Figure 5.5a shows the diffusion for $n_{\rm max} = 2$. Single-particle correlations are caused by the back-correlation mechanism and lower the self-diffusion significantly. This can be seen in Figure 5.6a, where we plot $\tilde{p}(m)$ at loading $\langle n\rangle = 1$. Fig. 5.5a shows that interparticle correlations are positive ($\Gamma^{-1} > D_s/D_t$), signifying that a particle drags along other particles. This can be understood as follows. Suppose a tagged particle has diffused in a certain direction. The vacancies it leaves behind can be occupied

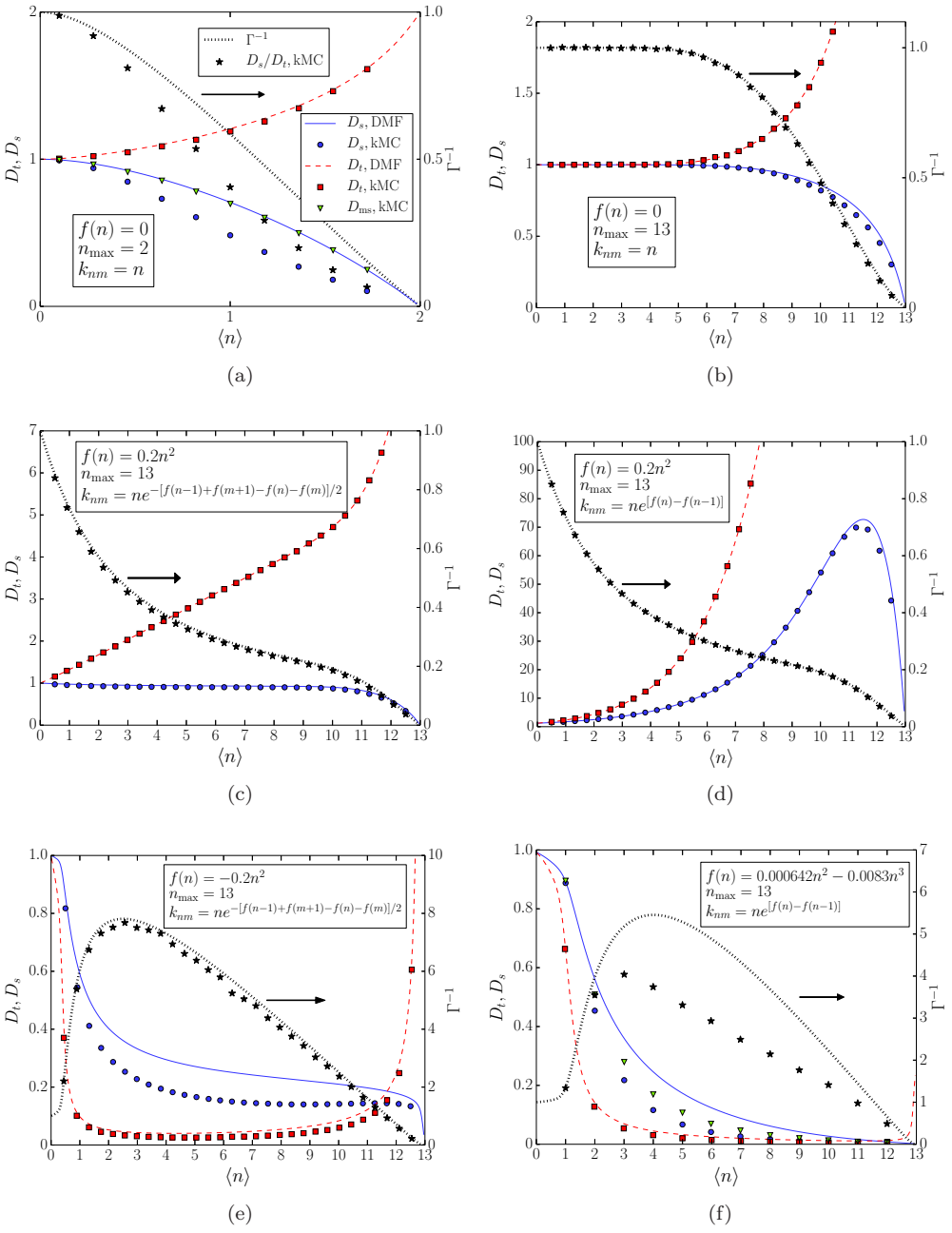

Figure 5.5: D_s, D_t (left axis) and Γ^{-1}, D_s/D_t (right axis). (*a*) $f(n) = 0$ and $n_{\max} = 2$; (*b*) $f(n) = 0$ and $n_{\max} = 13$; (*c*) $f(n) = 0.2n^2$, $n_{\max} = 13$ and the rates of Eq. (2.13) ; (*d*) $f(n) = 0.2n^2$, $n_{\max} = 13$ and the rates of Eq. (2.12); (*e*) $f(n) = -0.2n^2$, $n_{\max} = 13$ and the rates of Eq. (2.13); (*f*) $f(n) = 0.000642n^2 - 0.0083n^3$, $n_{\max} = 13$ and the rates of Eq. (2.12).

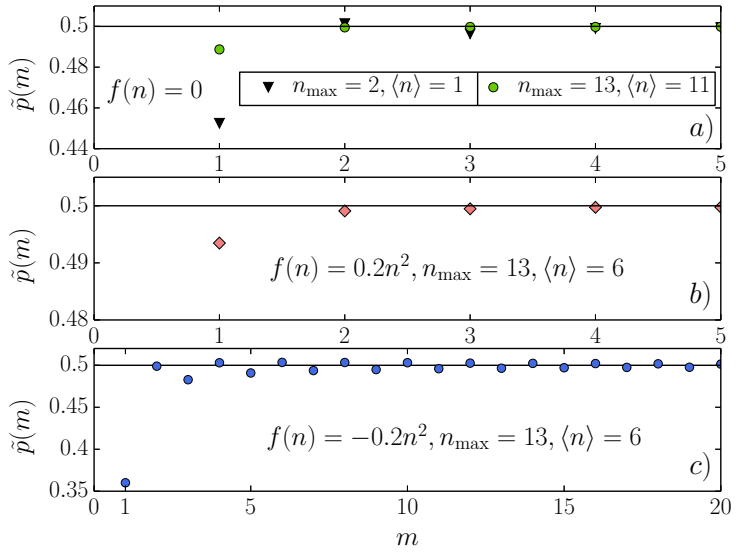

Figure 5.6: Single-particle memory $\tilde{p}(m)$ for different interactions and loadings and the rates of Eq. (2.13).

by other particles. In front the other particles have had to "make way" for the tagged particle. Both effects cause particles in the environment to diffuse in the same direction as the tagged particle. The transport diffusion is almost equal to the DMF value (different from $n_{\max} = 1$, for which it is exactly equal). The Maxwell-Stefan diffusion is higher than the self-diffusion and almost equal to the DMF result.

Figure 5.5b shows the diffusion for $f(n) = 0$ and $n_{\max} = 13$. The diffusive behavior is discussed in Section 5.1. Correlations have a small influence on the self-diffusion, even at high loading. This is because jumps of other particles erase the memory of the environment. The only type of correlations in the system are back-correlations, which occur at loadings where $p^{\text{eq}}_{n_{\max}} \neq 0$. For $n_{\max} = 2$, if the tagged particle jumps from a full cavity, the cavity it jumps to contains at most one other particle. For $n_{\max} = 13$ at loadings $\langle n \rangle \approx n_{\max}$, a particle that jumps from a full cavity will arrive in a cavity containing around 12 other particles. If one of these other particles jumps back, the memory effect of the environment on the tagged particle is lost. The back-correlation effect is therefore smaller compared to the case $n_{\max} = 2$; see $\tilde{p}(m)$ at loading $\langle n \rangle = 11$ in Fig. 5.6a. Similarly to single-particle correlations, interparticle correlations are also small ($\Gamma^{-1} \approx D_s/D_t$). Since the back-correlation mechanism is small, this is what one would expect. In all graphs where $\Gamma^{-1} \approx D_s/D_t$ one has that $D_{\text{ms}} \approx D_s$; we do not plot the MS diffusion for these cases.

We now discuss the diffusion for $f(n) = 0.2n^2$ and $n_{\max} = 13$. Figure 5.5d shows the diffusion for the rates of Eq. (2.12). The self-diffusion shows an increasing trend with increasing concentration and a decrease near $\langle n \rangle \approx n_{\max}$. This is typical behavior observed in MD simulations [46, 109]. Similar behavior is obtained for repulsive particles in other lattice models [47, 62, 64]. For convex $f(n)$'s with the rates of Eq. (2.12) this behavior always occurs, as can be understood as follows. The

difference $[f(n-1)+f_{\mathrm{TS}}]-f(n)$ measures the change in interaction free energy when a particle moves to the TS (f_{TS} is the interaction free energy of a particle in the TS, cf. Appendix A). Since $f(n)$ is convex the difference $f(n)-f(n-1)$ grows with increasing n: It becomes easier to jump to the TS for higher loadings, increasing the diffusion. This interpretation of such behavior is well known [47, 54, 60]. As long as the system does not feel that there is an $n_{\max}$ ($p^{\mathrm{eq}}_{n_{\max}} \approx 0$) the dynamics is a ZRP and the DMF solution is exact; see Section 4.2. When the presence of $n_{\max}$ is felt there are correlations because of the back-correlation mechanism. We can conclude that the rates of Eq. (2.12) provide the correct qualitative behavior for repulsive particles, as observed in MD simulations [46, 47, 109].

Figure 5.5c shows the diffusion for $f(n) = 0.2n^2$, $n_{\max} = 13$, and the rates of Eq. (2.13). A close-up of the self-diffusion is shown in Fig. 5.11. The diffusive behavior is discussed in Section 5.1 and qualitatively differs from Fig 5.5d. It was noted that correlations have a small influence on the diffusion. Because the rates depend on the number of particles in both cavities there are correlations caused by the interaction, besides the back-correlation mechanism. This can be seen by comparing the self-diffusion (Fig. 5.11) with the self-diffusion for $f(n) = 0$ and $n_{\max} = 13$ (Fig. 5.5b). While correlations only have an influence for $f(n) = 0$ if the presence of $n_{\max}$ is felt, correlations are also present at loadings where $n_{\max}$ is not felt for $f(n) = 0.2n^2$. We investigate correlations at loading $\langle n \rangle = 6$. The probability to be full is then negligible [see p^{eq}_n in Fig. 5.7a], and all correlation effects are caused by the interaction. Single-particle correlations due to the interaction can be understood as follows. Consider two cavities containing six particles. If the tagged particle hops, $(6,6) \to (5,7)$, the average number of particles in the cavity it came from is smaller compared the average of p^{eq}_n. Because the free energy favors a homogeneous density distribution, this increases the rate at which the particle jumps back, lowering the self-diffusion compared to the DMF approximation. If the tagged particle makes the jump $(8,4) \to (7,5)$, the rate to jump back is smaller compared to the DMF approximation, thereby enhancing the diffusion. $\tilde{p}(m) \approx 1/2$ for all $m > 1$ and is slightly smaller for $m = 1$; see Fig. 5.6b. Memory effects are small *on average*: The self-diffusion is around 2.6 % lower than the DMF value. $p(n|\hat{n})$ for different $\hat{n}$ and p^{eq}_n are shown in Fig. 5.7a. There is a clear difference between $p(n|\hat{n})$ and p^{eq}_n for $\hat{n} \neq \langle n \rangle$. There are two reasons why the effect of correlations on the diffusion is small. Because there are on average 6 particles per cavity, jumps of other particles tend to erase the memory effect of the environment, as discussed previously. The effect on the diffusion is further diminished because correlations contribute both positively and negatively. They therefore partly cancel each other.

Figure 5.5e shows the diffusion for $f(n) = -0.2n^2$, $n_{\max} = 13$, and the rates of Eq. (2.13). We refer to Section 5.1 for a discussion of the diffusive behavior. There are strong memory effects; see $\tilde{p}(m)$ for $\langle n \rangle = 6$ in Fig. 5.6c. Not only is $\tilde{p}(1)$ much smaller than $1/2$, the memory effect is also long lived. These strong correlations are caused by the clustering of the particles. An example of a strongly correlated event is when the tagged particle jumps from a full to an empty cavity. The probability to jump back is then large; see the difference between p^{eq}_n and $p(12|\hat{n} = 1)$ at $\langle n \rangle = 6$ in Fig. 5.7b. For this event there are no other particles in the cavity where the tagged particle jumps to whose presence could decrease the memory effect. Even though correlations have a strong effect on the self- and transport diffusion, interparticle correlations are small

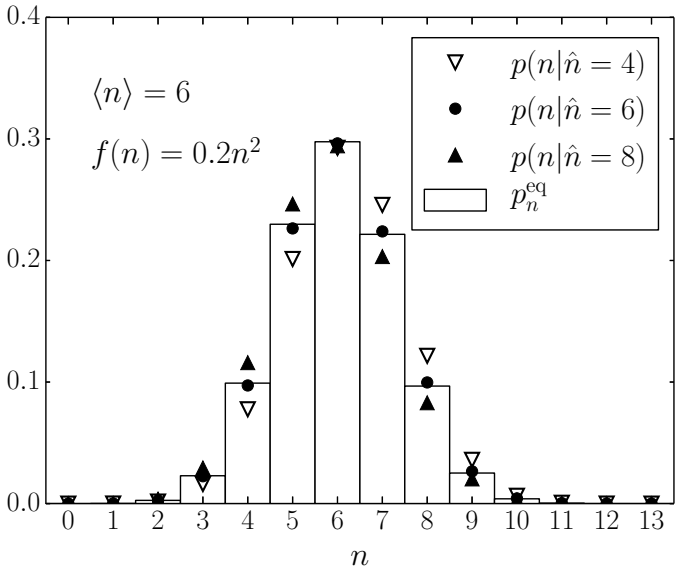

(a)

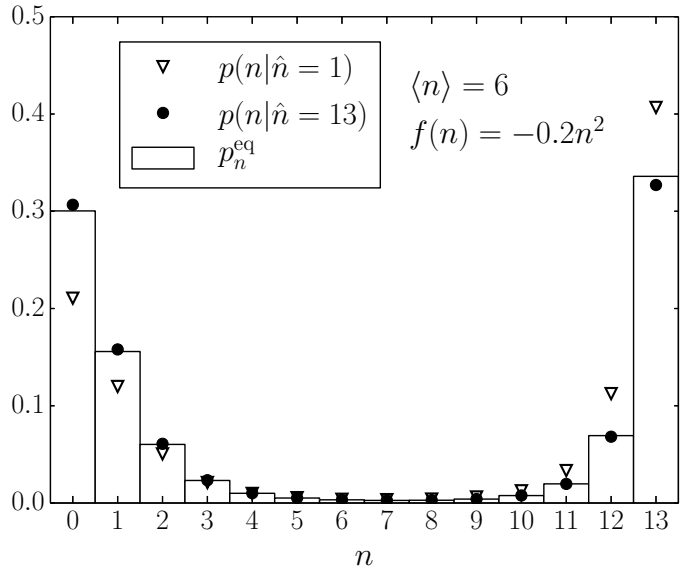

(b)

Figure 5.7: p_n^{eq} and $p(n|\hat{n})$ for different $\hat{n}$ at loading $\langle n \rangle = 6$, $n_{\max} = 13$, and the rates of Eq. (2.13) for (*a*) $f(n) = 0.2n^2$ and (*b*) $f(n) = -0.2n^2$.

($\Gamma^{-1} \approx D_s/D_t$). To understand why particles do not drag along other particles, we examine the dynamics more carefully. For all $n \leq n_{\max}$ one has that $k_{n,n-1} = nk_{10}$, which is the same rate as for $f(n) = 0$. In other words, particle exchange between cavities that are both almost full or both almost empty follows a dynamics similar to the situation for noninteracting particles. In this case, particles do not drag along other particles; see Fig. 5.5b. As can be seen from p_n^{eq} (Figs. 3.1c and 5.7b), this type of transition occurs a lot. The other type of transition that often occurs is a particle jump from a full to an empty cavity. These are strongly correlated events, but they influence only the diffusion of a *single* particle.

We now discuss the diffusion for the concave free energy $f(n) = 0.000642n^2 - 0.0083n^3$ with $n_{\max} = 13$, which was obtained by fitting the analytical Γ from our model with the experimental Γ of methanol in ZIF-8, as discussed in Section 5.2. The experimental Γ is calculated from the experimentally measured adsorption isotherm. However, $f(n)$ does not specify the type of rates that should be used, as discussed in Section 2.2. For the rates of Eq. (2.13) a good agreement with the experimental diffusion data was found; see Fig. 5.3. In contrast, Fig. 5.5f shows the diffusion for the same parameters, with the rates of Eq. (2.12). The diffusive behavior qualitatively differs: both self- and transport diffusion become much smaller for high loadings, and $\Gamma^{-1} > D_s/D_t$. This is in contrast to the experiments where $\Gamma^{-1} \approx D_s/D_t$ [28], which is also reproduced by the rates of Eq. (2.13), cf. Figs. 5.3 and 5.4. We therefore conclude that for clustering particles the rates of Eq. (2.13) give the correct qualitative behavior of the diffusion. This is further supported by the discussion of the calculation of the transition rates in Section 2.2 and Appendix A. Correlations have a strong effect on the diffusion, cf. Fig. 5.5f. Because the rates only depend on the number of particles in the cavity of the tagged particle, these correlations are caused by the back-correlation mechanism. Since the probability to be full is non-negligible even at low loadings, this is not surprising. $\Gamma^{-1} > D_s/D_t$, i.e., interparticle correlations are positive. Since the back-correlation mechanism has a strong impact on the self-diffusion one expects significant inter-particle correlations, as discussed for $f(n) = 0$ and $n_{\max} = 2$. The Maxwell-Stefan diffusion is higher than the self-diffusion but still significantly smaller than the DMF result. Note that because $p_{n_{\max}}^{\text{eq}} \neq 0$ even at low loadings, the dynamics can never be approximated by a ZRP.

Figure 5.8a shows the diffusion for $n_{\max} = 13$, the rates of Eq. (2.13), and the $f(n)$ from Table 5.1. We study this interaction because it switches among concave, convex, and concave. This in contrast to the previous interactions, which are concave, convex, or constant over the whole concentration range. We again refer to Section 5.1 for a discussion of the diffusion. We focus here on the fact that $\Gamma^{-1} < D_s/D_t$ for $6 \leq \langle n \rangle \leq 10$ [see Fig. 5.8b], implying negative interparticle correlations. The grand potential $\Omega(n)$ and p_n^{eq} at loadings $\langle n \rangle = 6$ and $\langle n \rangle = 9$ are plotted in Fig. 5.9. The crucial property to obtain $\Gamma^{-1} < D_s/D_t$ is that the cavity occupation $n = 6$ is very stable, while all other occupations around it are not. Consider a tagged particle that has diffused in a certain direction, in a system at loading $\langle n \rangle = 6$. In this case almost all cavities contain six particles. When the tagged particle jumps to a neighboring cavity, $(6, 6) \to (5, 7)$, it immediately pushes one of the other particles in its new cavity to the cavity it came from to restore the situation where every cavity has six particles. A particle that has diffused in a certain direction therefore pushes other particles in the opposite direction. The interparticle correlation term in Eq. (2.24)

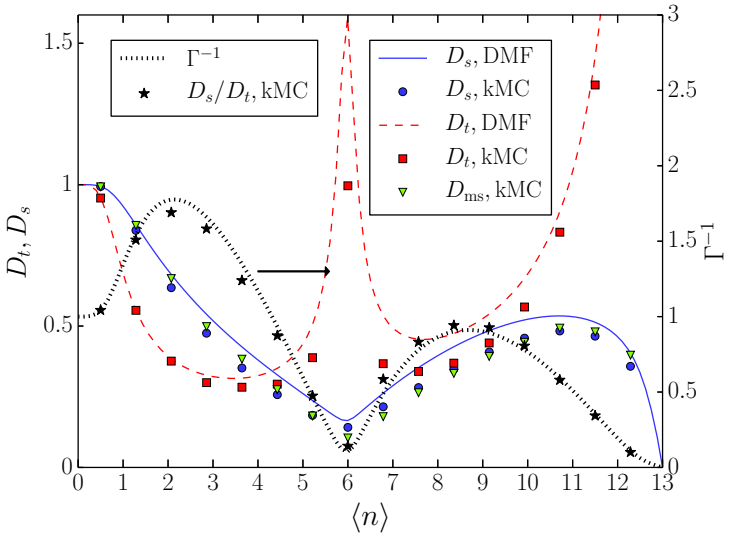

(a)

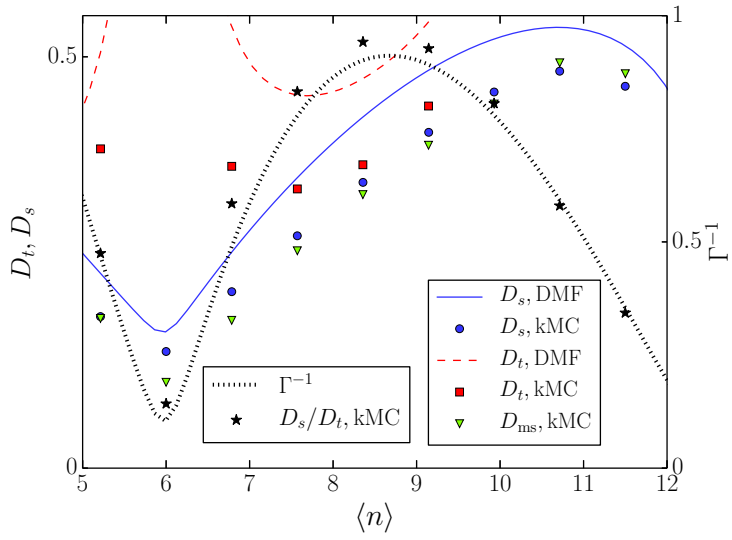

(b)

Figure 5.8: $f(n)$ of Table 5.1, $n_{\max} = 13$, and the rates of Eq. (2.13). (*a*) D_s, D_t (left axis) and Γ^{-1}, D_s/D_t (right axis). (*b*) Close-up of diffusion curves for $5 \leq \langle n \rangle \leq 12$.

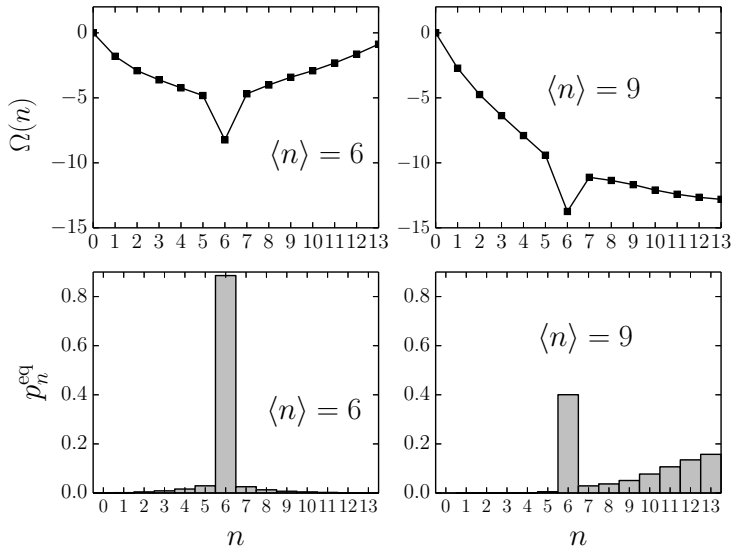

Figure 5.9: $\Omega(n)$ and $p_n^{\rm eq}$ for the $f(n)$ of Table 5.1 with $n_{\max} = 13$, at $\langle n \rangle = 6$ and $\langle n \rangle = 9$.

is then negative and $\Gamma^{-1} < D_s/D_t$. In the theory of Maxwell-Stefan diffusion this means that $1/D_{\rm cor} < 0$ and $D_{\rm ms} < D_s$, as shown in Fig. 5.8b. We are unaware of any previous studies where $D_{\rm ms} < D_s$ was found (or at least explicitly mentioned). Indeed, it is often assumed that the self-diffusion is always higher than the Maxwell-Stefan diffusion [43].

We now discuss the diffusion in two- and three-dimensional systems. The two-dimensional lattice has a square geometry and the three-dimensional lattice is cubic. For these geometries the DMF results Eqs. (5.6) and (5.7) are equal to the one-dimensional case; see Section 5.3. In Fig. 5.10 we plot the self- and transport diffusion for $f(n) = -0.2n^2$, $n_{\max} = 13$, and the rates of Eq. (2.13) in one, two, and three dimensions. The qualitative behavior stays the same. The effect of correlations decreases with increasing dimension, which can be understood as follows. If a tagged particle has jumped, most of the memory of the environment comes from the cavity from which it came. The relative influence of this cavity decreases if there are more cavities connected to the cavity of the tagged particle. One therefore expects the effect of correlations to decrease proportionally to the number of neighbors of each cavity. Also plotted is the diffusion in the x direction in a three-dimensional system, where the rates in the y and z directions are 10 times faster than the rates in the x direction (i.e., there is anisotropy in the dynamics). The effect of correlations is further reduced: If a particle jumps in the x direction, the memory of the environment is erased faster by particles jumping the y and z directions. In Fig. 5.11 we plot the self-diffusion for $f(n) = 0.2n^2$, $n_{\max} = 13$, and the rates of Eq. (2.13) in one, two, and three dimensions. Also here the qualitative behavior stays the same, with the effect of correlations decreasing with higher dimensionality. The effect of correlations on the transport diffusion is already negligible in one dimension, so we do not plot

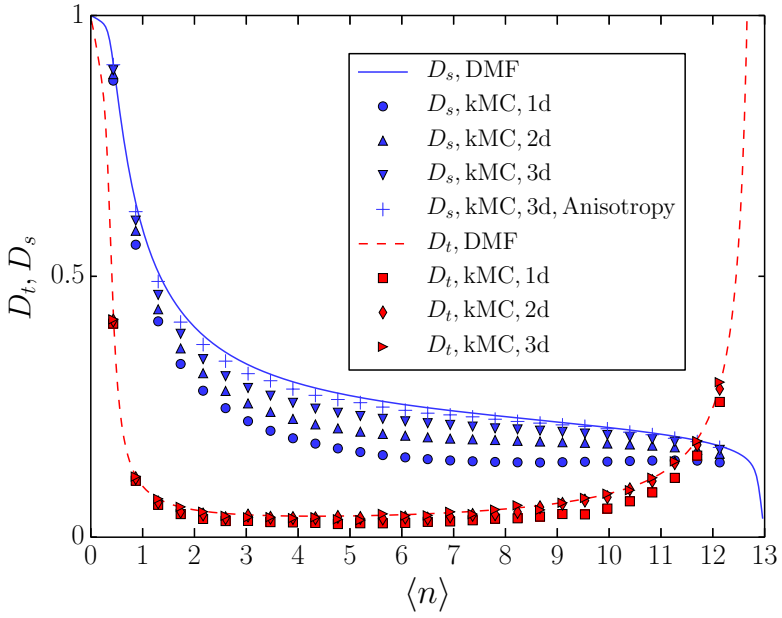

Figure 5.10: D_s and D_t for $f(n) = -0.2n^2$, $n_{\max} = 13$, and the rates of Eq. (2.13) for dimensions 1, 2, and 3.

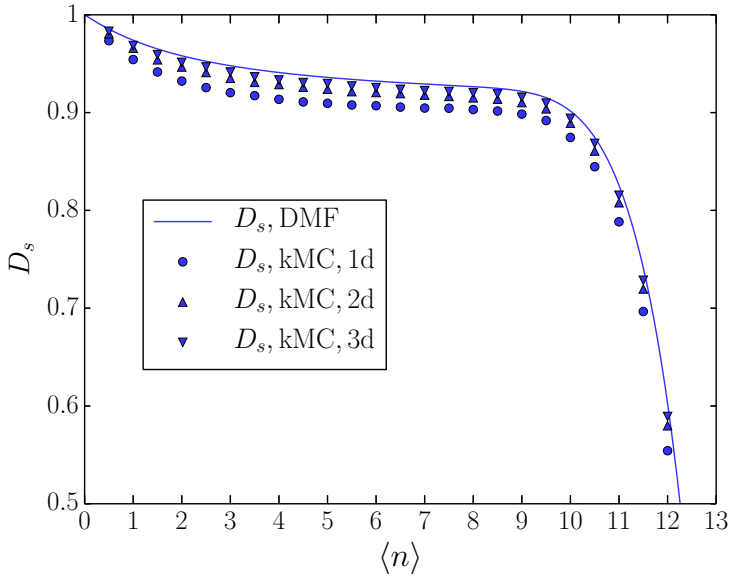

Figure 5.11: Self-diffusion for $f(n) = 0.2n^2$, $n_{\max} = 13$, and the rates of Eq. (2.13) for dimensions 1, 2, and 3.

the data for higher dimensions.

5.5 Correspondence with simulations and experiments

In Section 5.2 quantitative agreement with experimental results of methanol and ethanol diffusion in ZIF-8 was found. In this case the particles undergo strong (attractive) interactions via hydrogen bonding [30]. The behavior of the thermodynamic factor and both the self- and transport diffusion was reproduced correctly over the whole concentration range. This was achieved for an interaction free energy that correctly reproduced the experimentally measured thermodynamic factor. We now examine the assumptions underlying our model and discuss when agreement with experiments and molecular dynamics simulations can be expected.

We assume that particles in neighboring cavities do not interact with each other. The only exception is when a particle is in the transition state, in which case it can interact with particles in both cavities, as discussed in Section 2.2. The same assumption has been made when modeling the behavior of adsorption isotherms; see Section 3.2. A good agreement with experiments can be achieved for apolar molecules at low and medium loadings [86]. For high loadings and polar molecules this assumption is generally not quantitatively correct. The importance of intercavity interactions on equilibrium properties was investigated using simulations in Refs. [59, 110]. It was found that at high loadings this interaction is in general non-negligible. At low temperature intercavity interactions can be important at low loadings, cf. Ref. [110]. In Ref. [60] the average jump rate of a particle between two cavities ($\hat{k}_{\mathrm{av}}$) was calculated numerically using dynamically corrected TST. It was found that if all other cavities (differing from cavities A and B as defined in Section 2.2) connected to the cavity of the particle that jumps are closed off, the calculated self-diffusion can differ by as much as 60 %. From these results it is clear that agreement with experiments can, in general, only be expected for low and medium loadings. The agreement with experiment was found for strongly interacting particles, using the rates of Eq. (2.13). For these rates, the particle in the transition state interacts with the particles in both cavities. Hence, the most important intercavity interaction, when one of the particles is in the transition state, is taken into account in the dynamics.

We did not include a dynamical correction factor in the rates, i.e., we assumed that all particles crossing the TS equilibrate in cavity B (see the discussion in Appendix A). A quantitative influence of the correction factor was found for particles feeling repulsive interactions [46, 60]. This is understandable for repulsive interactions, because particles in cavity B tend to push back the particle that jumps. Agreement was found with experiments of clustering particles, which are attractive. It can be expected that recrossing of the TS on short time scales are of less importance in this case, because a particle that has crossed the TS is attracted by the other particles in cavity B.

Flexibility of the material can have an influence, as was found for ethane diffusion in MOF ZIF-8 [111]. It remains an open question if it is important for ethanol and methanol diffusion. We note that cavity windows whose size depends on the loading, as found in Ref. [111], can be accounted for by making the interaction free energy of

the TS depend on the number of particles: $f_{\mathrm{TS}} = f_{\mathrm{TS}}(n)$.

From the above discussion one can conclude that in general a qualitative agreement can be expected with experimental systems. For the case of clustering particles, our model seems to allow for a quantitative agreement of both dynamical and equilibrium properties over the whole concentration range. Both the free energy $F(n)$ and the rates k_{nm} can be determined numerically using MD simulations [59, 112, 113]. The quality of our assumptions and choice of rates could be verified using these techniques. Such a study would also be of interest to investigate memory effects. Beerdsen, Dubbeldam, and Smit have studied diffusion in microporous materials using dynamically corrected TST [60, 61, 109]. In their work it is assumed that, after the particle has equilibrated in the cavity it has jumped to, memory effects are negligible. Abouelnasr and Smit presented a study where these memory effect are included [112] for a system showing behavior similar to that in Fig. 5.5d. In this case memory effects in the environment can be expected to be negligible, as was found in Ref. [112]. For clustering particles this memory effect is, however, much stronger, especially in a one-dimensional system, cf. Fig. 5.5e.

5.6 Conclusion

We conclude that our model allows for an understanding of the effect of clustering on the self- and transport diffusion. For clustering particles, the behavior of the self- and transport diffusion observed in experiments can be understood over the whole concentration range. Rather surprisingly, also a good quantitative agreement with the experimental results can be obtained. Given the proper choice of transition rates, one finds the diffusive behavior of repulsive particles as observed in MD simulations and other lattice models. The interpretation of this behavior agrees with those given in previous studies.

It is commonly assumed that inter-particle correlations are negligible in cage-type materials connected by narrow windows, i.e., $\Gamma^{-1} \approx D_s/D_t$; see the discussion in [27]. Only at high concentrations one observes significant inter-particle correlations [54]. The results from Chmelik *et al.* [28] provided the first experimental verification that $\Gamma^{-1} \approx D_s/D_t$ by measuring the three terms independently. However, from the discussion in Section 5.4 one can conclude that for clustering particles $\Gamma^{-1} \approx D_s/D_t$ does not follow automatically from the geometry of the material. Indeed, if particles cluster a significant fraction of the cavities are full also at low loadings, and at high loadings the approximation $\Gamma^{-1} \approx D_s/D_t$ fails. The observation that $\Gamma^{-1} \approx D_s/D_t$ is then a non-trivial result of the specific dynamics associated to the clustering particles.

By choosing an "extreme" shape of $f(n)$ one can find negative interparticle correlations. To our knowledge, this is the first observation of this phenomenon in a lattice gas. From the analytical results for $L = 2$ in Section 4.3 one is interested in finding an $f(n)$ for which the net effect of correlations is positive for $L \to \infty$. Given that the effect is very small already for $L = 2$, and that one furthermore has to simulate D_t for several different interactions and concentrations, finding this numerically seems difficult.

Finally, from the discussion in Section 5.5 it is clear that our model can in general not lead to a quantitatively correct description of diffusion in porous materials. Why

it works so well for clustering particles is an interesting question. The techniques to study this with MD simulations are available.

Chapter 6

Adsorption and desorption kinetics

In this Chapter we investigate the adsorption and desorption kinetics of the model. In the adsorption process an empty system is brought into contact with a particle reservoir at a fixed density. Particles flow into the system until the particle concentration in the system is equal to the reservoir density. The desorption process proceeds oppositely: a system at some particle concentration is brought into contact with a reservoir at a lower concentration. Particles then flow out of the system until the particle concentration in the system is equal to the reservoir density. The rates at which particles are absorbed and desorbed from porous materials is of crucial importance for many applications [86]. Particle interactions have a large influence on the adsorption and desorption behavior [114]. The influence of interactions is therefore studied in detail. A one-dimensional system of length 100 is considered. We assume that there is no extra resistance at the boundaries, i.e. there are no surface barriers, which can be the case in experiments [115]. The process is assumed to be isothermal, which is a good approximation for materials of small size. The dynamics is simulated using kinetic Monte Carlo (kMC). Adsorption and desorption runs are performed between 5.10^3 and 3.10^4 times each (depending on the interaction) to achieve good statistics. We again take $k_{10}e^{-\beta[f(1)-f(0)]} = 1$ for the rates of Eq. (2.12) and $k_{10} = 1$ for the rates of Eq. (2.13). In all cases $kT = \lambda = 1$.

6.1 Non-interacting particles

We first consider non-interacting particles $f(n) = 0$ and no $n_{\max}$. Both the rates of Eqs. (2.12) and (2.13) are equal to $k_{nm} = n$, and $p_n^{\text{eq}}(\mu)$ is the Poisson distribution with average $\langle n \rangle$, for which $\langle n^2 \rangle - \langle n \rangle^2 = \langle n \rangle$. Since all particle jumps are uncorrelated D_t is given by Eq. (4.7), which reduces to $\langle k \rangle / (\langle n^2 \rangle - \langle n \rangle^2) = \langle n \rangle / (\langle n^2 \rangle - \langle n \rangle^2) = 1$, cf. Fig. 6.1c. In the desorption process the system is equilibrated according to $p_n^{\text{eq}}(\mu)$ with the chemical potential corresponding to $\langle n \rangle = 13$. Starting at time $t = 0$ the reservoir cavities are put at chemical potential $\mu \to -\infty$ for all times ($p_n^{\text{eq}}(-\infty) = \delta_{n0}$). The adsorption proceeds oppositely: the system starts in a completely empty state,

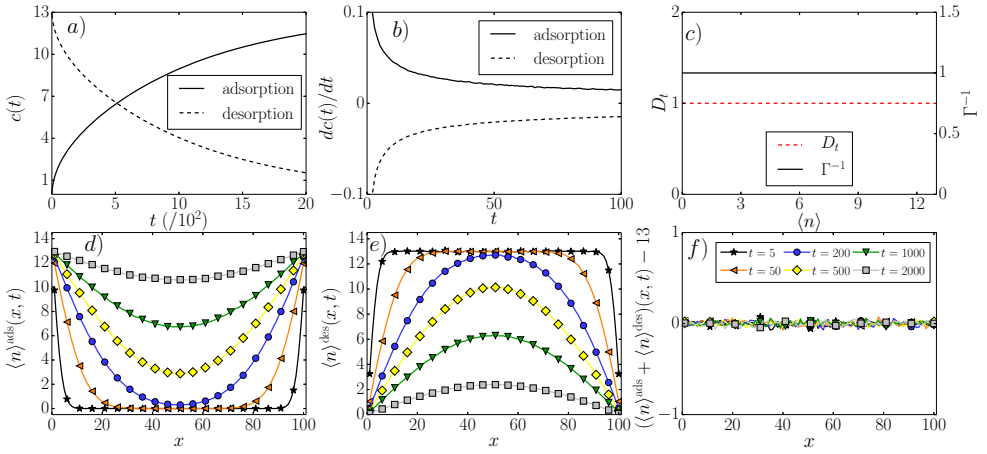

Figure 6.1: Adsorption/desorption between $\langle n \rangle = 13$ and $\langle n \rangle = 0$, for $f(n) = 0$, no $n_{\max}$, and rates $k_n = n$. *a*) Average concentration $c(t)$. *b*) Rate of adsorption and desorption. *c*) Transport diffusion (analytical solution) and Γ^{-1}. *d*), *e*) Average number of particles $\langle n \rangle(x,t)$ in each cavity at different times t, during respectively adsorption $\langle n \rangle^{\rm ads}(x,t)$ and desorption $\langle n \rangle^{\rm des}(x,t)$. For visual clarity markers are shown each 5 positions. The lines are a guide to the eye. *f*) $\langle n \rangle^{\rm ads}(x,t) + \langle n \rangle^{\rm des}(x,t) - 13$. Markers are shown each 10 points. The lines are a guide to the eye.

and the reservoir cavities are put at the chemical potential corresponding to $\langle n \rangle = 13$ at time $t = 0$. The average number of particles in cavity x at time t is denoted by $\langle n \rangle(x,t)$.

In Fig. 6.1 we plot the adsorption and desorption kinetics. The average particle concentration in the system, $c(t) = \sum_{x=1}^{L} \langle n \rangle(x,t)/L$, during adsorption and desorption is shown in Fig. 6.1a. Adsorption and desorption proceed at the same rate, see Fig. 6.1b. The average number of particles in each cavity at different times are plotted in Figs. 6.1c and 6.1d, for respectively adsorption ($\langle n \rangle^{\rm ads}(x,t)$) and desorption ($\langle n \rangle^{\rm des}(x,t)$). In Fig. 6.1f we plot $\langle n \rangle^{\rm ads}(x,t) + \langle n \rangle^{\rm des}(x,t) - 13$. Since adsorption and desorption proceed at the same rate this quantity is zero for all x and t. If adsorption proceeds faster than desorption it is positive, and *vice versa*.

In a continuous system with constant transport diffusion D_t, the concentration dependence $c(x,t) = \langle n \rangle(x,t)$ during desorption can be found by solving the diffusion equation:

$$\frac{\partial c(x,t)}{\partial t} = D_t \frac{\partial^2 c(x,t)}{\partial x^2}, \tag{6.1}$$

with boundary conditions

$$c(0,t) = c(L,t) = 0, \quad \forall t, \tag{6.2}$$

$$c(x,0) = \langle n \rangle_{\rm start}, \quad 0 < x < L. \tag{6.3}$$

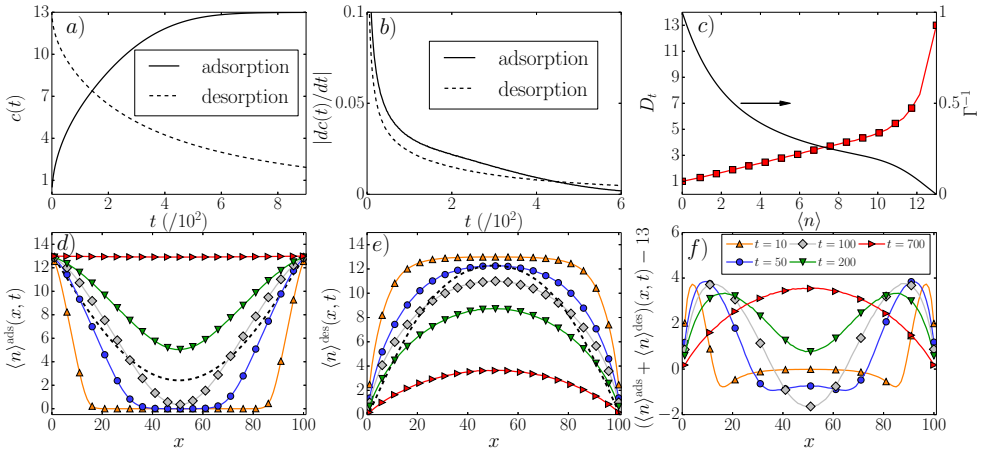

Figure 6.2: Adsorption/desorption between $\langle n \rangle = 13$ and $\langle n \rangle = 0$, for $f(n) = 0.2n^2$, $n_{\max} = 13$, and the rates of Eq. (2.13). *a*) Average concentration $c(t)$. *b*) Rate of adsorption and desorption. *c*) (red squares, left axis) Transport diffusion from kMC, the line is a guide to the eye. D_t at $\langle n \rangle = 0$ and $\langle n \rangle = 13$ was calculated analytically. (black line, right axis) Γ^{-1} *d*), *e*) Average number of particles $\langle n \rangle(x,t)$ in each cavity at different times t, during respectively adsorption $\langle n \rangle^{\rm ads}(x,t)$ and desorption $\langle n \rangle^{\rm des}(x,t)$. Markers are shown each 5 positions. The lines are a guide to the eye. The black dashed lines represent respectively $\langle n \rangle^{\rm ads}(x,t)$ and $\langle n \rangle^{\rm des}(x,t)$ for the parameters of Fig. 6.1, with the same concentration $c(t)$ as for $t = 100$ in this figure. *f*) $\langle n \rangle^{\rm ads}(x,t) + \langle n \rangle^{\rm des}(x,t) - 13$. Markers are shown each 10 points. The lines are a guide to the eye.

The solution is [116]:

$$c^{\rm des}(x,t) = \frac{4\langle n \rangle_{\rm start}}{\pi} \sum_{n=0}^{\infty} \frac{1}{2n+1} \sin\left(\frac{(2n+1)\,\pi x}{L}\right) e^{-D_t[(2n+1)\pi/L]^2 t}. \tag{6.4}$$

The concentration dependence during adsorption is simply $c^{\rm ads}(x,t) = \langle n \rangle_{\rm start} - c^{\rm des}(x,t)$. It was checked that for $L \uparrow \infty$ our simulations converge to this solution.

6.2 Repulsive particles

For interacting particles the transport diffusion is concentration dependent and, as a result, adsorption and desorption proceed at different rates [86, 117, 118]. For a continuous system the concentration dependence can be found by solving the diffusion equation with a concentration-dependent transport diffusion:

$$\frac{\partial c(x,t)}{\partial t} = \frac{\partial}{\partial x}\left(D_t(c(x,t))\frac{\partial c(x,t)}{\partial x}\right), \tag{6.5}$$

with the correct boundary conditions for adsorption/desorption. If the transport diffusion can be calculated analytically, this equation can be solved numerically. If

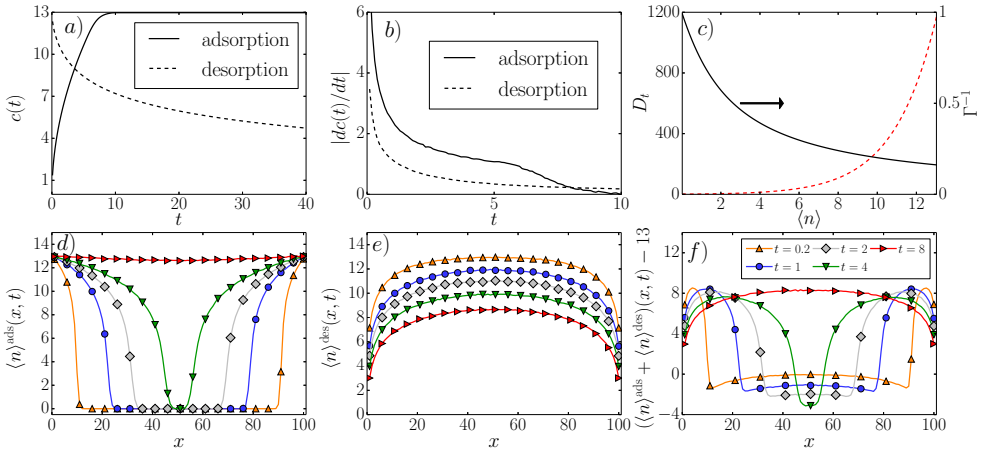

Figure 6.3: Adsorption/desorption between $\langle n \rangle = 13$ and $\langle n \rangle = 0$, for $f(n) = 0.2n^2$, no $n_{\max}$, and the rates of Eq. (2.12). *a*) Average concentration $c(t)$. *b*) Rate of adsorption and desorption. *c*) (dashed line, left axis) Transport diffusion (analytical result). (black line, right axis) Γ^{-1} *d*), *e*) Average number of particles $\langle n \rangle(x,t)$ in each cavity at different times t, during respectively adsorption $\langle n \rangle^{\text{ads}}(x,t)$ and desorption $\langle n \rangle^{\text{des}}(x,t)$. Markers are shown each 5 positions. The lines are a guide to the eye. *f*) $\langle n \rangle^{\text{ads}}(x,t) + \langle n \rangle^{\text{des}}(x,t) - 13$. Markers are shown each 10 points. The lines are a guide to the eye.

not, it is necessary to first perform kMC simulations to measure the transport diffusion at different concentrations. This result can then be interpolated to obtain $D_t(c)$, which can be used to numerically solve Eq. (6.5). Such a procedure is however time consuming, and one has to be careful with the numerical accuracy of the obtained result. Instead, we simulate directly the adsorption and desorption behavior using kMC.

Consider the parameters $f(n) = 0.2n^2$, $n_{\max} = 13$, and the rates of Eq. (2.13), with the adsorption and desorption proceeding between $\langle n \rangle = 0$ and $\langle n \rangle = 13$, cf. Fig. 6.2. The reservoirs are put at $\langle n \rangle = 13$ by taking the chemical potential $\mu \to \infty$ ($p_n^{\text{eq}}(\infty) = \delta_{n n_{\max}}$). The system system starts at $\langle n \rangle = 13$ by taking $n_i = 13$ for $1 < i < L$. As discussed in Chapter 3, the particles are repulsive for this interaction. The transport diffusion therefore increases with concentration, cf. Fig. 6.2c. The rate of adsorption is higher than the rate of desorption, as can be seen from Fig. 6.2b. If the system is almost completely filled in the adsorption process the desorption starts proceeding faster. $\langle n \rangle^{\text{ads}}(x,t)$ and $\langle n \rangle^{\text{des}}(x,t)$ at different times are plotted in respectively Figs. 6.2d and 6.2e. In Fig. 6.2f we plot $\langle n \rangle^{\text{ads}}(x,t) + \langle n \rangle^{\text{des}}(x,t) - 13$. Since the transport diffusion grows with increasing concentration, particles diffuse faster from high to low concentration if the particle concentration is high. During adsorption the reservoirs provide a steady input of particles, which creates a front of high concentration that moves into the system. During desorption the region of high concentration gradually disappears. Adsorption therefore proceeds at a higher rate. The front of high concentration moving into the system during adsorption (Fig. 6.2d)

results in two inward moving peaks in Fig. 6.2f. For small times, the desorption in the middle of the system is faster than the adsorption. The effect is however smaller, and disappears when the middle of the system decreases in concentration. By comparing Figs. 6.1 and 6.2 one sees that adsorption and desorption proceed faster compared to the non-interacting case, as can be expected. The black dashed lines in Figs. 6.2d and 6.2e represent respectively $\langle n \rangle^{\text{ads}}(x,t)$ and $\langle n \rangle^{\text{des}}(x,t)$ for the parameters of Fig. 6.1, with the same average concentration $c(t)$ as for $t = 100$ in Fig. 6.2. During the adsorption of non-interacting particles, a particle diffuses as fast near the boundaries as in the middle. For repulsive particles the diffusion is higher at the boundaries than in the middle of the system. This makes the concentration of repulsive particles higher near the boundaries and lower in the middle, for the same average concentration. During desorption the repulsive particles diffuse faster in the middle of the system, also leading to a concentration that is higher near the boundaries and lower in the middle.

We now consider a ZRP with $f(n) = 0.2n^2$, with the adsorption and desorption proceeding between $\langle n \rangle = 0$ and $\langle n \rangle = 13$, cf. Fig. 6.3. Since the difference in transport diffusion between $\langle n \rangle = 0$ and $\langle n \rangle = 13$ is much higher than in the previous case, the difference between adsorption and desorption is more pronounced. The qualitative behavior stays the same.

6.3 Attractive particles

We now study attractive particles. Consider the parameters $f(n) = 0.000642n^2 - 0.0083n^3$, $n_{\max} = 13$, and the rates of Eq. (2.13). This interaction is qualitatively similar to $f(n) = -0.2n^2$, but is more interesting because it provides a good description of methanol diffusion in ZIF-8, cf. Section 5.2. The transport diffusion has a minimum for low and medium concentrations and a maximum near $\langle n \rangle = 13$, cf. 6.4c. The adsorption and desorption kinetics between $\langle n \rangle = 13$ and $\langle n \rangle = 0$ are shown in Fig. 6.4. Even though the transport diffusion shows a strong minimum for low and medium concentrations, adsorption still proceeds faster than desorption. This is because of the maximum in the transport diffusion around $\langle n \rangle = 13$, resulting in the same qualitative behavior as in Figs. 6.2 and 6.3. Adsorption and desorption proceed slower compared to Figs. 6.1 and 6.2, because of the minimum in the transport diffusion. The black dashed lines in Figs. 6.4d and 6.4e represent respectively $\langle n \rangle^{\text{ads}}(x,t)$ and $\langle n \rangle^{\text{des}}(x,t)$ for the parameters of Fig. 6.1, with the same concentration $c(t)$ as for $t = 4000$ in Fig. 6.4. The difference for adsorption is qualitatively the same as in Fig. 6.2d, although it is more pronounced due to the large difference in the transport diffusion between low and high concentration. For small times the difference in desorption is qualitatively the same as in Fig. 6.2e. For longer times this behavior is reversed compared to Fig. 6.2e. Once the middle of the system is no longer at $\langle n \rangle = 13$, the diffusion near the boundaries (where $\langle n \rangle \approx 0$) is faster than in the middle of the system.

The adsorption and desorption kinetics between $\langle n \rangle = 7$ and $\langle n \rangle = 0$ for the same parameters are shown in Fig. 6.5. In contrast to the previous cases, the transport diffusion at the starting concentration of the adsorption ($\langle n \rangle = 7$) is smaller than at $\langle n \rangle = 0$. The steady flow of particles from the reservoirs now slows down the adsorption compared to the desorption. The behavior in Fig. 6.5f is the reverse of the

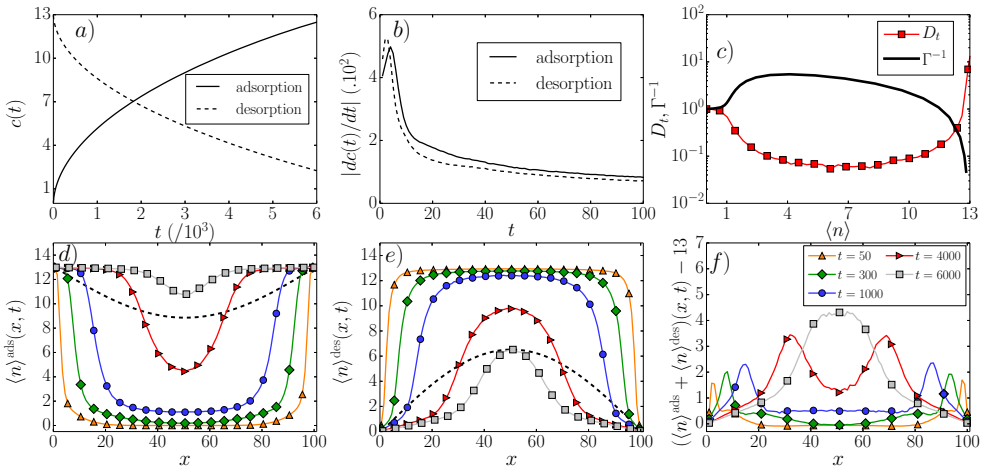

Figure 6.4: Adsorption/desorption between $\langle n \rangle = 13$ and $\langle n \rangle = 0$, for $f(n) = 0.000642n^2 - 0.0083n^3$, $n_{\max} = 13$, and the rates of Eq. (2.13). *a*) Average concentration $c(t)$. *b*) Rate of adsorption and desorption. *c*) (red squares) Transport diffusion from kMC, the line is a guide to the eye. D_t at $\langle n \rangle = 0$ and $\langle n \rangle = 13$ was calculated analytically. (black line) Γ^{-1} *d*), *e*) Average number of particles $\langle n \rangle(x,t)$ in each cavity at different times t, during respectively adsorption $\langle n \rangle^{\rm ads}(x,t)$ and desorption $\langle n \rangle^{\rm des}(x,t)$. Markers are shown each 5 positions. The lines are a guide to the eye. The black dashed lines represent respectively $\langle n \rangle^{\rm ads}(x,t)$ and $\langle n \rangle^{\rm des}(x,t)$ for the parameters of Fig. 6.1, with the same concentration $c(t)$ as for $t = 4000$ in this figure. *f*) $\langle n \rangle^{\rm ads}(x,t) + \langle n \rangle^{\rm des}(x,t) - 13$. Markers are shown each 10 points. The lines are a guide to the eye.

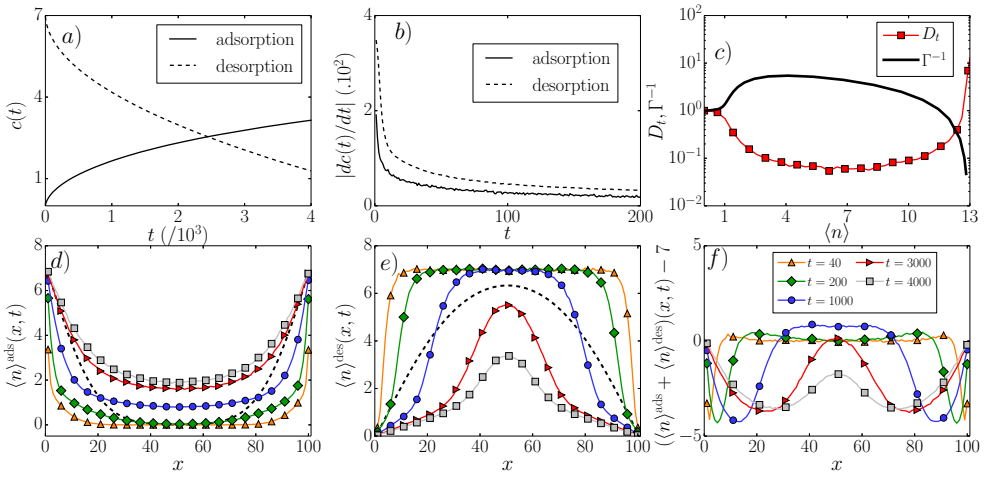

Figure 6.5: Adsorption/desorption between $\langle n\rangle = 7$ and $\langle n\rangle = 0$, for $f(n) = 0.000642n^2 - 0.0083n^3$, $n_{\max} = 13$, and the rates of Eq. (2.13). *a*) Average concentration $c(t)$. *b*) Rate of adsorption and desorption. *c*) (red squares) Transport diffusion from kMC, the line is a guide to the eye. D_t at $\langle n\rangle = 0$ and $\langle n\rangle = 13$ was calculated analytically. (black line) Γ^{-1} *d*), *e*) Average number of particles $\langle n\rangle(x,t)$ in each cavity at different times t, during respectively adsorption $\langle n\rangle^{\text{ads}}(x,t)$ and desorption $\langle n\rangle^{\text{des}}(x,t)$. Markers are shown each 5 positions. The lines are a guide to the eye. The black dashed lines represent respectively $\langle n\rangle^{\text{ads}}(x,t)$ and $\langle n\rangle^{\text{des}}(x,t)$ for non-interacting particles between $\langle n\rangle = 7$ and $\langle n\rangle = 0$, with the same concentration $c(t)$ as for $t = 1000$ in this figure. *f*) $\langle n\rangle^{\text{ads}}(x,t) + \langle n\rangle^{\text{des}}(x,t) - 7$. Markers are shown each 10 points. The lines are a guide to the eye.

previous cases. The black dashed lines in Figs. 6.5d and 6.5e represent respectively $\langle n \rangle^{\text{ads}}(x,t)$ and $\langle n \rangle^{\text{des}}(x,t)$ for non-interacting particles between $\langle n \rangle = 7$ and $\langle n \rangle = 0$, with the same concentration $c(t)$ as for $t = 1000$ in Fig. 6.5. The difference in adsorption is reversed compared to Fig. 6.2d: the concentration at the boundaries is here lower than for the non-interacting case. The difference in desorption is the same as for Fig. 6.4e at long times.

For attractive particles with the rates of Eq. (2.12) and $n_{\max} = \infty$ there is particle condensation, as mentioned in Section 4.2. We therefore don't study this situation.

6.4 Conclusion

To conclude, we studied the adsorption and desorption kinetics for different interactions. In the adsorption process the system is initialized at concentration c_{low}. At time $t = 0$ the system is connected to particle reservoirs at higher concentration c_{high}, after which equilibration to c_{high} occurs. The desorption process proceeds reversely: the system is initialized at c_{high}, and the reservoirs are fixed at concentration c_{low}. Both adsorption and desorption processes are strongly influenced by the concentration-dependent transport diffusion. For repulsive particles the transport diffusion is a monotonic increasing function of concentration. In this case adsorption is always faster than desorption. For attractive particles the transport diffusion is nonmonotonic. Around $\langle n \rangle \approx 0$ it decreases for increasing concentration, has a minimum at an intermediate concentration and increases up to its maximal value at $\langle n \rangle = n_{\max}$. In this situation both adsorption or desorption can proceed faster than the other, depending on the choice of c_{high} and c_{low}.

Chapter 7

Current fluctuations

7.1 Introduction

A system connected to two particle reservoirs at different densities relaxes to a nonequilibrium steady state (NSS), with a particle current flowing through it. The description of the fluctuations of this current has recently received much attention [119–133]. In equilibrium, thermodynamic potentials are related to exponentially unlikely fluctuations away from the average [134], as was already discussed by Einstein [135]. Analogously, one can construct nonequilibrium thermodynamic potentials from the study of exponentially unlikely current and density fluctuations away from the NSS [136]. A theoretical framework for this approach is provided by the macroscopic fluctuation theory (MFT) [137–141].

Using the MFT, Akkermans and co-workers studied current fluctuations in diffusive systems connected to two reservoirs [142]. They showed analytically that for a system of arbitrary (but fixed) dimension, the ratio of the cumulants of the current distribution is independent of the shape of the system and the shape of the contacts with the reservoirs. This derivation is valid if both the system and the contacts with the reservoirs are macroscopic in size. The analytical prediction was tested by numerically calculating the ratio of the first two cumulants, called the Fano factor, for the symmetric simple exclusion process (SSEP). In two dimensions, convergence to the analytical predictions was found for large system sizes by assuming a power-law behavior and extrapolating the numerical data. In three dimensions no convergence was found. The numerical results were, however, obtained for contacts that are not macroscopic in size. Akkermans et al. therefore argued that the discrepancy between numerics and theory was caused by too small contact sizes with the reservoirs.

Under certain conditions, the asymptotic current distribution of a one-dimensional system that is described by the MFT can be calculated from an additivity principle (AP) postulated by Bodineau and Derrida [39]. The validity of this AP has been confirmed in several one-dimensional systems, both analytically [39, 143–146] and numerically [120, 146–149]. An interesting question is if one can use the AP to predict the current distribution in higher-dimensional systems. This is especially important because many experimental systems are higher-dimensional. The results from [142] indicate that it is, indeed, possible to do this. So far, only a few studies have

addressed this question. Saito and Dhar studied heat fluctuations in a deterministic system connected to stochastic reservoirs [150]. They found that the AP can predict the current distribution in three dimensions, both for diffusive and anomalous heat transport. Hurtado, Pérez-Espigares, del Pozo, and Garrido confirmed the validity of the AP for the two-dimensional Kipnis-Marchioro-Presutti (KMP) model [120, 151].

We study numerically the first three cumulants of the current distribution of boundary driven generalized exclusion processes (GEPs) [75]. The dynamics is simulated using kinetic Monte Carlo (kMC). The simplest case of a GEP is the SSEP, where only one particle can occupy each lattice site. In our simulations of the SSEP we consider contacts with the reservoirs that are macroscopic in size. Complete convergence of the Fano factor to the analytical prediction of [142] is found in two dimensions. For three dimensions the data indicate convergence for large system sizes. We proceed with the study of the transport-diffusion coefficient and the current fluctuations in a GEP where maximally two (interacting) particles can occupy each lattice site. The first three cumulants of the current distribution are calculated by combining the AP with the results from [142]. In one and two dimensions the first three cumulants obtained from kMC are in agreement with the predicted values. In three dimensions the first two cumulants are in agreement with the AP. The statistics for the third cumulant is insufficient for a reliable comparison. Because the transport diffusion depends on the dimension, the current statistics change for different dimensions. The current statistics are independent of the spatial dimension for the SSEP and the zero-range process.

7.2 Theory

Consider a one-dimensional system of length L in contact with two particle reservoirs, called A and B, at densities ρ_A and ρ_B. The dynamics in the bulk of the system is diffusive, i.e., there is no external driving in the bulk. The total number of particles that have passed through the system in the time interval $[0, t]$, in the NSS, is denoted by Q_t. To measure Q_t one could, e.g., count the net number of particles entering the system from reservoir A. Q_t is a stochastic quantity and is described by a probability distribution $P(Q_t)$. We study $P(Q_t)$ in the limit $t \uparrow \infty$ and $L \uparrow \infty$. Bodineau and Derrida showed that, by postulating an AP, one can calculate the cumulants of $P(Q_t)$ in a one-dimensional system from the integrals I_m [39, 143]

$$I_m = \int_{\rho_B}^{\rho_A} D_t(\rho)\sigma(\rho)^{m-1} d\rho. \tag{7.1}$$

$D_t(\rho)$ is the transport diffusion Eq. (2.16). $\sigma(\rho)$ describes equilibrium fluctuations of Q_t for large t

$$\frac{\langle Q_t^2 \rangle}{t} = \frac{1}{L}\sigma(\rho), \quad \rho_A = \rho_B = \rho. \tag{7.2}$$

The first three cumulants of $P(Q_t)$ are equal to

$$\frac{\langle Q_t \rangle}{t} = \frac{1}{L} I_1, \tag{7.3}$$

$$\frac{\langle Q_t^2 \rangle_c}{t} = \frac{\langle Q_t^2 \rangle - \langle Q_t \rangle^2}{t} = \frac{1}{L} \frac{I_2}{I_1}, \tag{7.4}$$

$$\frac{\langle Q_t^3 \rangle_c}{t} = \frac{\langle (Q_t - \langle Q_t \rangle)^3 \rangle}{t} = \frac{1}{L} \frac{3(I_3 I_1 - I_2^2)}{I_1^3}. \tag{7.5}$$

The ratio of the first two cumulants is called the Fano factor

$$F = \lim_{L \to \infty} \lim_{t \to \infty} \frac{\langle Q_t^2 \rangle - \langle Q_t \rangle^2}{\langle Q_t \rangle} = \frac{I_2}{I_1^2}. \tag{7.6}$$

Consider all density profiles $\rho_j(x, t')$, with $0 \leq x \leq L$ and $0 \leq t' \leq t$, that lead to the same particle flux j. In the long-time limit $t \uparrow \infty$, only the most probable (optimal) of these profiles is relevant for the current distribution [141]. The AP is valid as long as the optimal profiles are time-independent: $\rho_j(x, t') \equiv \rho_j(x)$. The point at which the optimal profile becomes time-dependent corresponds to a dynamical phase transition [140, 152–154]. For example, for one-dimensional systems on a ring, large fluxes are created by traveling waves [152–154]. One can show from the MFT that a sufficient condition on $D_t(\rho)$ and $\sigma(\rho)$ for the validity of the AP is [140]

$$D_t(\rho)\sigma''(\rho) \leq D_t'(\rho)\sigma'(\rho), \quad \forall \rho. \tag{7.7}$$

Note that (7.7) is a sufficient but not a necessary condition.

A qualitative explanation of the AP goes as follows. The system is divided into subsystems. Their density profiles are considered to be independent of each other, except at the contacts between them. The subsystems should be so small that they are close to (local) equilibrium, but yet be large enough to allow for coarse graining. In this case, each subsystem has Gaussian current fluctuations around its deterministic behavior (2.16), which is completely described by $D_t(\rho)$ and $\sigma(\rho)$. By calculating the optimal densities at the contacts between the subsystems, one finds the cumulant generating function (CGF) of the current distribution. From this CGF one can calculate (7.3), (7.4), (7.5). Hence, the AP allows one to calculate the current distribution arbitrarily far from equilibrium using only the equilibrium quantities $D_t(\rho)$ and $\sigma(\rho)$.

We now consider systems in $d \geq 1$ dimensions. Fick's first law is then given by

$$\vec{j} = -\mathbf{D}_t(\rho)\vec{\nabla}\rho, \tag{7.8}$$

with $\mathbf{D}_t(\rho)$ a symmetric $d \times d$ matrix. If the diffusion is isotropic, which is the case considered here, one can write $\mathbf{D}_t(\rho) = D_{t,d}(\rho)\mathbb{I}_d$, with $D_{t,d}(\rho)$ a scalar function depending on the dimension. A sufficient condition that excludes the possibility of a dynamical phase transition is (7.7) with the scalar functions $D_{t,d}(\rho)$ and $\sigma_d(\rho)$ [140].

Akkermans et al. studied current fluctuations in higher-dimensional diffusive systems [142]. The shape of the system and the contacts with the reservoirs are taken arbitrary, but macroscopic in size. If the optimal density and current profiles are time-independent, the MFT predicts that the CGF of the system in d dimensions $\mu_d(\lambda)$ equals [142]

$$\mu_d(\lambda) = \kappa \mu_1(\lambda), \tag{7.9}$$

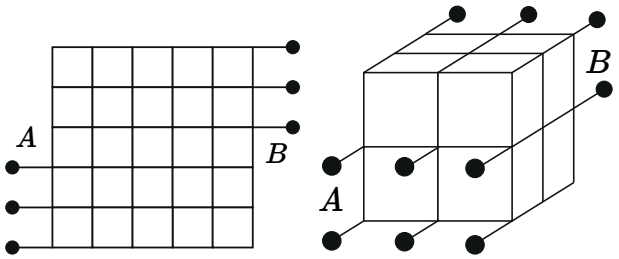

Figure 7.1: The type of contacts used for the SSEP in two dimensions (a) and in three dimensions (b). The black dots are sites with a particle density of 1 (A) or 0 (B), whose state is uncorrelated from the rest of the system. In two dimensions, 1/2 of the lower left is connected to reservoir A and 1/2 of the upper right is connected to reservoir B. In three dimensions, 2/3 of the lower left is connected to reservoir A and 2/3 of the upper right is connected to reservoir B.

with κ a constant that depends on the shape of the system and shape of the contacts with the reservoirs. The calculation of κ is explained in Appendix F.4. $\mu_1(\lambda)$ is the CGF of a one-dimensional system described by $D_{t,d}(\rho)$ and $\sigma_d(\rho)$. Since one assumes that the optimal density and current profiles are time-independent, $\mu_1(\lambda)$ can be calculated from the AP, by using $D_{t,d}(\rho)$ and $\sigma_d(\rho)$ in (7.1).

7.3 Symmetric simple exclusion process

The SSEP is a stochastic lattice gas where particles interact by exclusion, i.e., each site can contain maximally one particle. Each particle attempts to hop to its nearest neighbors with unit rate. A hopping attempt is successful if the site is empty. The distance between two sites is equal to one. For the SSEP $D_t(\rho) = 1$ and $\sigma(\rho) = 2\rho(1-\rho)$ in any dimension. (7.7) is therefore always satisfied. We consider reservoirs with densities $\rho_A = 1$ and $\rho_B = 0$. A calculation from the AP [39] or an exact microscopic derivation [155] shows that $F = 1/3$ in one dimension. Since $D_t(\rho)$ and $\sigma(\rho)$ are independent of the dimension, $F = 1/3$ in any dimension. It is, however, important that the size of the contacts scales with the system size, thereby maintaining a finite fraction of the boundary in contact with the reservoirs. The numerical computation of the Fano factor in [142] was performed for systems where this scaling is absent. We present simulations in which the contacts do scale with the system size.

The dynamics is simulated using a kMC algorithm, cf. Appendix F.1. How the Fano factor is computed from the simulation data is explained in Appendix F.2. In two dimensions we consider squares of size $L \times L$ and in three dimensions cubes of size $L \times L \times L$. The contact between the system and the reservoirs is modeled as lattice sites whose densities are fixed and uncorrelated from the rest of the system, as in [142]. The shape of the contacts is illustrated in Figure 7.1.

The numerical results for the Fano factor are presented in Figure 7.2a. For two dimensions the Fano factor has converged to 1/3 at $L \approx 40$. This extends the extrap-

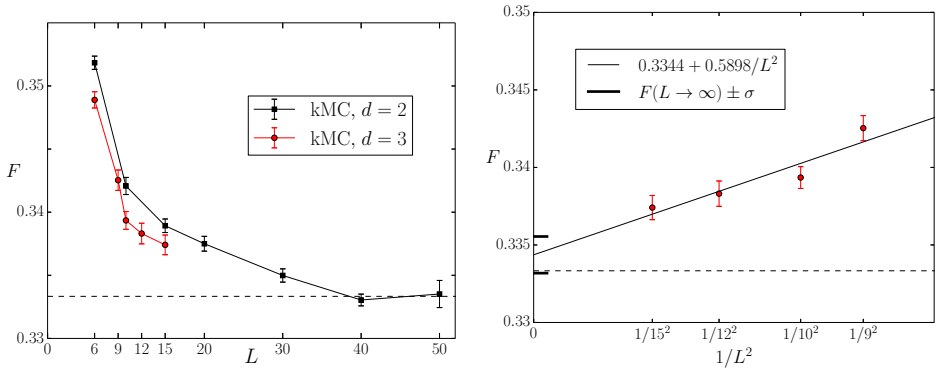

(a) (b)

Figure 7.2: (a) The Fano factor with one-sigma error bars for the SSEP, for squares $L \times L$ and cubes $L \times L \times L$ as depicted in Figure 7.1. The lines are a guide to the eye. The two-dimensional results show a convergence to $1/3$ at $L \approx 40$. The three-dimensional results have not yet converged. (*b*) The three-dimensional data as a function of $1/L^2$ for $L \geq 9$. The thin black line is a $1/L^2$ fit using the method of least squares with weighted error bars. The thick black lines are one-sigma error bars on the $L \to \infty$ limit predicted by the fit.

olation presented in Figure 3 of [142]. We determined numerically that $\kappa \approx 0.663L$ for the geometry in Figure 7.2a, cf. Appendix F.4. The average current indeed converges to $L\langle Q_t \rangle / t \approx 0.663L$, compared to $L\langle Q_t \rangle / t = 1$ in one dimension (data not shown). For three dimensions convergence to $1/3$ is not yet attained at $L = 15$. However, the data indicate convergence to $1/3$ for larger system sizes. For the same distance L between the two reservoirs, the Fano factor in three dimensions is lower than in two dimensions. One therefore expects convergence before $L = 40$ in three dimensions. In Figure 7.2b we plot the Fano factor in three dimensions as a function of $1/L^2$. There is no specific reason to assume that this is the correct convergence law. We choose this scaling because we want to compare our results with Figure 4 of [142]. A $1/L^2$ fit indicates an $L \to \infty$ limit of $F = 0.3344$, with one-sigma error bar $\sigma = 0.0018$. The fit was performed using the method of least squares with weighted error bars [156]. The extrapolation is in agreement with the expected value of $F = 1/3$. Our numerical results validate the conjecture from [142] that the observed discrepancy between numerics and theory is caused by too small contacts with the reservoirs.

7.4 Generalized exclusion processes

7.4.1 The model

We now study the model defined in Section 2.1. The length of the system is equal to $L = N + 1$, with N the number of cavities. This model is a GEP [75] with a stochastic thermodynamical interpretation for the equilibrium statistics and dynamics. In the

following, we fix the parameters to $n_{\max} = 2$ and $\beta = 1$. The rates we consider are

$$k_{nm} = ne^{-[f(n-1)+f(m+1)-f(n)-f(m)]/2}. \tag{7.10}$$

It is clear that a linear term in $F(n)$ (or $f(n)$) does not influence these rates. Hence, we can rescale $F(n)$ so that $f(0) = f(1) \equiv 0$ without loss of generality. All possible interactions are then described by $f(2)$.

For an isothermal system, which we consider here, $D_t(\rho)$ and $\sigma(\rho)$ are related by the following fluctuation-dissipation relation [160]

$$\sigma(\rho) = 2k_bT\rho^2\kappa(\rho)D_t(\rho), \tag{7.11}$$

with $\kappa(\rho)$ the isothermal compressibility. One knows from statistical physics that $\kappa(\rho)$ can be written as

$$\kappa(\rho) = \beta\frac{V}{\langle n\rangle}\frac{\langle n^2\rangle - \langle n\rangle^2}{\langle n\rangle}, \tag{7.12}$$

with V the volume in which the average $\langle n\rangle$ and particle fluctuations $\langle n^2\rangle - \langle n\rangle^2$ are measured. Because particles in different cavities do not interact, one can take the averages over one cavity, $V = 1$ and $\rho = \langle n\rangle$. One then finds for $\sigma(\rho)$ (7.11)

$$\sigma(\rho) = 2(\langle n^2\rangle - \langle n\rangle^2)D_t(\rho). \tag{7.13}$$

Regarding notation, since $\rho = \langle n\rangle$ we use ρ and $\langle n\rangle$ interchangeably. Also, averages $\langle\cdot\rangle$ are a function of the chemical potential of the reservoirs. These can, however, be straightforwardly converted to densities via (2.3). In this chapter we write everything as a function of the density.

From (7.13) one finds that I_m (7.1) can be written as

$$I_m = \int_{\langle n\rangle_B}^{\langle n\rangle_A} D_t(\langle n\rangle)^m \left[2(\langle n^2\rangle - \langle n\rangle^2)\right]^{m-1} d\langle n\rangle, \tag{7.14}$$

where $\langle n\rangle_A$ and $\langle n\rangle_B$ are the average number of particles in, respectively, reservoir cavity A and B. One can compute I_m by numerically simulating $D_t(\langle n\rangle)$ and analytically calculating $\langle n^2\rangle - \langle n\rangle^2$ from $p_n^{\text{eq}}(\mu)$.

7.4.2 Transport-diffusion coefficient

From Section 5.4 one can conclude that $D_t(\rho)$ is, in general, influenced by correlations (see also [161]). Since the effect of correlations changes and is actually seen to diminish with increasing dimension, cf. Section 5.4, the function $D_t(\rho)$ depends on the dimension. If the effect of correlations upon the diffusion is completely neglected one can show that $D_t(\rho)$ is given by (4.7). This result is valid for a (hyper)cubic lattice in any dimension. Because one arrives at (4.7) by neglecting all correlations, it could be argued that in the limit of infinite dimension $D_t(\rho)$ converges to (4.7). Although we do not have a rigorous proof of this statement, it is confirmed by numerical evidence given below (see also Section 5.4). We therefore denote the results that are calculated from (4.7) as the $d \to \infty$ limit. Note that in this limit the integral (7.14) can be calculated analytically.

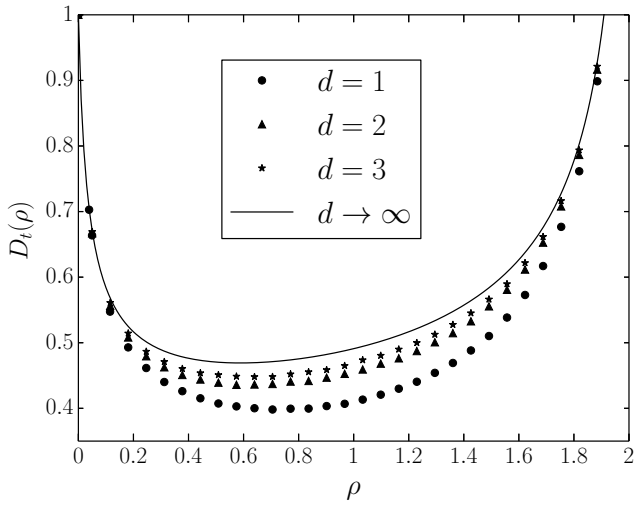

Figure 7.3: $D_t(\rho)$ for $f(2) = -2.5$ and $n_{\max} = 2$ in one, two, three, and infinite dimensions. The error bars are smaller than the symbol sizes.

The uncorrelated result (4.7) is exact for the SSEP ($n_{\max} = 1$), which is easily checked by using that $p_1^{\text{eq}} = \rho$ and $p_0^{\text{eq}} = 1 - \rho$. It is also the same in any dimension [162]. (4.7) is also exact for the one-dimensional ZRP [159], as discussed in Section 4.2. Since the particle distribution in the NSS factorizes in any dimension for the ZRP [163], the calculation from Section 4.2 can be straightforwardly extended to higher dimensions to show that $D_t(\rho)$ is independent of the dimension. To our knowledge, these are the only two cases where the uncorrelated result is exact for GEPs. It is, then, no surprise that $D_t(\rho)$ is independent of the dimension.

We consider now $f(2) = -2.5$. This is a concave $f(n)$, signifying attractive particles. We choose this interaction because correlations have a large effect for attractive particles. In Figure 7.3 we plot $D_t(\rho)$ in one, two, three, and infinite dimensions. We refer to Appendix F.3 for details on the simulations. $D_t(\rho)$ appears to converge with increasing dimension towards the $d \to \infty$ result (4.7). The transport diffusion in function of the dimension for $\langle n \rangle \approx 0.51$ and $\langle n \rangle \approx 1.49$ is shown in, respectively, Figures 7.4a and 7.4b. The behavior is well approximated by a $1/d$ dependence. Figure 7.4c shows the same quantity for the interaction $f(2) = 0$ at $\langle n \rangle = 1$. Also here an approximate $1/d$ dependence is found. This dependence can be understood as follows. Correlations are the result of memory effects in the environment, as discussed in Section 5.4. The strongest contribution comes from the increased probability that a particle jumps back to its previous position. The probability to do so is approximately $1/2d$ as there are $2d$ neighboring cavities. This simple argument indeed suggests that the effect of correlations will decrease approximately as $\propto 1/d$.

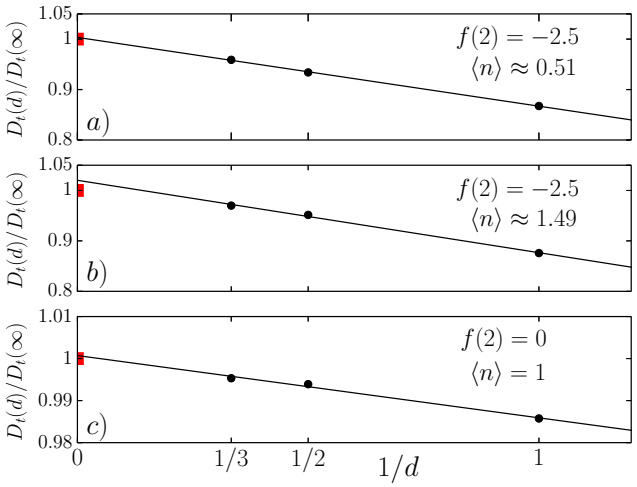

Figure 7.4: The transport diffusion as a function of the dimension, for $n_{\max} = 2$. The data are normalized w.r.t. the analytical uncorrelated result (4.7), which is denoted by $D_t(\infty)$. The black circles are from kMC simulations and the red squares are (4.7). The error bars are smaller than the symbol sizes. $1/d$ fits were performed with the method of least squares. In all three cases this fit provides a good estimate for the transport diffusion at infinite dimension, with a relative error $(D_{t,\text{fit}}(\infty)/D_t(\infty) - 1)$ of *a*) 0.3 %, *b*) 2.0 %, and *c*) 0.07 %.

7.4.3 Current fluctuations

The sufficiency condition (7.7) is not satisfied for $f(2) = -2.5$, as shown in Figure 7.5 for $d \to \infty$ (4.7). The numerically simulated $D_t(\rho)$'s do not give smooth results for (7.7), since one has to calculate the second derivative of an interpolated function. The qualitative behavior of (7.7) for finite dimensions is, however, the same as for $d \to \infty$. Starting from (4.7), one sees that (7.7) does not hold for many GEPs. One can show analytically that all GEPs with $n_{\max} = 2$ and $f(2) < 0$ do not satisfy (7.7). Numerically, one finds that GEPs with $n_{\max} = 2$ and $f(2) \gtrsim 2.917$ also do not satisfy (7.7). Although (7.7) is not satisfied for the parameters considered here, we expect that the AP is still valid. Dynamical phase transitions have only been observed for closed systems [140, 152–154], not boundary driven ones [147–149]. Also, dynamical phase transitions do not occur for currents close to the average current [141]. Currents created by time-dependent density profiles, if any, are therefore highly unlikely, and their influence on the first three moments of the current distribution is expected to be negligible.

We study the current statistics for $f(2) = -2.5$ and reservoir densities $\langle n \rangle_A = n_{\max} = 2$ ($\mu_A = \infty$) and $\langle n \rangle_B = 0$ ($\mu_B = -\infty$). Plots of $L\langle Q_t \rangle / t = I_1$ and $L\langle Q_t^2 \rangle_c / t = I_2/I_1$ as a function of the length are shown in, respectively, Figures 7.6a and 7.6b. The values predicted by the AP are given by lines, which are the one-sigma error bars. These error bars arise from the error bars on the simulated $D_t(\rho)$'s. Values from direct numerical simulations are also given with one-sigma error bars, as explained in

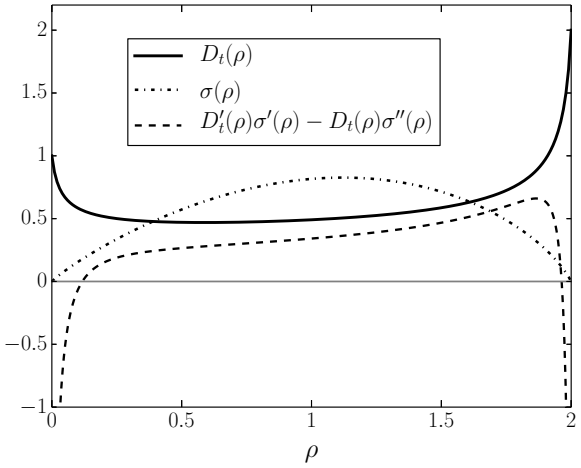

Figure 7.5: Plot of $D_t(\rho)$, $\sigma(\rho)$, and $D_t'(\rho)\sigma'(\rho) - D_t(\rho)\sigma''(\rho)$ for $f(2) = -2.5$ and $n_{\max} = 2$ in the limit $d \to \infty$ (4.7). The sufficiency condition (7.7) is satisfied if $D_t'(\rho)\sigma'(\rho) - D_t(\rho)\sigma''(\rho) \geq 0$ for all ρ.

Appendix F.2.

Let us first consider the one-dimensional data. We estimate convergence in length at $L \approx 175$. How we check for convergence in time is explained in Appendix F.2. The value for I_1, cf. Figure 7.7a, is taken from the highest considered length in Figure 7.6a. To achieve a good statistics for the second and third cumulant, we have performed an extensive simulation for length $L = 251$. The simulated values for $L\langle Q_t^2\rangle_c/t = I_2/I_1$, $F = I_2/I_1^2$, and $L\langle Q_t^3\rangle_c/t$ for this length are given in, respectively, Figures 7.7b, 7.7c, and 7.7d. I_1 from the AP is slightly higher than the directly simulated value ($I_1^{\mathrm{AP}}/I_1^{\mathrm{sim}} \approx 1.0018$). The most likely reason for this is that the simulated $D_t(\rho)$ slightly overestimates the real $D_t(\rho)$. The transport diffusion should be measured in the limit of an infinitely small concentration gradient, while of course the simulations are performed at a finite concentration gradient. Similarly, one should in principle simulate an infinitely long system, so that all boundary effects have disappeared. Both approximations cause the numerically simulated $D_t(\rho)$ to overestimate the real value [161]. Furthermore, to calculate I_1^{AP} one has to interpolate the simulated points of $D_t(\rho)$, and then integrate this interpolated function. This could introduce a small numerical imprecision. Since the relative difference is less than 0.2% we consider this result a very good agreement between I_1^{AP} and I_1^{sim}. Also the variance and the Fano factor are in very good agreement with the value from the AP: $(I_2^{\mathrm{AP}}/I_1^{\mathrm{AP}})/(I_2^{\mathrm{sim}}/I_1^{\mathrm{sim}}) \approx 1.0007$ and $F^{\mathrm{AP}}/F^{\mathrm{sim}} \approx 0.9989$.

Figure 7.7d shows the third cumulant. Although the error bars are significantly larger compared to the first two cumulants, the data indicate agreement between the AP and the directly simulated values. Finally, we plot $P(Q_t)$ obtained from kMC together with the Gaussian prediction from the first two moments of the AP in Figure 7.8. The small error on I_1 from the AP is noticeable for determining $\langle Q_t\rangle$. When using the simulated $\langle Q_t\rangle$, one sees that $P(Q_t)$ is well approximated by a Gaussian.

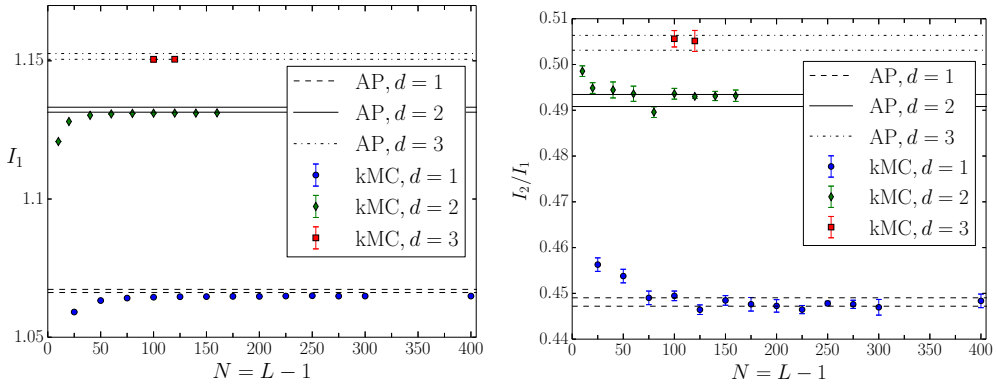

(a) (b)

Figure 7.6: (a) $L\langle Q_t\rangle/t = I_1$ and (b) $L\langle Q_t^2\rangle_c/t = I_2/I_1$, for $f(2) = -2.5$, $n_{\max} = 2$, and different lengths in one, two, and three dimensions. The lines are predictions from the AP, and represent one-sigma error bars. The points with one-sigma error bars are from a direct simulation of the current. In two (three) dimensions, the directly measured cumulants are divided by L_y (L_yL_z), see Appendix F.4.

Indeed, the skewness of $P(Q_t)$ is small $\langle Q_t^3\rangle_c/\langle Q_t^2\rangle_c^{3/2} \approx 0.034$, i.e., $P(Q_t)$ is almost symmetric. Although the difference is small, one observes that for $Q_t < 320$ the simulated $P(Q_t)$ is consistently lower than the Gaussian, while for $Q_t > 365$ it is consistently higher.

We now discuss the higher-dimensional systems. In contrast to the SSEP, all sites at the boundaries are in contact with the reservoirs. If periodic boundary conditions are imposed in the y direction, $D_t(\rho)$ converges in two dimensions to the $L_y \uparrow \infty$ limit at $L_y \approx 3$. In the simulations we take $L_y = L_z = 5$ with periodic boundary conditions. The transport diffusion is simulated for the same concentration gradients and length in the x direction as for the one-dimensional case. The different coupling to the reservoirs compared to the SSEP is done for numerical reasons. The program for the GEP is too slow to simulate a convergence in both the x direction and y (z) direction. The periodic boundary conditions employed here are equivalent to the $L_y(L_z) \uparrow \infty$ limit. All sites at the boundaries are coupled to the reservoirs because this gives the highest particle flux. The higher the particle flux, the better the current statistics for a given simulation time. If all boundary sites are connected to the reservoirs $\kappa = L_y$ and $\kappa = L_yL_z$ in, respectively, two and three dimensions. This is explained in Appendix F.4.

For two dimensions we assume convergence in length at $L \approx 120$. The error on I_1 is comparable to the one-dimensional case ($I_1^{\mathrm{AP}}/I_1^{\mathrm{sim}} \approx 1.0010$). The second and third cumulants are determined from extensive simulations at length $L = 121$. The variance and Fano factor are slightly underestimated by the AP: $(I_2^{\mathrm{AP}}/I_1^{\mathrm{AP}})/(I_2^{\mathrm{sim}}/I_1^{\mathrm{sim}}) \approx 0.9982$ and $F^{\mathrm{AP}}/F^{\mathrm{sim}} \approx 0.9971$. We consider this a very good agreement between the direct simulations and predictions from the AP. The relative difference is less than 0.3 %, and all quantities show a large overlap within their error bars. The

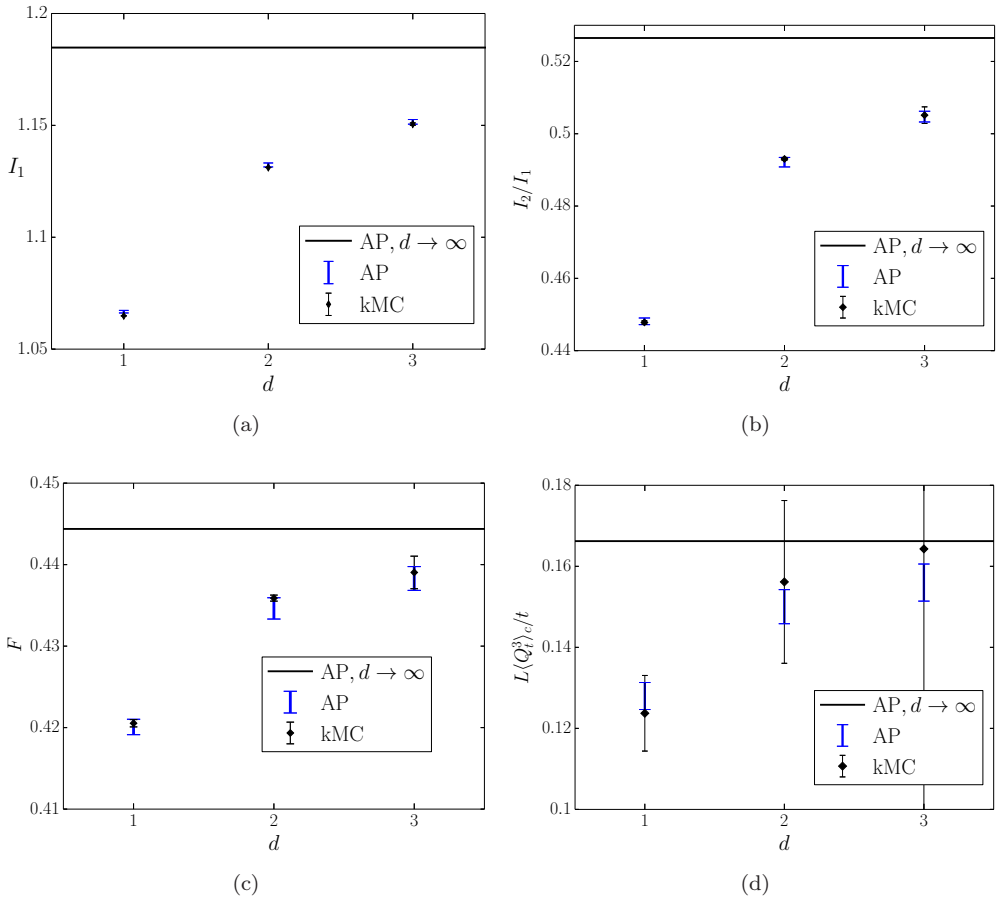

Figure 7.7: (a) I_1, (b) I_2/I_1, (c) F, (d) $L\langle Q_t^3 \rangle_c / t$ for $f(2) = -2.5$ and $n_{\max} = 2$ as a function of the dimension. Predictions from the AP are denoted by blue error bars without symbol. The limiting case $d \to \infty$ is shown as a black line. Direct numerical simulations are denoted by black diamonds. In two (three) dimensions, the directly measured cumulants are divided by L_y ($L_y L_z$), see Appendix F.4. Note that the error bar at $d = 3$ in (d) spans approximately 7 times the whole y axis.

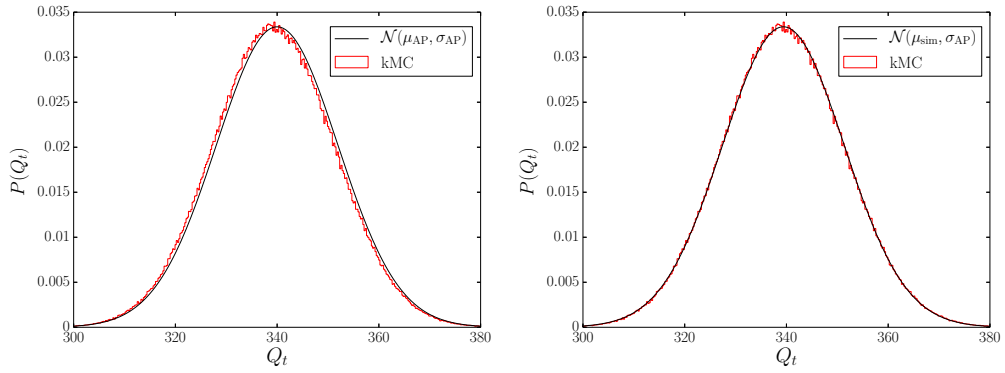

(a) (b)

Figure 7.8: $P(Q_t)$ from kMC (red) in one dimension for $n_{\max} = 2$, $f(2) = -2.5$, $L = 251$, and $t = 8.10^4$. A Gaussian distribution (black) with average and variance predicted by the AP (a) and the simulated average and variance from the AP (b) is also plotted. The data is well approximated by a Gaussian distribution.

third cumulant is also compatible with the AP prediction, although the error bar on the directly simulated value is rather large. The shape of $P(Q_t)$ is similar to the one-dimensional case (data not shown).

For three dimensions the simulation times become much longer. We therefore only simulate the current for systems of length $L = 101$ and $L = 121$. Since the two-dimensional system has converged at $L = 121$, one can safely assume that this is also the case for the three-dimensional system. The cumulants from Figure 7.7 are calculated for $L = 121$. The average, variance, and Fano factor are correctly predicted by the AP. There is insufficient data to achieve a reliable estimate for the third cumulant. The obtained value shown in Figure 7.7d agrees well with the AP, but the error bar is very large: $L\langle Q_t^3\rangle_c/t + \sigma = 0.438$ and $L\langle Q_t^3\rangle_c/t - \sigma = -0.110$. The shape of $P(Q_t)$ is similar to the one-dimensional case (data not shown).

7.5 Conclusion

To conclude, we have studied numerically current fluctuations in the symmetric simple exclusion process (SSEP) and a generalized exclusion process (GEP). For the SSEP we find that the Fano factor is independent of the spatial dimension and (macroscopic) shape of the contacts with the reservoirs. For the GEP our numerical simulations are in agreement with the predictions from the AP combined with the MFT [142]. In one and two dimensions agreement is found for the first three cumulants. In three dimensions the first two cumulants agree with the AP, while the statistics for the third cumulant are insufficient for a reliable comparison. The transport diffusion, and as a result the current statistics, depends on the dimension. Only for the SSEP and the ZRP is the transport diffusion independent of the dimension.

A more precise numerical determination of the transport diffusion from Fick's

first law is computationally very time consuming, at least using the methods presented here. It would therefore be of interest to find exact analytical results for the transport diffusion for the GEP. Another interesting question concerns the simulation of higher moments of the current distribution. This could be achieved using a sophisticated Monte Carlo algorithm to simulate rare events, see e.g. [164–166]. Both the SSEP and the ZRP satisfy the sufficiency condition for the validity of the AP (7.7). However, many GEPs do not satisfy (7.7). Hence, one might observe deviations from the predictions of the AP for large current fluctuations. An analysis of the optimal density profiles, before and (possibly) after the dynamical phase transition, is also of interest.

The quantities $D_t(\rho)$ [26] and $\sigma(\rho)$ [167] are experimentally accessible in nanoporous materials. The average particle flux through a system in contact with two particle reservoirs can also be measured [15]. If it is possible to measure the variance of the particle flux with a good precision, these techniques present an opportunity for an experimental verification of the additivity principle and, therefore, the macroscopic fluctuation theory.

Chapter 8

Conclusions and perspectives

Recent experimental progress has opened up the possibility to measure both the self- and transport diffusion in nanoporous materials with great precision at all concentrations [26, 27]. This has created a wealth of new experimental data for different molecules and materials. Inspired by cage-type nanoporous materials we have constructed a lattice model where the interaction is described by a free energy function $F(n)$ that solely depends on the number of particles in a cavity, as discussed in Chapter 2. Because of recent experimental results [28] and molecular dynamics studies [30–32], a special interest is taken in the behavior of clustering particles.

In Chapter 3 we have presented a systematic study of the dependence of the adsorption isotherm and thermodynamic factor on the shape of $F(n)$. Several studies with similar model assumptions have appeared in the literature [86]. These are, however, mostly aimed at finding a specific set of parameters that reproduce experimental adsorption isotherms. Our discussion is more general. It provides a good understanding of the effect of clustering on the adsorption isotherm and thermodynamic factor. As far as we know, the only other work to consider clustering particles on a lattice is [168], which provided an intuitive explanation of why $\Gamma^{-1} > 1$ for clustering particles in terms of fractional vacancies.

In Chapter 4 we derived analytical results for the self- and transport diffusion. These were obtained by ignoring correlations in the system. The obtained expressions are remarkably simple. Moreover, one can give a clear physical interpretation to what it means to ignore correlations in the diffusion; see Section 5.3. The effect of clustering on the self- and transport diffusion can be easily understood from our model, cf. Section 5.1. The self-, Maxwell-Stefan, and transport diffusion are investigated for different types of interactions and transition rates in Section 5.4. This analysis is much more extensive than what has appeared previously in the literature; see the discussion of similar models in Section 2.5. Given the discussion of the model assumptions in Section 5.5, it is surprising that the experimental diffusion behavior of clustering particles is so well reproduced in our model (Section 5.2).

The precision obtained in our numerical simulations seems of interest to a number of theoretical studies on the diffusion in lattice gases [169, 170]. In these works one calculates the transport-diffusion coefficient analytically. The validity of this expression is checked by comparing the stationary concentration profiles from simulations

with those predicted by the analytically obtained D_t. A direct simulation of the transport diffusion seems, however, preferable [161].

In Chapter 6 we studied the adsorption and desorption kinetics of our model. We gained interest in this topic after reading the paper of Tsotsalas *et al.* [114]. The authors describe an experiment on the adsorption and desorption kinetics in Cu-BTC, a cage-type material. A metastable state during desorption was observed, i.e., the desorption temporarily stopped. This was attributed to molecular clustering. From the discussion in Chapter 6, more specifically Figures 6.4 and 6.5, one sees that such a metastable state is not observed for clustering particles in our model. Cu-BTC consists of three different types of cavities. This can be described by a straightforward extension of the model studied in this thesis. Adsorption isotherms and thermodynamic factors are already available for a variety of different molecules [171–174], both from experiments and MD simulations. One can find the correct interaction by searching an $F(n)$ that reproduces these equilibrium quantities. The adsorption and desorption kinetics can then be studied as in Chapter 6. Such a study could maybe clarify the microscopic origin of the metastable state that is observed in [114]. One could furthermore study the self- and transport diffusion using the same free energy. This would be of interest, since there are only a few results on the diffusion of clustering molecules (such as ethanol and methanol) in Cu-BTC [172].

In Chapter 7 we predicted the probability distribution of the particle flux through the system from the additivity principle. The input for the additivity principle is the transport diffusion and the fluctuations in particle number $\langle n^2 \rangle - \langle n \rangle^2$. Both these quantities are experimentally available. The flux through a block of nanoporous material connected to two particle reservoirs at different densities can also be measured; see Section 14.9 in [15]. If it is possible to measure the second moment of the particle flux with a good precision, this could provide the first experimental verification of the additivity principle. We do, however, not know if this is possible. Chapter 7 could be seen as a first attempt to connect experimental work on nanoporous materials with results from nonequilibrium statistical mechanics. Since a lot of research on nonequilibrium statistical mechanics is done on lattice models, it is an interesting question whether this can also be done for other results.

Appendix A

Transition-state-theory calculations

Because the window separating the two cavities is a perfect choice for the transition state, the system under study is ideally suited for a TST calculation; see, e.g., Refs. [51, 52, 55, 57, 58, 66]. We use the expression given by Tunca and Ford [58]:

$$k_{nm}^{\mathrm{TST}} = (2\pi M\beta)^{-1/2}\,\frac{S}{V} n \frac{z(n-1,1,m)}{z(n)z(m)}, \tag{A.1}$$

where M is the mass of one particle, S the area of the TS surface, and V the volume of the cavity. $z(n,1,m)$ is the configurational integral with a particle in the TS:

$$z(n,1,m) = \frac{1}{SV^{n+m}} \int_S \int_{V_A} \int_{V_B} d\mathbf{r}^{\mathrm{TS}} d\mathbf{r}^{\mathrm{A}} d\mathbf{r}^{\mathrm{B}} e^{-\beta U_{\mathrm{tot}}}. \tag{A.2}$$

The labels $\mathbf{r}^{\mathrm{TS}}$, $\mathbf{r}^{\mathrm{A}}$, and $\mathbf{r}^{\mathrm{B}}$ denote the positions of all the particles in, respectively, the TS, cavity A, and cavity B. U_{tot} is the total interaction energy of the particles in the TS and both cavities. It is assumed that the TS can hold at most one particle. The TST rate of Eq. (A.1) has a simple physical interpretation: The second term gives the probability that a particle from cavity A is in the TS, while the first term $(2\pi M\beta)^{-1/2}$ is the average velocity towards cavity B of a particle in the TS. Their product gives the rate at which a particle jumps from cavity A to cavity B. Note that these rates always satisfy local detailed balance.

The total interaction energy can be written as follows:

$$U_{\mathrm{tot}} = U_{\mathrm{TS}}(\mathbf{r}^{\mathrm{TS}}) + U(\mathbf{r}^{\mathrm{A}}) + V(\mathbf{r}^{\mathrm{A}}, \mathbf{r}^{\mathrm{TS}}) + U(\mathbf{r}^{\mathrm{B}}) + V(\mathbf{r}^{\mathrm{B}}, \mathbf{r}^{\mathrm{TS}}). \tag{A.3}$$

$U_{\mathrm{TS}}(\mathbf{r}^{\mathrm{TS}})$ is the energy of the particle in the TS due to interactions with the cavity wall. The interaction energy in cavity A is equal to $U(\mathbf{r}^{\mathrm{A}}) + V(\mathbf{r}^{\mathrm{A}}, \mathbf{r}^{\mathrm{TS}})$. $U(\mathbf{r}^{\mathrm{A}})$ is the same function as in Eq. (2.10), i.e., the total interaction energy in cavity A if there is no particle in the TS. $V(\mathbf{r}^{\mathrm{A}}, \mathbf{r}^{\mathrm{TS}})$ is the contribution to the interaction energy of cavity A caused by the particle in the TS.

We now derive the transition rate of Eq. (2.12). Since there are no long-range interactions, one can make the approximation that the particle in the TS does not

influence the particles in the cavities: $V(\mathbf{r}^{\mathrm{A}}, \mathbf{r}^{\mathrm{TS}}) = V(\mathbf{r}^{\mathrm{B}}, \mathbf{r}^{\mathrm{TS}}) = 0$. Using Eq. (A.3) one finds that the configuration integral Eq. (A.2) can be written as $z(n,1,m) = z_{\mathrm{TS}} z(n) z(m)$, with the definition:

$$z_{\mathrm{TS}} = \frac{1}{S} \int_S d\mathbf{r}^{\mathrm{TS}} e^{-\beta U_{\mathrm{TS}}(\mathbf{r}^{\mathrm{TS}})}. \tag{A.4}$$

Writing $f_{\mathrm{TS}} = -kT \ln z_{\mathrm{TS}}$ one finds the transition rate:

$$k_{nm} = (2\pi M \beta)^{-1/2} \frac{S}{V} e^{-\beta f_{\mathrm{TS}}} n e^{\beta[f(n) - f(n-1)]}. \tag{A.5}$$

Rewriting this as a function of k_{10} gives Eq. (2.12).

For long-range particle interactions the assumption that $V(\mathbf{r}, \mathbf{r}^{\mathrm{TS}}) = 0$ no longer holds true. The specific form of $V(\mathbf{r}, \mathbf{r}^{\mathrm{TS}})$ depends on the interparticle interactions. An analytical calculation of $z(n,1,m)$ is difficult in this case. It also can no longer be expected that $z(n,1,m)$ can be written as a function of $f(n)$. We can, however, put upper and lower bounds on $f(n,1,m) = -kT \ln z(n,1,m)$ as a function of $f(n)$. Consider $f(n,m|\mathrm{TS}) = f(n,1,m) - f_{\mathrm{TS}}$, with f_{TS} the interaction free energy of a particle in the TS that has no interaction with particles in the cavities: $f_{\mathrm{TS}} = -kT \ln z(0,1,0)$. All interparticle interactions are then included in $f(n,m|\mathrm{TS})$. This function must lie in between:

$$f(n) + f(m) \leq f(n,m|\mathrm{TS}) \leq f(n+1) + f(m+1). \tag{A.6}$$

The lower bound becomes an equality if the particle in the TS does not interact with the particles in the cavities, in which case one finds Eq. (A.5) for k_{nm}. This corresponds to $c = 1$ in Eq. (2.11). The upper bound becomes an equality if the particle in the TS interacts with the particles in the cavities in exactly the same way as if it was located in the cavities. This gives the rates with $c = 0$ in Eq. (2.11). The rates of Eq. (2.13) are found for the choice $f(n-1,m|\mathrm{TS}) = [f(n-1) + f(n) + f(m) + f(m+1)]/2$, which is the average of the lower and upper bound. This choice takes the interaction free energy in both cavities as the average of the situation where the TS particle is present or absent in the cavity. Since half of the particle in the TS is physically in contact with the particles in cavities A and B, this is a reasonable choice. Equal importance is given to the change in free energy of both cavities, and the rate is a function of $f(n)$:

$$k_{nm} = \frac{S n e^{-(\beta/2)[f(n-1)+f(m+1)-f(n)-f(m)]}}{V\,(2\pi M\beta)^{1/2}\, e^{\beta f_{\mathrm{TS}}}}. \tag{A.7}$$

Rewriting this as a function of k_{10} gives Eq. (2.13). Note that this rate corresponds to $c = 1/2$ in Eq. (2.11).

We finally remark that the expression Eq. (A.1) assumes that all particles crossing the TS equilibrate in cavity B. This is generally not the case: The particle can recross the TS surface on short time scales and equilibrate in cavity A. Recrossings can be accounted for by including a dynamical correction factor in the rates, which is determined from short MD simulations [61]. Studies of diffusion in microporous materials using dynamically corrected TST can be found in Refs. [46, 59, 60].

Appendix B

Kinetic Monte Carlo

Consider a system with a discrete space of states that follows a Markovian dynamics. The kinetic Monte Carlo algorithm proceeds as follows:

1. Set the time at $t = 0$
2. Construct an ordered list of the rates r_i of all possible transitions ($i \in \{1, N\}$)
3. Calculate the function $R_i = \sum_{j=1}^{i} r_j$ for all $i \in \{1, N\}$
4. Draw a uniform random number u from $(0, 1]$
5. Find the transition i for which $R_{i-1} < uR_N \leq R_i$
6. Perform transition i
7. Draw a uniform random number u' from $(0, 1]$
8. Update the time $t \to t + \Delta t$ with $\Delta t = -R_N^{-1} \ln u'$
9. Return to step 2

This algorithm was implemented in C++. The chemical potentials for the concentration $\langle n \rangle$ are determined numerically with Mathematica. Random numbers are generated using the Mersenne Twister random number generator [175]. The rates k_{nm}, $k_n^{r,+}$, and $k_n^{r,-}$ depend on $F(n)$, μ_l, and μ_r; they are calculated and stored in a list before the program starts.

One-dimensional systems

We now discuss how we implemented the above algorithm to simulate one-dimensional systems. The number of particles at site i is initialized according to the probability distribution $p_n^{\text{eq}}(\mu_i)$, with

$$\mu_i = \mu_l + (\mu_r - \mu_l)\frac{i}{L+1}. \tag{B.1}$$

When measuring the self-diffusion one also has to initialize the number of labeled particles at each site. Consider the case where α_l (α_r) percent of the particles in the left (right) reservoir is labeled. Given that there are n particles at the ith site, we initialize this site with n^* labeled particles with probability

$$\binom{n}{n^*}\alpha_i^{n^*}(1-\alpha_i)^{n-n^*}, \tag{B.2}$$

where

$$\alpha_i = \alpha_l - (\alpha_l - \alpha_r)\frac{i}{L+1}. \tag{B.3}$$

This corresponds to the uncorrelated probability distribution for the labeled particles, as discussed in Section 4.2. The system is equilibrated before the measurements start. We take the equilibration time to be long, i.e., we make sure that many transitions have occurred at each site (at least 10^4) when the equilibration ends.

There are $2(L-1)$ possible transitions (particle jumps between the cavities) in the system. There are 4 possible transitions at the boundaries (addition or removal of a particle at each boundary). After initialization, the rate of each possible transition is stored in a list L_r with length $2(L-1)+4$. This list contains the rates of all possible transitions, also the ones with rate zero (for example if a cavity is full $n = n_{\max}$, particles jump to this cavity with rate zero). The sum of all the transition rates, R_{sum}, is also calculated. For the updating procedure we perform a linear search on the list to determine which transition takes place (step 5 in the algorithm). An improvement of the search speed is obtained by starting the search at the end of the list if $u > 0.5$, and otherwise starting at the beginning. After the transition is performed, the list of rates L_r is updated only for the events that are influenced by the transition. These events are all particle jumps from and to the two cavities participating in the transition. Both R_{sum} and L_r therefore only need to be updated for maximally 6 different transitions, regardless of the length of the system.

Higher-dimensional systems

For the study of the transport diffusion and current fluctuations in higher dimensions a faster algorithm is needed. We have implemented the algorithm described by Schulze [176] for our model with $n_{\max} = 2$. The idea is that, because there is a small number of different rates, the search for the transition (step 5) can be performed much faster.

Consider N distinct rates R_n (note that the notation is different compared to the previous section). In our case these rates are k_{10}, k_{20}, k_{11}, k_{21}, $k_0^{r,+}(\mu_{l/r})$, $k_1^{r,+}(\mu_{l/r})$, $k_1^{r,-}(\mu_{l/r})$, and $k_2^{r,-}(\mu_{l/r})$, so $N = 12$. We maintain N lists that contain all events that occur with rate R_n. These lists are stored in the array L_{nk}. We also maintain an address list A_m, which contains the positions of all events m in the array L_{nk}. Furthermore, we keep track of the total number of events C_n in each of the N lists.

The algorithm then proceeds as follows:

1. Calculate the overall rate $R = \sum_{n=1}^{N} R_n C_n$; retain all the partial sums S_n
2. draw a uniform random number u from $[0, R)$

3. Search through the list of partial sums S_n until $u < S_n$

4. Select an event from the set of events that occur at this rate by computing

$$k = \text{Int}\left(\frac{(S_n - u)}{R_n}\right)$$

   The event stored in the array L_{nk} at row n and column k ($k \in \{1, C_n\}$) is then selected

5. Execute this event and update the configuration

6. For the events that have their rate changed from R_{n_i} to R_{n_f} (a) move them to the end of the list n_f; add 1 to C_{n_f}; update A_m; (b) move the event listed as $L_{n_i C_{n_i}}$ into the vacated position on list n_i; reduce C_{n_i} by 1; update A_m

7. Draw a uniform random number u' from $(0, 1]$

8. Update the time $t \to t + \Delta t$ with $\Delta t = -R^{-1} \ln u'$

9. return to step 1

The search in step 3 is through a list of length 12. The computation time for this search is independent of the system size. The order of the rates in the list R_n is arbitrary. We take the system rates k_{10}, k_{20}, k_{11}, and k_{21} as the first four rates, since there are much more events with these rates than with the boundary rates. Because interactions are local, only a limited number of events need to be updated in step 6.

This algorithm should be contrasted with the algorithm for one-dimensional systems, where the search in step 5 is through a list whose size scales linearly with the system size. As a result, the computation time for a fixed number of Monte Carlo steps scales linearly with the system size. For the Schulze algorithm, this computation time is independent of the system size.

The Schulze algorithm has the drawback that it is only useful for systems with a small $n_{\max}$. The two- and three-dimensional results presented in Figures 5.10 and 5.11 were obtained using an algorithm where the list L_r was recalculated at each Monte Carlo step. This is easier to implement, but requires longer simulation times.

Appendix C

Separation of time-scales

It is shown how to obtain the master equation for a system with time-scale separation, Eq. (4.1). The theory and notation from [40] is used. The system consists of three cavities. The left and right cavity are connected to particle reservoirs. The state is denoted by (n_l, n, n_r), the number of particles in respectively the left, middle, and right cavity. Following notation from [40], "microstates" are denoted by (n_l, n, n_r), and "mesostates" are denoted by n, the number of particles in the middle cavity. By time-scale separation, we mean that the dynamics between different microstates belonging to the same mesostate is much faster than between microstates belonging to different mesostates. In our model, this means that transitions between the reservoirs and the cavities are much faster than transitions between the cavities. The probability to find the system in mesostate n equals

$$P_n = \sum_{n_l, n_r} p(n_l, n, n_r). \tag{C.1}$$

The conditional probability to be in microstate (n_l, n, n_r) being in the mesostate n is given by

$$\mathbb{P}_n(n_l, n_r) = p(n_l, n, n_r)/P_n. \tag{C.2}$$

Due to the time-scale separation, the $\mathbb{P}_n(n_l, n_r)$ evolve much faster than the mesostate probabilities P_n. The $\mathbb{P}_n(n_l, n_r)$'s obey an almost isolated dynamics inside the mesostate n, eventually relaxing to the stationary distribution $\mathbb{P}_n^{\mathrm{st}}(n_l, n_r)$:

$$\sum_{n_l', n_r'} W_{(n_l,n,n_r),(n_l',n,n_r')} \mathbb{P}_n^{\mathrm{st}}(n_l', n_r') = 0, \tag{C.3}$$

where $W_{(n_l,n,n_r),(n_l',n,n_r')}$ is the rate to jump from (n_l', n, n_r') to (n_l, n, n_r). This rate can be separated into a sum of rates due to the left and right reservoir

$$\sum_{n_l', n_r'} W_{(n_l,n,n_r),(n_l',n,n_r')} \mathbb{P}_n^{\mathrm{st}}(n_l', n_r') \tag{C.4}$$

$$= \sum_{n_l', n_r'} \left(W^{(l)}_{(n_l,n,n_r),(n_l',n,n_r)} + W^{(r)}_{(n_l,n,n_r),(n_l,n,n_r')} \right) \mathbb{P}_n^{\mathrm{st}}(n_l', n_r'), \tag{C.5}$$

where transitions with the left (right) reservoir only change n_l (n_r). Because particles only interact within the same cavity, transition rates of the reservoirs only depend on the particle number of the cavity they are connected to. Eq. (C.5) can be rewritten as

$$\sum_{n_l',n_r'} \left(W^{(l)}_{n_l,n_l'} + W^{(r)}_{n_r,n_r'} \right) \mathbb{P}^{\mathrm{st}}_n(n_l',n_r'). \tag{C.6}$$

These rates are independent of n, so $\mathbb{P}^{\mathrm{st}}_n(n_l,n_r)$ does not depend on n, allowing us to write $\mathbb{P}^{\mathrm{st}}(n_l,n_r)$. Moreover, $W^{(l)}_{n_l,n_l'}$ and $W^{(r)}_{n_r,n_r'}$ are not influenced by each other. The probabilities to have n_l or n_r particles are therefore uncorrelated, and we can write $\mathbb{P}^{\mathrm{st}}(n_l',n_r') = \mathbb{P}^{\mathrm{st}}(n_l')\mathbb{P}^{\mathrm{st}}(n_r')$. Eq. (C.6) can be written as

$$\sum_{n_l',n_r'} \left(W^{(l)}_{n_l,n_l'} \mathbb{P}^{\mathrm{st}}(n_l')\mathbb{P}^{\mathrm{st}}(n_r') + W^{(r)}_{n_r,n_r'} \mathbb{P}^{\mathrm{st}}(n_l')\mathbb{P}^{\mathrm{st}}(n_r') \right) \tag{C.7}$$

$$= \sum_{n_l'} W^{(l)}_{n_l,n_l'} \mathbb{P}^{\mathrm{st}}(n_l') + \sum_{n_r'} W^{(r)}_{n_r,n_r'} \mathbb{P}^{\mathrm{st}}(n_r') = 0. \tag{C.8}$$

The rates of the left (l) and right (r) reservoir obey local detailed balance

$$\frac{W^{(l,r)}_{i,i+1}}{W^{(l,r)}_{i+1,i}} = \exp\left(-\frac{F(i) - \mu_{(l,r)} i - F(i+1) + \mu_{(l,r)}(i+1)}{kT} \right). \tag{C.9}$$

$\mathbb{P}^{\mathrm{st}}(n_l)$ and $\mathbb{P}^{\mathrm{st}}(n_r)$ are therefore equal to the equilibrium probability distributions $p^{\mathrm{eq}}_{n_l}(\mu_l)$ and $p^{\mathrm{eq}}_{n_r}(\mu_r)$. The end result reads

$$\mathbb{P}^{\mathrm{st}}_n(n_l,n_r) = p^{\mathrm{eq}}_{n_l}(\mu_l) p^{\mathrm{eq}}_{n_r}(\mu_r). \tag{C.10}$$

Using first-order perturbation theory (see Appendix A of [40]), one can show that the master equation of P_n is given by

$$\dot{P}_n = V^{\mathrm{st}}_{n,n-1} P_{n-1} + V^{\mathrm{st}}_{n,n+1} P_{n+1} - (V^{\mathrm{st}}_{n-1,n} + V^{\mathrm{st}}_{n+1,n}) P_n, \tag{C.11}$$

with

$$V^{\mathrm{st}}_{n+1,n} = \sum_{n_l,n_r,n_l',n_r'} W_{(n_l,n+1,n_r),(n_l',n,n_r')} \mathbb{P}^{\mathrm{st}}_n(n_l',n_r') \tag{C.12}$$

$$= \sum_{n_l,n_r,n_l',n_r'} W_{(n_l,n+1,n_r),(n_l',n,n_r')} p^{\mathrm{eq}}_{n_l'}(\mu_l) p^{\mathrm{eq}}_{n_r'}(\mu_r) \tag{C.13}$$

$$= \sum_{n_l',n_r'} (k_{n_l'n} + k_{n_r'n}) p^{\mathrm{eq}}_{n_l'}(\mu_l) p^{\mathrm{eq}}_{n_r'}(\mu_r) \tag{C.14}$$

$$= \sum_{n_l'} p^{\mathrm{eq}}_{n_l'}(\mu_l) k_{n_l'n} + \sum_{n_r'} p^{\mathrm{eq}}_{n_r'}(\mu_r) k_{n_r'n}, \tag{C.15}$$

which is the equation for k^+_n Eq. (4.2). k^-_n is found similarly. One then finds that Eq. (C.11) equals Eq. (4.1).

Appendix D

First-order expansion of the current and concentration gradient

Consider a chemical potential $\mu + \delta$ with δ small. A first order expansion of $p_n^{\mathrm{eq}}(\mu)$ around $\delta = 0$ gives:

$$p_n^{\mathrm{eq}}(\mu + \delta) = p_n^{\mathrm{eq}}(\mu) + \delta\beta(n - \langle n \rangle)p_n^{\mathrm{eq}}(\mu) + O(\delta^2). \tag{D.1}$$

Since we have that $\mu_l = \mu + \delta$ and $\mu_r = \mu - \delta$, the concentration difference Eq. (4.5) is

$$dc(\mu + \delta, \mu - \delta) = \frac{1}{\lambda} \sum_{n,n_l} (n - n_l) p_{n_l}^{\mathrm{eq}}(\mu + \delta) p_n^{\mathrm{eq}}(\mu). \tag{D.2}$$

Using Eq. (D.1), one finds in first order around $\delta = 0$:

$$\begin{aligned}
&\lambda dc(\mu + \delta, \mu - \delta) = \\
&\left[\sum_{n,n_l} (n - n_l) p_n^{\mathrm{eq}}(\mu) p_{n_l}^{\mathrm{eq}}(\mu) + \delta\beta \sum_{n,n_l} (n - n_l)(n_l - \langle n \rangle) p_n^{\mathrm{eq}}(\mu) p_{n_l}^{\mathrm{eq}}(\mu) \right] \\
&= \left[\langle n \rangle - \langle n \rangle + \delta\beta \left(\langle n \rangle^2 - \langle n \rangle^2 - \langle n^2 \rangle + \langle n \rangle^2 \right) \right] \\
&= -\delta\beta \left[\langle n^2 \rangle - \langle n \rangle^2 \right].
\end{aligned} \tag{D.3}$$

Similarly, one finds for the particle flux $j(\mu+\delta,\mu-\delta)$ in first order around $\delta=0$:

$$\begin{aligned}
j(\mu+\delta,\mu-\delta) &= \sum_{n,n_l}(k_{n_l n}-k_{nn_l})p_n^{\rm eq}(\mu)p_{n_l}^{\rm eq}(\mu+\delta)\\
&= \sum_{n,n_l}\left[(k_{n_l n}-k_{nn_l})p_n^{\rm eq}(\mu)p_{n_l}^{\rm eq}(\mu)+\delta\beta(k_{n_l n}-k_{nn_l})(n_l-\langle n\rangle)p_n^{\rm eq}(\mu)p_{n_l}^{\rm eq}(\mu)\right]\\
&= \langle k\rangle-\langle k\rangle-\delta\beta\langle n\rangle(\langle k\rangle-\langle k\rangle)+\delta\beta\sum_{n,n_l}(k_{n_l n}-k_{nn_l})n_l p_n^{\rm eq}(\mu)p_{n_l}^{\rm eq}(\mu)\\
&= \delta\beta\sum_{n,n_l}(k_{n_l n}-k_{nn_l})n_l p_n^{\rm eq}(\mu)p_{n_l}^{\rm eq}(\mu)\\
&= \delta\beta\sum_{n,n_l}p_n^{\rm eq}(\mu)p_{n_l}^{\rm eq}(\mu)k_{n_l n}(n_l-n). \qquad \text{(D.4)}
\end{aligned}$$

On the last line we have used that $\sum_{n,n_l}k_{nn_l}n_l p_n^{\rm eq}(\mu)p_{n_l}^{\rm eq}(\mu)=\sum_{n,n_l}k_{n_l n}n p_n^{\rm eq}(\mu)p_{n_l}^{\rm eq}(\mu)$, which follows from a change in dummy summation indices. Writing the summation boundaries explicitly one finds

$$\begin{aligned}
j(\mu+\delta,\mu-\delta) &= \delta\beta\sum_{n_l=1}^{n_{\max}}\sum_{n=0}^{n_{\max}-1}p_n^{\rm eq}(\mu)p_{n_l}^{\rm eq}(\mu)k_{n_l n}(n_l-n)\\
&= \delta\beta\sum_{n_l=0}^{n_{\max}-1}\sum_{n=0}^{n_{\max}-1}p_n^{\rm eq}(\mu)p_{n_l+1}^{\rm eq}(\mu)k_{n_l+1,n}(n_l+1-n)\\
&= \delta\beta\sum_{n_l=0}^{n_{\max}-1}\sum_{n=0}^{n_{\max}-1}T_{n_l,n}, \qquad \text{(D.5)}
\end{aligned}$$

where we have used that $k_{0,m}=k_{m,n_{\max}}=0$ for all m, and where on the last line we have defined

$$T_{n_l,n}=p_n^{\rm eq}(\mu)p_{n_l+1}^{\rm eq}(\mu)k_{n_l+1,n}(n_l+1-n). \qquad \text{(D.6)}$$

We now show that

$$\sum_{n=0}^{n_{\max}-1}\sum_{n=0}^{n_{\max}-1}T_{n,m}=\sum_{n=0}^{n_{\max}}\sum_{m=0}^{n_{\max}}p_n^{\rm eq}(\mu)p_m^{\rm eq}(\mu)k_{nm}=\langle k\rangle. \qquad \text{(D.7)}$$

We can rewrite the second term in Eq. (D.7) as

$$\sum_{n=0}^{n_{\max}}\sum_{m=0}^{n_{\max}}p_n^{\rm eq}p_m^{\rm eq}k_{nm}=\sum_{n=0}^{n_{\max}-1}\sum_{m=0}^{n_{\max}-1}p_{n+1}^{\rm eq}p_m^{\rm eq}k_{n+1,m}, \qquad \text{(D.8)}$$

where we again use that $k_{0,m}=k_{m,n_{\max}}=0$ for all m. To shorten notation we do not write the μ dependency. Eq. (D.7) then becomes:

$$\begin{aligned}
\sum_{n=0}^{n_{\max}-1}\sum_{m=0}^{n_{\max}-1}p_{n+1}^{\rm eq}p_m^{\rm eq}k_{n+1,m}(n+1-m) &= \sum_{n=0}^{n_{\max}-1}\sum_{m=0}^{n_{\max}-1}p_{n+1}^{\rm eq}p_m^{\rm eq}k_{n+1,m}\\
\sum_{n=0}^{n_{\max}-1}\sum_{m=0}^{n_{\max}-1}T_{nm} &= \sum_{n=0}^{n_{\max}-1}\sum_{m=0}^{n_{\max}-1}K_{nm},
\end{aligned}$$

where we have defined a new quantity K_{nm}. First note that $T_{nn} = K_{nn}$ by definition. For the elements $n \neq m$ we look at the sum $T_{nm} + T_{mn}$:

$$
\begin{aligned}
&T_{nm} + T_{mn} = \\
&p^{\mathrm{eq}}_{n+1} p^{\mathrm{eq}}_{m} k_{n+1,m} + p^{\mathrm{eq}}_{n} p^{\mathrm{eq}}_{m+1} k_{m+1,n} + \left[p^{\mathrm{eq}}_{n+1} p^{\mathrm{eq}}_{m} k_{n+1,m} - p^{\mathrm{eq}}_{n} p^{\mathrm{eq}}_{m+1} k_{m+1,n} \right] (n - m) \\
&= p^{\mathrm{eq}}_{n+1} p^{\mathrm{eq}}_{m} k_{n+1,m} + p^{\mathrm{eq}}_{n} p^{\mathrm{eq}}_{m+1} k_{m+1,n} = K_{nm} + K_{mn},
\end{aligned}
$$

The term on the second line is zero because of detailed balance Eq. (2.4). This completes the proof that $j = \delta\beta\langle k \rangle$. Using these expressions for j and dc one finds the end result Eq. (4.7)

Appendix E

Self-diffusion: arbitrary percentages of labeled particles

Again consider three cavities with the separation of time-scales discussed in Appendix C. Suppose α percent of the particles is labeled in the left cavity, and β percent in the right cavity. Due to the time-scale separation, these percentages are constant. The system is in equilibrium at chemical potential μ. The stationary probability p_{n,n^*} to find n particles of which n^* are labeled in the middle cavity equals

$$p_{n,n^*} = p_n^{\mathrm{eq}}(\mu)\binom{n}{n^*}\left(\frac{\alpha+\beta}{2}\right)^{n^*}\left(1-\frac{\alpha+\beta}{2}\right)^{n-n^*} \equiv p_n^{\mathrm{eq}}(\mu)B_{n,(\alpha+\beta)/2}(n^*). \quad \text{(E.1)}$$

$B_{n,(\alpha+\beta)/2}$ is the binomial distribution with parameters n and $(\alpha+\beta)/2$. The average of $B_{n,\alpha}(n^*)$ equals αn. One can understand that this is the correct distribution from a combinatorial argument. The probability to have n particles is given by the equilibrium distribution $p_n^{\mathrm{eq}}(\mu)$; the labeling of the particles has no influence on this result. What is the probability to have n^* labeled particles if there are n particles in the cavity? A particle that enters the middle cavity has equal probability to have come from the left or right cavity, since the system is in equilibrium. The probability that a particle entering from the left is labeled equals α; when it enters from the right this probability is β. The total probability that a particle entering the middle cavity is labeled is therefore $(\alpha+\beta)/2$. The probability to have n^* labeled particles when there are n particles in the middle cavity equals

$$\binom{n}{n^*}\left(\frac{\alpha+\beta}{2}\right)^{n^*}\left(1-\frac{\alpha+\beta}{2}\right)^{n-n^*} \equiv B_{n,(\alpha+\beta)/2}(n^*). \quad \text{(E.2)}$$

This is the binomial distribution $B_{n,(\alpha+\beta)/2}(n^*)$. It should be interpreted as to probability to win n^* times out of n tries, when the probability to win equals $(\alpha+\beta)/2$. p_{n,n^*} is found by multiplying Eq. (E.2) with $p_n^{\mathrm{eq}}(\mu)$. For $\alpha = 1$ and $\beta = 0$ one recovers the result Eq. (4.8).

To verify this is the correct solution, one can solve the master equation for p_{n,n^*}. The rate for an unlabeled particle to enter the middle cavity equals $k_n^+ (1-(\alpha+\beta)/2)$; a labeled particle enters with rate $k_n^+(\alpha+\beta)/2$. The rates to leave the middle cavity depend on the state (n,n^*): An unlabeled particle leaves the middle cavity at rate $k_n^- ((n-n^*)/n)$; a labeled particle leaves the middle cavity with rate $k_n^- (n^*/n)$. The master equation reads

$$\begin{aligned}\dot{p}_{n,n^*} = &\left(1-\frac{\alpha+\beta}{2}\right) k_{n-1}^+ p_{n-1,n^*} + \frac{\alpha+\beta}{2} k_{n-1}^+ p_{n-1,n^*-1} \\ &+ \frac{n+1-n^*}{n+1} k_{n+1}^- p_{n+1,n^*} + \frac{n^*+1}{n+1} k_{n+1}^- p_{n+1,n^*+1} \\ &- \left(k_n^+ + k_n^-\right) p_{n,n^*}. \end{aligned} \tag{E.3}$$

Using the probability distribution Eq. (E.1) for p_{n,n^*}, this equation reduces to

$$\dot{p}_{n,n^*} = k_{n-1}^+ p_{n-1}^{\mathrm{eq}} + k_{n+1}^- p_{n+1}^{\mathrm{eq}} - \left(k_n^+ + k_n^-\right) p_n^{\mathrm{eq}} = \dot{p}_n^{\mathrm{eq}} = 0. \tag{E.4}$$

One finds

$$\lambda dc^* = \sum_{n_l, n_l^*, n, n^*} (n^* - n_l^*) p_{n_l}^{\mathrm{eq}}(\mu) p_n^{\mathrm{eq}}(\mu) B_{n_l,\alpha}(n_l^*) B_{n,(\alpha+\beta)/2}(n^*) \tag{E.5}$$

$$= \frac{\beta-\alpha}{2}\langle n\rangle, \tag{E.6}$$

and

$$j^* = \sum_{n_l, n_l^*, n, n^*} \left(k_{n_l n} \frac{n_l^*}{n_l} - k_{n n_l} \frac{n^*}{n}\right) p_{n_l}^{\mathrm{eq}}(\mu) p_n^{\mathrm{eq}}(\mu) B_{n_l,\alpha}(n_l^*) B_{n,(\alpha+\beta)/2}(n^*) \tag{E.7}$$

$$= -\frac{\beta-\alpha}{2}\langle n\rangle. \tag{E.8}$$

The end result reads

$$D_s = \lambda^2 \langle k\rangle / \langle n\rangle. \tag{E.9}$$

Appendix F

Simulation of Current fluctuations

F.1 Algorithms

Because we consider $\rho_A = 1$ and $\rho_B = 0$ for the SSEP, all transition rates are equal to one (also at the boundaries). All n possible transitions are stored in a list. A random integer between 0 and $n-1$ decides which transition takes place. The time between two events is taken from the distribution $p(t) = n\exp(-nt)$. For the GEP with $n_{\max} = 2$ there are 12 different rates (four in the system and four at the contact with each reservoir). Since this is a small number, one can use the algorithm described by Schulze [176], as discussed in Appendix B. For a fixed number of Monte Carlo steps, the computation time of both algorithms is constant for different system sizes.

F.2 Data analysis

The current fluctuations are measured as follows. First the system is allowed to relax to its steady state, after which we put the time at 0. The net number of particles that have entered the system between time 0 and t is denoted by $Q_{t,1}$. The net number of particles that have entered between time t and $2t$ is denoted by $Q_{t,2}$, and so on. In the simulations Q_t is determined by measuring the particle current at the left and right boundary. One then has a list $\{Q_t\}$ with N_l elements. The average is equal to

$$\overline{Q_t} = \sum_{i=1}^{N_l} Q_{t,i}/N_l. \tag{F.1}$$

For large N_l the average $\overline{Q_t}$ is a good approximation for the average $\langle Q_t \rangle$ over $P(Q_t)$. The sample variance is equal to

$$S_t^2 = \sum_{i=1}^{N_l} (Q_{t,i} - \overline{Q_t})^2/(N_l - 1). \tag{F.2}$$

For large N_l, S_t^2 converges to $\langle Q_t^2 \rangle - \langle Q_t \rangle^2$.

The one-sigma error bar on $\overline{Q_t}$ is equal to (assuming the $Q_{t,i}$'s are independent identically distributed variables)

$$\sigma = \sqrt{S_t^2 / N_l}. \tag{F.3}$$

The variance of S_t^2 is equal to

$$\mathrm{Var}(S_t^2) = \frac{1}{N_l} \left(\sigma_4 - \frac{N_l - 3}{N_l - 1} \sigma^4 \right), \tag{F.4}$$

with $\sigma_4 = \langle (Q_t - \langle Q_t \rangle)^4 \rangle$ the fourth central moment of $P(Q_t)$ (see for example exercise 7.45 in [177]). We estimate σ by (F.3). We do not estimate σ_4 directly from the simulation data, because our data do not allow for an accurate prediction of the fourth moment. Rather, we use the prediction for σ_4 from the AP [39]. One-sigma error bars on S_t^2 are equal to $\left[\mathrm{Var}\left(S_t^2\right)\right]^{1/2}$. Except for the third cumulant, all other error bars are obtained from addition and multiplication of $\overline{Q_t}$ and S_t^2. The rules for finding these error bars can be found in e.g. [178]. The Fano factor is calculated by $F(t) = S_t^2 / \overline{Q_t}$. The error bar on the third cumulant is found by bootstrapping the simulated data.

By adding the currents pairwise $Q_{t,i} + Q_{t,i+1}$ (with i odd), one can calculate $\overline{Q_{2t}}$ and S_{2t}^2 for the time interval $2t$ (with $N_l/2$ points), and so on. We study the Fano factor $F(nt)$ for $1 \leq n \leq 6$.

We now explain how we check if the data have converged in time. For clarity we consider the specific example of the two-dimensional SSEP at $L = 40$ with $t = 2.10^4$. The autocorrelation (AC) of $Q_{t,i}$ and $Q_{t,i+1}$ is

$$\mathrm{AC} = \frac{\sum_{i=1}^{N_l - 1} (Q_{t,i} - \overline{Q_t})(Q_{t,i+1} - \overline{Q_t})}{\sum_{i=1}^{N_l} (Q_{t,i} - \overline{Q_t})^2}. \tag{F.5}$$

The AC is plotted in Figure F.1a, together with the critical values (CVs) to reject the null hypothesis that AC = 0 at 95 % significance level. All points are smaller than the CVs. The point at $n = 1$ is, however, very close to the lower CV. This suggests that there is still a non-negligible AC for times $1t$. Indeed, for small times the AC is always negative. For large times, when the $Q_{t,i}$'s are uncorrelated, the AC fluctuates close to zero. The scale of "close to zero" is determined by the CVs.

The Fano factor $F(nt)$ is plotted in Figure F.1b. $F(1t)$ is slightly higher than the other 5 points, indicating again that there is not yet convergence in time. The first two point that are converged in time are $F(2t)$ and $F(3t)$. A plot in function of the number of simulated points N_l for $F(3t)$ is shown in Figure F.2. After $N_l \approx 25.10^4$ the data fluctuate around the end value F_{final}, indicating a good convergence for $F(3t)$. The average of $F(2t)$ and $F(3t)$ is taken as the final data point (as plotted in Figure 7.2a). For most points, the first two converged values are averaged to calculate the final result. If computation times are exceedingly long, such as for the SSEP in two dimensions for $L = 50$, only the first converged point is taken. In this case this point is $F(2t)$. $F(3t)$ has not yet converged as can be seen from a graph similar to Figure F.2. This explains the large error bar for $L = 50$ compared to the other points for the two-dimensional SSEP.

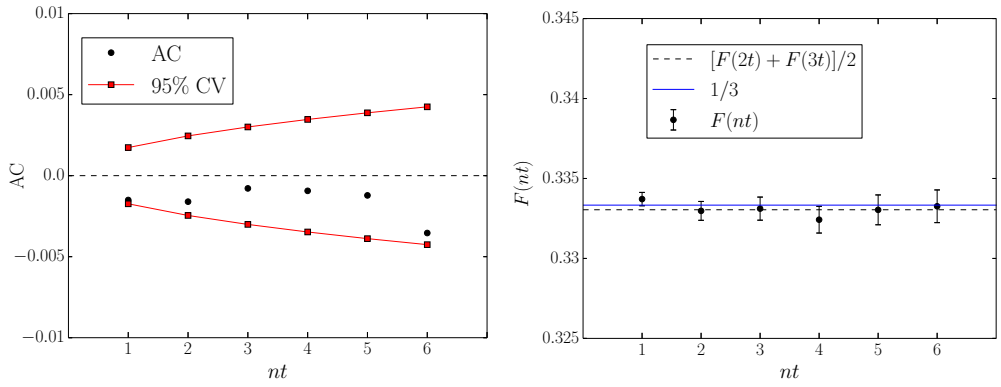

(a) (b)

Figure F.1: The two-dimensional SSEP with $t = 2.10^4$, $L = 40$, and the geometry of Figure 7.1a. (a) (circles) Autocorrelation (F.5). (red squares) Critical values to reject the null hypothesis AC = 0 at 95 % significance level. (b) (circles) $F(nt)$. (dashed line) Average of $F(2t)$ and $F(3t)$. This is the value of the data point in Figure 7.2a.

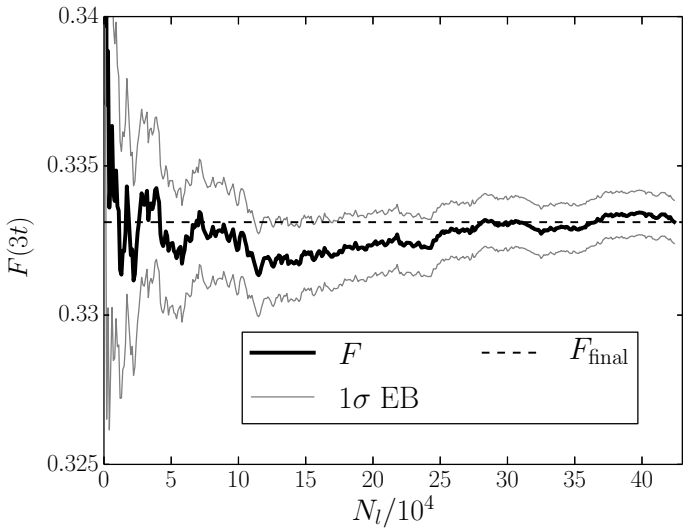

Figure F.2: The two-dimensional SSEP with $t = 2.10^4$, $L = 40$, and the geometry of Figure 7.1a. (thick black line) $F(3t)$ after N_l simulated points. (thin grey lines) one-sigma error bars. (dashed line) final value of $F(3t)$.

F.3 Simulation of transport diffusion

$D_t(\rho)$ is simulated for 30 concentrations. The length in the x direction is $L = N+1 = 16$ in two and three dimensions. In one dimension the analysis was performed for $L = 21$ and $L = 16$. The predicted values of I_1 were the same up to a relative difference of 0.006%. The data presented in Chapter 7 are for $L = 21$ in one dimension. The concentration gradient for low and high concentrations is taken between $\Delta\rho = 0.05$ and $\Delta\rho = 0.03$. For the other concentrations we take $\Delta\rho = 0.06$. The values at $\rho = 0$ and $\rho = n_{\max}$ can be calculated analytically: $D_t(0) = 1$ and $D_t(2) = 2$. An approximation for the continuous function $D_t(\rho)$ is achieved by interpolating these 32 points (using the "Interpolation" function of Mathematica). For concentrations smaller than $\rho \approx 0.04$ and higher than $\rho \approx 1.96$ the interpolated values are higher than the uncorrelated result (4.7). Since we know that correlations lower $D_t(\rho)$, we consider the uncorrelated results for these concentrations instead of the interpolated function.

F.4 Cumulant generating function in $d > 1$

The CGF $\mu_d(\lambda)$ of a d-dimensional system is equal to (cf. the last equation in [142])

$$\mu_d(\lambda) = \left[L^{d-2} \int d\vec{r} \left(\vec{\nabla} v(\vec{r}) \right)^2 \right] \times \left[L\mu_1(\lambda) \right]. \tag{F.6}$$

$\mu_1(\lambda)$ is the CGF of a one-dimensional system described by $D_{t,d}(\rho)$ and $\sigma_d(\rho)$. Consider a rectangular system of length L_x and height L_y. All sites at $x = 0$ are coupled to reservoir A and all sites at $x = L_x$ are coupled to reservoir B. L is the typical domain size, which we take equal to L_x. $v(x, y)$ is function on the domain $0 \le x \le 1$, $0 \le y \le L_y/L_x$, that satisfies the Laplace equation $\Delta v(\vec{r}) = 0$, with $v(0, y) = 0$, $v(1, y) = 1$, and Neumann boundary conditions otherwise. For the geometry we consider it is straightforward to show that $v(x, y) = x$. One then finds

$$\mu_2(\lambda) = \left[\int_0^1 \int_0^{L_y/L_x} dxdy \right] \times \left[L_x\mu_1(\lambda) \right] = L_y\mu_1(\lambda). \tag{F.7}$$

The calculation for the same geometry in three dimensions shows that $\mu_3(\lambda) = L_y L_z \mu_1(\lambda)$.

The density $\rho(x, y)$ can be found from the one-dimensional profile $\rho_1(x)$ (equation (33) in [142])

$$\rho(x, y) = \rho_1(v(x, y)) = \rho_1(x). \tag{F.8}$$

Note that the only assumption required for these results is the time-independence of the optimal density and current profiles. In the study of the two-dimensional KMP model with all the boundary sites connected to reservoirs [120, 151], one made the extra assumption that the optimal current profile is constant $\vec{j}_{\vec{J}}(\vec{r}) = \vec{J}$. This extra assumption is unnecessary: it can be derived from the time-independence of the optimal profiles and the MFT. Indeed, in one dimension time-independent profiles imply a constant current profile. A constant current profile in two dimensions follows

from (F.8). Note that for more general couplings to the reservoirs, such as in Figure 7.1, the optimal current profile need not be constant.

We have solved numerically the Laplace equation for $v(\vec{r})$ for the domain in Figure 7.2a. One finds $\mu_2(\lambda) \approx 0.663 L \mu_1(\lambda)$. This agrees with our kMC results, as discussed in Section 7.3.

Bibliography

[1] A. Einstein. On the movement of small particles suspended in stationary liquids required by the molecular-kinetic theory of heat. *Ann. Phys. (Berlin)*, 322:549, 1905.

[2] S. G. Brush. *The kind of motion we call heat*, volume 2, chapter 15. North-Holland, Amsterdam, 1976.

[3] R. M. Mazo. *Brownian motion: fluctuations, dynamics and applications*. Oxford University Press, New York, 2002.

[4] E. Frey and K. Kroy. Brownian motion: a paradigm of soft matter and biological physics. *Ann. Phys.*, 14:20, 2005.

[5] H. Mehrer and N. A. Stolwijk. Heroes and highlights in the history of diffusion. *Diffusion Fundamentals*, 11:1, 2009.

[6] J. Philibert. One and a half century of diffusion: Fick, einstein, before and beyond. *Diffusion Fundamentals*, 4:1, 2006.

[7] A. Einstein. Over de beweging van deeltjes in suspensie in vloeistoffen in rust, zoals vereist door de moleculair-kinetische theorie der warmte. *Physicalia Mag.*, 27:21, 2005. [translation: F. A. Cerulus].

[8] P. Pearle, B. Collett, K. Bart, D. Bilderback, D. Newman, and S. Samuels. What brown saw and you can too. *Am. J. Phys.*, 78:1278, 2010.

[9] R. Brown. *The Miscellaneous Botanical Works of Robert Brown*, volume 1. London, 1866.

[10] T. Li, S. Kheifets, D. Medellin, and M. G. Raizen. Measurement of the instantaneous velocity of a brownian particle. *Science*, 328:1673, 2010.

[11] R. Huang, I. Chavez, K. M. Taute, B. Lukić, S. Jeney, M. G. Raizen, and E.-L. Florin. Direct observation of the full transition from ballistic to diffusive brownian motion in a liquid. *Nat. Phys.*, 7:576, 2011.

[12] B. Alberts, A. Johnson, J. Lewis, M. Raff, K. Roberts, and P. Walter. *Molecular Biology of the Cell*. Garland Science, New York, 2002.

[13] M. Muthukumar. Polymer translocation through a hole. *J. Chem. Phys.*, 111: 10371, 1999.

[14] S. M. Bezrukov, L. Schimansky-Geier, and G. Schmid. Brownian motion in confined geometries. *Eur. Phys. J. Special Topics*, 223:3021, 2014.

[15] J. Kärger, D. M. Ruthven, and D. N. Theodorou. *Diffusion in Nanoporous Materials*. Wiley-VCH, New York, 2012.

[16] B. Smit and T. L. M. Maesen. Molecular simulations of zeolites: adsorption, diffusion, and shape selectivity. *Chem. Rev.*, 108:4125, 2008.

[17] A. R. Millward and O. M. Yaghi. Metal-organic frameworks with exceptionally high capacity for storage of carbon dioxide at room temperature. *J. Am. Chem. Soc.*, 127:17998, 2005.

[18] M. P. Suh, H. J. Park, T. K. Prasad, and D.-W. Lim. Hydrogen storage in metal-organic frameworks. *Chem. Rev.*, 112:782, 2011.

[19] Z. Wang, H. Wang, A. Mitra, L. Huang, and Y. Yan. Pure-silica zeolite low-k dielectric thin films. *Adv. Mater.*, 13:746, 2001.

[20] Database of zeolite structures. `http://www.iza-structure.org/databases/`. Accessed: 26-01-2013.

[21] M. E. Davis. Ordered porous materials for emerging applications. *Nature*, 417: 813, 2002.

[22] O. M. Yaghi, M. O'Keeffe, N. W. Ockwig, H. K. Chae, M. Eddaoudi, and J. Kim. Reticular synthesis and the design of new materials. *Nature*, 423:705, 2003.

[23] G. Férey. Hybrid porous solids: past, present, future. *Chem. Soc. Rev.*, 37:191, 2008.

[24] J. Kärger and J. Caro. Interpretation and correlation of zeolitic diffusivities obtained from nuclear magnetic resonance and sorption experiments. *J. Chem. Soc. Faraday Trans. I*, 73:1363, 1977.

[25] E. Beerdsen and B. Smit. Diffusion in confinement: Agreement between experiments better than expected. *J. Phys. Chem. B*, 110:14529, 2006.

[26] J. Kärger, T. Binder, C. Chmelik, F. Hibbe, H. Krautscheid, R. Krishna, and J. Weitkamp. Microimaging of transient guest profiles to monitor mass transfer in nanoporous materials. *Nature Mater.*, 13:333, 2014.

[27] J. Kärger. Transport phenomena in nanoporous materials. *ChemPhysChem*, 16:24, 2015.

[28] C. Chmelik, H. Bux, J. Caro, L. Heinke, F. Hibbe, T. Titze, and J. Kärger. Mass transfer in a nanoscale material enhanced by an opposing flux. *Phys. Rev. Lett.*, 104:085902, 2010.

[29] K. S. Park, Z. Ni, A. P. Côté, J. Y. Choi, R. Huang, F. J. Uribe-Romo, H. K. Chae, M. O'Keeffe, and O. M. Yaghi. Exceptional chemical and thermal stability of zeolitic imidazolate frameworks. *Proc. Natl. Acad. Sci. U.S.A.*, 103:10186, 2006.

[30] R. Krishna and J. M. van Baten. Hydrogen bonding effects in adsorption of water-alcohol mixtures in zeolites and the consequences for the characteristics of the maxwell-stefan diffusivities. *Langmuir*, 26:10854, 2010.

[31] R. Krishna and J. M. van Baten. Highlighting a variety of unusual characteristics of adsorption and diffusion in microporous materials induced by clustering of guest molecules. *Langmuir*, 26:8450, 2010.

[32] R. Krishna and J. M. van Baten. Investigating cluster formation in adsorption of co2, ch4, and ar in zeolites and metal organic frameworks at subcritical temperatures. *Langmuir*, 26:3981, 2010.

[33] S. Martens, G. Schmid, L. Schimansky-Geier, and P. Hänggi. Entropic particle transport: Higher-order corrections to the fick-jacobs diffusion equation. *Phys. Rev. E*, 83:051135, 2011.

[34] P. Kalinay. Effective transport equations in quasi 1d systems. *Eur. Phys. J. Special Topics*, 223:3027, 2014.

[35] J. L. Anderson and C. C. Reed. Diffusion of spherical macromolecules at finite concentration. *J. Chem. Phys.*, 64:3240, 1976.

[36] B. U. Felderhof. Diffusion of interacting brownian particles. *J. Phys. A: Math. Gen.*, 11:929, 1978.

[37] C. Van den Broeck, F. Lostak, and H. N. W. Lekkerkerker. The effect of direct interactions on brownian diffusion. *J. Chem. Phys.*, 74:2006, 1981.

[38] H. Löwen and M. Heinen. Dynamical density functional theory for the diffusion of injected brownian particles. *Eur. Phys. J. Special Topics*, 223:3113, 2014.

[39] T. Bodineau and B. Derrida. Current fluctuations in nonequilibrium diffusive systems: an additivity principle. *Phys. Rev. Lett.*, 92:180601, 2004.

[40] M. Esposito. Stochastic thermodynamics under coarse graining. *Phys. Rev. E*, 85:041125, 2012.

[41] N. G. Van Kampen. *Stochastic Processes in Physics and Chemistry*. North-Holland, Amsterdam, 1981.

[42] P. Hänggi, P. Talkner, and M. Borkovec. Reaction-rate theory: fifty years after kramers. *Rev. Mod. Phys.*, 62:251, 1990.

[43] R. Krishna. Describing the diffusion of guest molecules inside porous structures. *J. Phys. Chem. C*, 113:19756, 2009.

[44] T. Ala-Nissila, R. Ferrando, and S. C. Ying. Collective and single particle diffusion on surfaces. *Adv. Phys.*, 51:949, 2002.

[45] D. Paschek and R. Krishna. Inter-relation between self-and jump-diffusivities in zeolites. *Chem. Phys. Lett.*, 333:278, 2001.

[46] E. Beerdsen, D. Dubbeldam, and B. Smit. Loading dependence of the diffusion coefficient of methane in nanoporous materials. *J. Phys. Chem. B*, 110:22754, 2006.

[47] R. Krishna and J. M. van Baten. Influence of adsorption thermodynamics on guest diffusivities in nanoporous crystalline materials. *Phys. Chem. Chem. Phys.*, 15:7994, 2013.

[48] E. Beerdsen, D. Dubbeldam, and B. Smit. Molecular understanding of diffusion in confinement. *Phys. Rev. Lett.*, 95:164505, 2005.

[49] H. Bux, C. Chmelik, J. M. van Baten, R. Krishna, and J. Caro. Novel mof-membrane for molecular sieving predicted by ir-diffusion and molecular modeling. *Adv. Mater.*, 22:4741, 2010.

[50] H. Liu et al. A hybrid absorption–adsorption method to efficiently capture carbon. *Nat. Commun.*, 5:5147, 2014.

[51] D. M. Ruthven and R. I. Derrah. Transition state theory of zeolitic diffusion. diffusion of ch4 and cf4 in 5a zeolite. *J. Chem. Soc., Faraday Trans. 1*, 68:2332, 1972.

[52] J. Kärger, H. Pfeifer, and R. Haberlandt. Application of absolute rate theory to intracrystalline diffusion in zeolites. *J. Chem. Soc., Faraday Trans. 1*, 76: 1569, 1980.

[53] D. M. Ruthven. Diffusion in type a zeolites: New insights from old data. *Microporous Mesoporous Mater.*, 162:69, 2012.

[54] R. Krishna. Diffusion in porous crystalline materials. *Chem. Soc. Rev.*, 41:3099, 2012.

[55] R. L. June, A. T. Bell, and D. N. Theodorou. Transition-state studies of xenon and sulfur hexafluoride diffusion in silicalite. *J. Phys. Chem.*, 95:8866, 1991.

[56] R. Q. Snurr, A. T. Bell, and D. N. Theodorou. Investigation of the dynamics of benzene in silicalite using transition-state theory. *J. Phys. Chem.*, 98:11948, 1994.

[57] C. Tunca and D. M. Ford. A transition-state theory approach to adsorbate dynamics at arbitrary loadings. *J. Chem. Phys.*, 111:2751, 1999.

[58] C. Tunca and D. M. Ford. Modeling cage-to-cage dynamics of adsorbates at arbitrary loadings with dynamically corrected transition-state theory. *J. Phys. Chem. B*, 106:10982, 2002.

[59] C. Tunca and D. M. Ford. A hierarchical approach to the molecular modeling of diffusion and adsorption at nonzero loading in microporous materials. *Chem. Eng. Sci.*, 58:3373, 2003.

[60] E. Beerdsen, B. Smit, and D. Dubbeldam. Molecular simulation of loading dependent slow diffusion in confined systems. *Phys. Rev. Lett.*, 93:248301, 2004.

[61] D. Dubbeldam, E. Beerdsen, T. J. H. Vlugt, and B. Smit. Molecular simulation of loading-dependent diffusion in nanoporous materials using extended dynamically corrected transition state theory. *J. Chem. Phys.*, 122:224712, 2005.

[62] P. Demontis, F. G. Pazzona, and G. B. Suffritti. Introducing a cellular automaton as an empirical model to study static and dynamic properties of molecules adsorbed in zeolites. *J. Phys. Chem. B*, 112:12444, 2008.

[63] F. G. Pazzona, P. Demontis, and G. B. Suffritti. From thermodynamic cell models to partitioning cellular automata for diffusion in zeolites. i. structure of the algorithm. *J. Chem. Phys.*, 131:234703, 2009.

[64] F. G. Pazzona, P. Demontis, and G. B. Suffritti. From thermodynamic cell models to partitioning cellular automata for diffusion in zeolites. ii. static and dynamic properties. *J. Chem. Phys.*, 131:234704, 2009.

[65] P. Demontis, F. G. Pazzona, and G. B. Suffritti. Effective interactions in multisite cells for adsorption in microporous materials. *J. Chem. Phys.*, 130:164701, 2009.

[66] S. M. Auerbach. Theory and simulation of jump dynamics, diffusion and phase equilibrium in nanopores. *Int. Rev. Phys. Chem.*, 19:155, 2000.

[67] C. Saravanan, F. Jousse, and S. M. Auerbach. Ising model of diffusion in molecular sieves. *Phys. Rev. Lett.*, 80:5754, 1998.

[68] S. Y. Bhide and S. Yashonath. Dependence of the self-diffusion coefficient on the sorbate concentration: A two-dimensional lattice gas model with and without confinement. *J. Chem. Phys.*, 111:1658, 1999.

[69] M.-O. Coppens, A. T. Bell, and A. K. Chakraborty. Dynamic monte-carlo and mean-field study of the effect of strong adsorption sites on self-diffusion in zeolites. *Chem. Eng. Sci.*, 54:3455, 1999.

[70] F. J. Keil, R. Krishna, and M.-O. Coppens. Modeling of diffusion in zeolites. *Rev. Chem. Eng.*, 16:71, 2000.

[71] D. A. Reed and G. Ehrlich. Surface diffusion, atomic jump rates and thermodynamics. *Surf. Sci.*, 102:588, 1981.

[72] D. A. Reed and G. Ehrlich. Surface diffusivity and the time correlation of concentration fluctuations. *Surf. Sci.*, 105:603, 1981.

[73] R. Krishna, D. Paschek, and R. Baur. Modeling the occupancy dependence of diffusivities in zeolites. *Microporous Mesoporous Mater.*, 76:233, 2004.

[74] B. Derrida. Non-equilibrium steady states: fluctuations and large deviations of the density and of the current. *J. Stat. Mech.*, 2007:P07023, 2007.

[75] C. Kipnis and C. Landim. *Scaling Limits of Interacting Particle Systems*. Springer-Verlag, 1999.

[76] L. Bertini, A. De Sole, D. Gabrielli, G. Jona-Lasinio, and C. Landim. Stochastic interacting particle systems out of equilibrium. *J. Stat. Mech.*, 2007:P07014, 2007.

[77] S. Mossa, F. Sciortino, P. Tartaglia, and E. Zaccarelli. Ground-state clusters for short-range attractive and long-range repulsive potentials. *Langmuir*, 20:10756, 2004.

[78] D. M. Ruthven. Simple theoretical adsorption isotherm for zeolites. *Nat. Phys. Sci.*, 232:70, 1971.

[79] K. G. Ayappa, C. R. Kamala, and T. A. Abinandanan. Mean field lattice model for adsorption isotherms in zeolite naa. *J. Chem. Phys.*, 110:8714, 1999.

[80] K. G. Ayappa. Statistical thermodynamics of lattice models in zeolites: Implications of local versus global mean field interactions. *J. Chem. Phys.*, 111:4736, 1999.

[81] J. H. Bae, Y. R. Lim, and J. Sung. Statistical mechanics of molecular adsorption: Effects of adsorbate interaction on isotherms. *Langmuir*, 24:25692, 2008.

[82] E. J. García, J. Pérez-Pellitero, C. Jallut, and G. D. Pirngruber. Modeling adsorption properties on the basis of microscopic, molecular, and structural descriptors for nonpolar adsorbents. *Langmuir*, 29:9398, 2013.

[83] E. J. García, J. Pérez-Pellitero, C. Jallut, and G. D. Pirngruber. How to optimize the electrostatic interaction between a solid adsorbent and co2. *J. Phys. Chem. C*, 118:9458, 2014.

[84] P. R. Van Tassel, H. T. Davis, and A. V. McCormick. Open-system monte carlo simulations of xe in naa. *J. Chem. Phys.*, 98:8919, 1993.

[85] P. R. Van Tassel, H. T. Davis, and A. V. McCormick. Adsorption simulations of small molecules and their mixtures in a zeolite micropore. *Langmuir*, 10:1257, 1994.

[86] D. M. Ruthven. *Principles of adsorption and adsorption processes*. John Wiley and Sons, Inc., 1984.

[87] L. D. Gelb, K. E. Gubbins, R. Radhakrishnan, and M. Sliwinska-Bartkowiak. Phase separation in confined systems. *Rep. Prog. Phys.*, 62:1573, 1999.

[88] Y. B. Melnichenko, G. D. Wignall, D. R. Cole, and H. Frielinghaus. Density fluctuations near the liquid-gas critical point of a confined fluid. *Phys. Rev. E*, 69:057102, 2004.

[89] Y. B. Melnichenko, G. D. Wignall, D. R. Cole, H. Frielinghaus, and L. A. Bulavin. Liquid–gas critical phenomena under confinement: small-angle neutron scattering studies of co2 in aerogel. *J. Mol. Liq.*, 120:7, 2005.

[90] R. Gomer. Diffusion of adsorbates on metal surfaces. *Rep. Prog. Phys.*, 53:917, 1990.

[91] M. R. Evans and T. Hanney. Nonequilibrium statistical mechanics of the zero-range process and related models. *J. Phys. A: Math. Gen.*, 38:R195, 2005.

[92] E. Levine, D. Mukamel, and G. M. Schütz. Zero-range process with open boundaries. *J. Stat. Phys.*, 120:759, 2005.

[93] A. Asselah, R. Brito, and J. L. Lebowitz. Self-diffusion in simple models: Systems with long-range jumps. *J. Stat. Phys.*, 87:1131, 1997.

[94] H. Jobic, J. Kärger, and M. Bée. Simultaneous measurement of self- and transport diffusivities in zeolites. *Phys. Rev. Lett.*, 82:4260, 1999.

[95] L. Heinke, D. Tzoulaki, C. Chmelik, F. Hibbe, J. M. van Baten, H. Lim, J. Li, R. Krishna, and J. Kärger. Assessing guest diffusivities in porous hosts from transient concentration profiles. *Phys. Rev. Lett.*, 102:065901, 2009.

[96] F. Salles, H. Jobic, G. Maurin, M. M. Koza, P. L. Llewellyn, T. Devic, C. Serre, and G. Ferey. Experimental evidence supported by simulations of a very high h2 diffusion in metal organic framework materials. *Phys. Rev. Lett.*, 100:245901, 2008.

[97] N. Rosenbach, H. Jobic, A. Ghoufi, F. Salles, G. Maurin, S. Bourrelly, P. L. Llewellyn, T. Devic, C. Serre, and G. Férey. Quasi-elastic neutron scattering and molecular dynamics study of methane diffusion in metal organic frameworks mil-47(v) and mil-53(cr). *Angew. Chem. Int. Ed.*, 47:6611, 2008.

[98] D. Tzoulaki, L. Heinke, H. Lim, J. Li, D. Olson, J. Caro, R. Krishna, C. Chmelik, and J. Kärger. Assessing surface permeabilities from transient guest profiles in nanoporous host materials. *Angew. Chem. Int. Ed.*, 48:3525, 2009.

[99] H. Jobic. Investigation of diffusion in molecular sieves by neutron scattering techniques. In H. G. Karge and J. Weitkamp, editors, *Adsorption and Diffusion*, volume 7, pages 207–233. Springer-Verlag, Berlin, Heidelberg, 2008.

[100] C. Chmelik, J. Kärger, M. Wiebcke, J. Caro, J. M. van Baten, and R. Krishna. Adsorption and diffusion of alkanes in cubtc crystals investigated using infra-red microscopy and molecular simulations. *Microporous Mesoporous Mater.*, 117: 22, 2009.

[101] F. Salles, H. Jobic, T. Devic, P. L. Llewellyn, C. Serre, G. Férey, and G. Maurin. Self and transport diffusivity of co2 in the metal-organic framework mil-47(v) explored by quasi-elastic neutron scattering experiments and molecular dynamics simulations. *ACS Nano*, 4:143, 2010.

[102] R. Krishna and J. M. van Baten. A molecular dynamics investigation of the unusual concentration dependencies of fick diffusivities in silica mesopores. *Microporous Mesoporous Mater.*, 138:228, 2011.

[103] R. Krishna and J. M. van Baten. Insights into diffusion of gases in zeolites gained from molecular dynamics simulations. *Microporous Mesoporous Mater.*, 109:91, 2008.

[104] J. A. Northby. Structure and binding of lennardjones clusters: 13 < n < 147. *J. Chem. Phys.*, 87:6166, 1987.

[105] I. Vattulainen, S. C. Ying, T. Ala-Nissila, and J. Merikoski. Memory effects and coverage dependence of surface diffusion in a model adsorption system. *Phys. Rev. B*, 59:7697, 1999.

[106] J. B. Taylor and I. Langmuir. The evaporation of atoms, ions and electrons from caesium films on tungsten. *Phys. Rev.*, 44:423, 1933.

[107] K. Nelissen, V. R. Misko, and F. M. Peeters. Single-file diffusion of interacting particles in a one-dimensional channel. *Europhys. Lett.*, 80:56004, 2007.

[108] D. Lucena, D. V. Tkachenko, K. Nelissen, V. R. Misko, W. P. Ferreira, G. A. Farias, and F. M. Peeters. Transition from single-file to two-dimensional diffusion of interacting particles in a quasi-one-dimensional channel. *Phys. Rev. E*, 85:031147, 2012.

[109] E. Beerdsen, D. Dubbeldam, and B. Smit. Understanding diffusion in nanoporous materials. *Phys. Rev. Lett.*, 96:044501, 2006.

[110] F. G. Pazzona, P. Demontis, and G. B. Suffritti. A grand-canonical monte carlo study of the adsorption properties of argon confined in zif-8: Local thermodynamic modeling. *J. Phys. Chem. C*, 117:349, 2012.

[111] T. Chokbunpiam, R. Chanajaree, O. Saengsawang, S. Reimann, C. Chmelik, S. Fritzsche, J. Caro, T. Remsungnen, and S. Hannongbua. The importance of lattice flexibility for the migration of ethane in zif-8: Molecular dynamics simulations. *Microporous Mesoporous Mater.*, 174:126, 2013.

[112] M. K. F. Abouelnasr and B. Smit. Diffusion in confinement: kinetic simulations of self- and collective diffusion behavior of adsorbed gases. *Phys. Chem. Chem. Phys.*, 14:11600, 2012.

[113] S. E. Jee and D. S. Sholl. Carbon dioxide and methane transport in ddr zeolite: Insights from molecular simulations into carbon dioxide separations in small pore zeolites. *J. Am. Chem. Soc.*, 131:7896, 2009.

[114] M. Tsotsalas, P. Hejcik, K. Sumida, Z. Kalay, S. Furukawa, and S. Kitagawa. Impact of molecular clustering inside nanopores on desorption processes. *J. Am. Chem. Soc.*, 135:4608, 2013.

[115] J. Kärger, C. Chmelik, L. Heinke, and R. Valiullin. A new view of diffusion in nanoporous materials. *Chem. Ing. Tech.*, 82:779, 2010.

[116] John Crank. *The mathematics of diffusion.* Oxford university press, 1979.

[117] D. R. Garg and D. M. Ruthven. The effect of the concentration dependence of diffusivity on zeolitic sorption curves. *Chem. Eng. Sci.*, 27:417, 1972.

[118] R. Krishna and R. Baur. Modelling issues in zeolite based separation processes. *Sep. Purif. Technol.*, 33:213, 2003.

[119] C. Appert-Rolland, B. Derrida, V. Lecomte, and F. van Wijland. Universal cumulants of the current in diffusive systems on a ring. *Phys. Rev. E*, 78: 021122, 2008.

[120] P. I. Hurtado, C. P. Espigares, J. J. del Pozo, and P. L. Garrido. Thermodynamics of currents in nonequilibrium diffusive systems: Theory and simulation. *J. Stat. Phys.*, 154:214, 2014.

[121] P. I. Hurtado and P. L. Garrido. Current fluctuations and statistics during a large deviation event in an exactly solvable transport model. *J. Stat. Mech.*, 2009:P02032, 2009.

[122] P. I. Hurtado, C. Pérez-Espigares, J. J. del Pozo, and P. L. Garrido. Symmetries in fluctuations far from equilibrium. *Proc. Natl. Acad. Sci. U.S.A.*, 108:7704, 2011.

[123] S. Prolhac and K. Mallick. Cumulants of the current in a weakly asymmetric exclusion process. *J. Phys. A: Math. Theor.*, 42:175001, 2009.

[124] M. Gorissen, J. Hooyberghs, and C. Vanderzande. Density-matrix renormalization-group study of current and activity fluctuations near nonequilibrium phase transitions. *Phys. Rev. E*, 79:020101, 2009.

[125] M. Gorissen and C. Vanderzande. Finite size scaling of current fluctuations in the totally asymmetric exclusion process. *J. Phys. A: Math. Theor.*, 44:115005, 2011.

[126] M. Gorissen, A. Lazarescu, K. Mallick, and C. Vanderzande. Exact current statistics of the asymmetric simple exclusion process with open boundaries. *Phys. Rev. Lett.*, 109:170601, 2012.

[127] A. Kundu, S. Sabhapandit, and A. Dhar. Large deviations of heat flow in harmonic chains. *J. Stat. Mech.*, 2011:P03007, 2011.

[128] A. Lazarescu and K. Mallick. An exact formula for the statistics of the current in the tasep with open boundaries. *J. Phys. A: Math. Theor.*, 44:315001, 2011.

[129] C. Maes, K. Netočný, and B. Wynants. Steady state statistics of driven diffusions. *Physica A*, 387:2675, 2008.

[130] R. Villavicencio-Sanchez, R. J. Harris, and H. Touchette. Current loops and fluctuations in the zero-range process on a diamond lattice. *J. Stat. Mech.*, 2012:P07007, 2012.

[131] M. Polettini and M. Esposito. Transient fluctuation theorems for the currents and initial equilibrium ensembles. *J. Stat. Mech.*, 2014:P10033, 2014.

[132] A. Vilenkin, B. Meerson, and P. V. Sasorov. Extreme fluctuations of current in the symmetric simple exclusion process: a non-stationary setting. *J. Stat. Mech.*, 2014:P06007, 2014.

[133] R. Villavicencio-Sanchez, R. J. Harris, and H. Touchette. Fluctuation relations for anisotropic systems. *Europhys. Lett.*, 105:30009, 2014.

[134] H. Touchette. The large deviation approach to statistical mechanics. *Phys. Rep.*, 478:1, 2009.

[135] A. Einstein. Theorie der opaleszenz von homogenen flüssigkeiten und flüssigkeitsgemischen in der nähe des kritischen zustandes. *Ann. Phys.*, 33: 1275, 1910.

[136] G. Jona-Lasinio. Thermodynamics of stationary states. *J. Stat. Mech.*, 2014: P02004, 2014.

[137] L. Bertini, A. De Sole, D. Gabrielli, G. Jona-Lasinio, and C. Landim. Fluctuations in stationary nonequilibrium states of irreversible processes. *Phys. Rev. Lett.*, 87:040601, 2001.

[138] L. Bertini, A. De Sole, D. Gabrielli, G. Jona-Lasinio, and C. Landim. Macroscopic fluctuation theory for stationary non-equilibrium states. *J. Stat. Phys.*, 107:635, 2002.

[139] L. Bertini, A. De Sole, D. Gabrielli, G. Jona-Lasinio, and C. Landim. Current fluctuations in stochastic lattice gases. *Phys. Rev. Lett.*, 94:030601, 2005.

[140] L. Bertini, A. De Sole, D. Gabrielli, G. Jona-Lasinio, and C. Landim. Non equilibrium current fluctuations in stochastic lattice gases. *J. Stat. Phys.*, 123: 237–276, 2006.

[141] L. Bertini, A. De Sole, D. Gabrielli, G. Jona-Lasinio, and C. Landim. Macroscopic fluctuation theory. *arXiv:1404.6466*, 2014.

[142] E. Akkermans, T. Bodineau, B. Derrida, and O. Shpielberg. Universal current fluctuations in the symmetric exclusion process and other diffusive systems. *Europhys. Lett.*, 103:20001, 2013.

[143] T. Bodineau and B. Derrida. Cumulants and large deviations of the current through non-equilibrium steady states. *C. R. Physique*, 8:540, 2007.

[144] F. Van Wijland and Z. Rácz. Large deviations in weakly interacting boundary driven lattice gases. *J. Stat. Phys.*, 118:27, 2005.

[145] R. J. Harris, A. Rákos, and G. M. Schütz. Current fluctuations in the zero-range process with open boundaries. *J. Stat. Mech.*, 2005:P08003, 2005.

[146] M. Žnidarič. Large-deviation statistics of a diffusive quantum spin chain and the additivity principle. *Phys. Rev. E*, 89:042140, 2014.

[147] P. Hurtado and P. Garrido. Test of the additivity principle for current fluctuations in a model of heat conduction. *Phys. Rev. Lett.*, 102:250601, 2009.

[148] P. I. Hurtado and P. L. Garrido. Large fluctuations of the macroscopic current in diffusive systems: A numerical test of the additivity principle. *Phys. Rev. E*, 81:041102, 2010.

[149] M. Gorissen and C. Vanderzande. Current fluctuations in the weakly asymmetric exclusion process with open boundaries. *Phys. Rev. E*, 86:051114, 2012.

[150] K. Saito and A. Dhar. Additivity principle in high-dimensional deterministic systems. *Phys. Rev. Lett.*, 107:250601, 2011.

[151] C. Pérez-Espigares, J. J. del Pozo, P. L. Garrido, and P. I. Hurtado. Large deviations of the current in a two-dimensional diffusive system. *AIP Conf. Proc.*, 1332:204, 2011.

[152] T. Bodineau and B. Derrida. Distribution of current in nonequilibrium diffusive systems and phase transitions. *Phys. Rev. E*, 72:066110, 2005.

[153] P. I. Hurtado and P. L. Garrido. Spontaneous symmetry breaking at the fluctuating level. *Phys. Rev. Lett.*, 107:180601, 2011.

[154] C. P. Espigares, P. L. Garrido, and P. I. Hurtado. Dynamical phase transition for current statistics in a simple driven diffusive system. *Phys. Rev. E*, 87: 032115, 2013.

[155] B. Derrida, B. Douçot, and P-E Roche. Current fluctuations in the one-dimensional symmetric exclusion process with open boundaries. *J. Stat. Phys.*, 115:717, 2004.

[156] R. J. Barlow. *Statistics: A Guide to the Use of Statistical Methods in the Physical Sciences*. John Wiley and Sons, 1989.

[157] T. Becker, K. Nelissen, B. Cleuren, B. Partoens, and C. Van den Broeck. Diffusion of interacting particles in discrete geometries. *Phys. Rev. Lett.*, 111:110601, 2013.

[158] T. Becker, K. Nelissen, B. Cleuren, B. Partoens, and C. Van den Broeck. Diffusion of interacting particles in discrete geometries: Equilibrium and dynamical properties. *Phys. Rev. E*, 90:052139, 2014.

[159] T. Becker, K. Nelissen, B. Cleuren, B. Partoens, and C. Van den Broeck. Adsorption and desorption in confined geometries: A discrete hopping model. *Eur. Phys. J. Special Topics*, 223:3243, 2014.

[160] Bernard Derrida. Non-equilibrium steady states: fluctuations and large deviations of the density and of the current. *J. Stat. Mech.*, 2007:P07023, 2007.

[161] T. Becker, K. Nelissen, B. Cleuren, B. Partoens, and C. Van den Broeck. Comment on "generalized exclusion processes: Transport coefficients". *arXiv:1412.6324*, 2014.

[162] R. Kutner. Chemical diffusion in the lattice gas of non-interacting particles. *Phys. Lett. A*, 81:239, 1981.

[163] M. R. Evans, S. N. Majumdar, and R. K. P. Zia. Factorized steady states in mass transport models on an arbitrary graph. *J. Phys. A: Math. Gen.*, 39:4859, 2006.

[164] C. Giardinà, J. Kurchan, and L. Peliti. Direct evaluation of large-deviation functions. *Phys. Rev. Lett.*, 96:120603, 2006.

[165] V. Lecomte and J. Tailleur. A numerical approach to large deviations in continuous time. *J. Stat. Mech.*, 2007:P03004, 2007.

[166] T. Nemoto and S.-i. Sasa. Computation of large deviation statistics via iterative measurement-and-feedback procedure. *Phys. Rev. Lett.*, 112:090602, 2014.

[167] H. Jobic, N. Laloué, C. Laroche, J. M. van Baten, and R. Krishna. Influence of isotherm inflection on the loading dependence of the diffusivities of n-hexane and n-heptane in mfi zeolite. quasi-elastic neutron scattering experiments supplemented by molecular simulations. *J. Phys. Chem. B*, 110:2195, 2006.

[168] R. Krishna and J. M. van Baten. A rationalization of the type iv loading dependence in the kärger–pfeifer classification of self-diffusivities. *Microporous Mesoporous Mater.*, 142:745, 2011.

[169] U. Bhat and P. L. Krapivsky. Exclusion processes with avalanches. *Phys. Rev. E*, 90:012133, 2014.

[170] C. Arita, P. L. Krapivsky, and K. Mallick. Generalized exclusion processes: Transport coefficients. *Phys. Rev. E*, 90:052108, 2014.

[171] J. J. Gutiérrez-Sevillano, J. M. Vicent-Luna, D. Dubbeldam, and S. Calero. Molecular mechanisms for adsorption in cu-btc metal organic framework. *J. Phys. Chem. C*, 117:11357, 2013.

[172] T. R. C. Van Assche, T. Duerinck, J. J. Gutiérrez Sevillano, S. Calero, G. V. Baron, and J. F. M. Denayer. High adsorption capacities and two-step adsorption of polar adsorbates on copper–benzene-1, 3, 5-tricarboxylate metal–organic framework. *J. Phys. Chem. C*, 117:18100, 2013.

[173] V. K. Peterson, P. D. Southon, G. J. Halder, D. J. Price, J. J. Bevitt, and C. J. Kepert. Guest adsorption in the nanoporous metal–organic framework cu3 (1, 3, 5-benzenetricarboxylate) 2: Combined in situ x-ray diffraction and vapor sorption. *Chem. Mater.*, 26:4712, 2014.

[174] S. Calero and P. Gómez-Álvarez. Insights into the adsorption of water and small alcohols on the open-metal sites of cu-btc via molecular simulation. *J. Phys. Chem. C*, 119:476, 2014.

[175] M. Matsumoto and T. Nishimura. Mersenne twister: A 623-dimensionally equidistributed uniform pseudo-random number generator. *ACM Transactions on Modeling and Computer Simulation*, 8:3, 1998.

[176] T. P. Schulze. Kinetic monte carlo simulations with minimal searching. *Phys. Rev. E*, 65:036704, 2002.

[177] G. Casella and R. L. Berger. *Statistical inference*. Duxbury Pacific Grove, CA, second edition, 2002.

[178] P. R. Bevington and D. Keith Robinson. *Data Reduction and Error Analysis for the Physical Sciences*. McGraw-Hill Inc., second edition, 1992.

Publications and presentations

Publications

- T. Becker, K. Nelissen, B. Cleuren, B. Partoens, C. Van den Broeck. Diffusion of Interacting Particles in Discrete Geometries. *Phys. Rev. Lett.*, 111:110601, 2013
- T. Becker, K. Nelissen, B. Cleuren, B. Partoens, C. Van den Broeck. Diffusion of interacting particles in discrete geometries: Equilibrium and dynamical properties. *Phys. Rev. E*, 90:052139, 2014
- T. Becker, K. Nelissen, B. Cleuren, B. Partoens, C. Van den Broeck. Adsorption and desorption in confined geometries: A discrete hopping model. *Eur. Phys. J. Special Topics*, 223:3243, 2014
- T. Becker, T. Willaert, B. Cleuren, C. Van den Broeck. Echo states for detailed fluctuation theorems. *Phys. Rev. E*, 91:012101, 2015
- T. Becker, K. Nelissen, B. Cleuren, B. Partoens, C. Van den Broeck. Comment on "Generalized exclusion processes: Transport coefficients." *arXiv:1412.6324*, 2015
- T. Becker, K. Nelissen, B. Cleuren. Current fluctuations in boundary driven diffusive systems in different dimensions: a numerical study. *arXiv:1502.07559*, 2015

Poster presentations

- *Diffusion of interacting particles in discrete geometries*, Summer school on Fundamental Problems in Statistical Physics XIII, Leuven, 16-29 June 2013
- *Diffusion of interacting particles in discrete geometries*, Summer School on Statistical Physics of Complex and Small Systems III, Palma de Mallorca, 2-13 September 2013
- *Diffusion of interacting particles in discrete geometries*, International Workshop on Brownian Motion in Confined Geometries, Dresden, 17-21 March 2014

Talks

– *Diffusion of interacting particles*, General Scientific Meeting of the Belgian Physical Society, Leuven, 28 May 2014

Dankwoord

Eerst en vooral wil ik mijn promotor Bart bedanken. Hij maakte altijd tijd voor mijn vele vragen, die met veel geduld werden besproken. Het is dankzij zijn continue inzet dat deze thesis geworden is tot wat hij is. Christian wil ik vooral bedanken voor de belangrijke rol die hij heeft gespeeld bij de publicatie van onze eerste paper. Dankzij zijn ervaring en wetenschappelijke drive is de impact van de paper sterk verhoogd. De samenwerking met Kwinten en Bart Partoens was wetenschappelijk zeer vruchtbaar. Kwinten zijn wekelijkse bezoeken waren altijd aangenaam.

Ook alle andere collega's moet ik bedanken voor de aangename werksfeer: Carlo, Koen, Gert. Mieke, die mij in mijn eerste jaar heeft begeleid met computers, cake, en aangename babbels. Tim, mijn eerste kantoorgenoot en soms een echte spraakwaterval. Het constant in vraag stellen van je kennis, en de daaropvolgende discussies, zijn ook voor mij leerrijk geweest. Hans en Karel bedank ik voor de vele (al dan niet wetenschappelijke) discussies. Onze weddenschappen hebben gezorgd voor veel taart en weinig bonje. De G6 is de perfecte plaats om een middagmaal te nuttigen: Rik, Michel, Rene, Rob, Dorine, Sabine, Wim, Marcel, Ben, ...: de sfeer (en de koffie) was altijd zeer goed.

Mijn vrienden en familie bedank ik voor de vriendschap en steun. Eef, Kevin, en Bram: met jullie samenwonen was (en is) een echt plezier. Ik had me geen betere appartementsgenoten kunnen wensen. Natuurlijk een speciale vermelding voor de "inner circle", voor de vele avonden vertier. Grote dank voor de levenslange steun van mijn ouders, mijn drielingsbroertje Joris en mijn drielingszusje Marian. Het is mij veel waard dat ik zo'n goede relatie heb met jullie. Het is dan ook veelzeggend dat ik de voorbije vier jaar bijna ieder weekend naar thuis ben gegaan. Dat was dus heus niet alleen maar voor de vuile was.